Short-Range Super-Resolution Feature Extraction of Complex Edged Contours for Object Recognition by Ultra-Wideband Radar

Von der Fakultät für Ingenieurwissenschaften
Abteilung Elektrotechnik und Informationstechnik
der Universität Duisburg-Essen

zur Erlangung des akademischen Grades

Doktor der Ingenieurwissenschaften

genehmigte Dissertation

von

Rahmi Salman
aus
Lünen

1. Gutachter: Prof. Dr.-Ing. Ingolf Willms
2. Gutachter: Prof. Dr.-Ing. Thomas Kaiser

Tag der mündlichen Prüfung: 16. Juni 2014

Vorwort

Diese Dissertation basiert auf den Forschungsergebnissen, die ich während meiner Tätigkeit als wissenschaftlicher Mitarbeiter am Fachgebiet Nachrichtentechnische Systeme der Universität Duisburg-Essen erarbeitet habe.

Für meine fachliche Weiterbildung und die hervorragende wissenschaftliche Betreuung bedanke ich mich bei meinem Doktorvater Herrn Prof. Dr.-Ing. Ingolf Willms. Seine beständige wissenschaftliche Kritik führte in weiten Teilen nicht nur zu einer Einsicht, die mir ohnedies verborgen geblieben wäre, sondern trug auch nachhaltig zu meiner persönlichen Weiterentwicklung bei. Des Weiteren gilt mein Dank Herrn Prof. Dr.-Ing. Thomas Kaiser für die Übernahme des zweiten Gutachtens.

Für die gute Zusammenarbeit am Fachgebiet möchte mich bei allen ehemaligen Kolleginnen und Kollegen bedanken, mein besonderer Dank gilt Herrn M. Sc. Dilyan Damyanov, Herrn Dr.-Ing. Thorsten Schultze und Herrn M. Sc. Benedikt Friederich.

Den Herren Prof. Dr.-Ing. habil. Reiner S. Thomä, Prof. Dr.-Ing. Dr.h.c. Dr.-Ing. E.h. Werner Wiesbeck, Prof. Dr.-Ing. Thomas Zwick, Prof. Dr.-Ing. Jörn Thielecke und deren Mitarbeitern danke ich für die sehr angenehme Zusammenarbeit. Ich schätze mich sehr glücklich, dass ich die Gelegenheit hatte, mit so kompetenten Projektpartnern an einem hochinteressanten Thema geforscht zu haben.
Bei Herrn Prof. Alexander Yarovoy und Herrn Dr. Takuya Sakamoto von der TU Delft bedanke ich mich für die fabelhafte Betreuung während meines Aufenthaltes als Gastwissenschaftler in Delft.

Der größte und herzlichste Dank geht an meine Frau. Ihr Verständnis und ihre liebevolle Unterstützung, selbst unter widrigsten Umständen, ermöglichten mir die notwendige Hingabe für diese Arbeit.

Bu doktora tezi zor şartlar altında gerçekleştirildi. Çalışma sırasında bana manevi her türlü desteği veren aileme ve beni motive eden dostlara en içten teşekkürlerimi ve şükranlarımı sunarım.

Rahmi Salman

"A scientist in his laboratory is not a mere technician: he is also a child confronting natural phenomena that impress him as though they were fairy tales."

Marie Curie, 1867-1934.

Kurzfassung

Diese Dissertation leistet einen Beitrag auf dem Gebiet der ultrabreitbandigen Radartechnologie. Insbesondere handelt es sich hierbei um die Entwicklung eines Systems zur Objekterkennung anhand eines bi-statischen Breitbandradars von teilweise polygonen Objekten, welche im Abstand von 1 m umrundet und vermessen werden. Geometrische, texturbasierte und momentenbasierte Merkmale werden aus den Radardaten extrahiert, die anschließend als Metrik für die Klassifizierung der Objekterkennung dienen. Der genaue zeitliche Verlauf eines UWB Radarsignals, der aufgrund der gebotenen zeitlichen Auflösung zur Verfügung steht, wird massiv von Interferenzen und transienten Effekten der Apparatur verzerrt.

Daher wurden Algorithmen entwickelt, die eine zeitlich-örtliche Präzision des Radars gewährleisten, welche das durch die Bandbreite bedingte Auflösungsvermögen übertreffen: (i) Ein innovativer Algorithmus zur Wellenfrontextraktion unter Einsatz von polarimetrischem Diversitätsgewinn, um auch massiv überlappte Pulse zu separieren; (ii) ein Algorithmus, der anschließend hoch aufgelöste Mikrowellenbilder erzeugt und mittels der Wellenfronten die Positionen der signifikanten Streuzentren ermittelt; (iii) ein Algorithmus zur Objekterkennung, der die Mikrowellenbilder klassifiziert und abschließend unterscheidet.

Herausragende Erkennungsraten bei voller Umrundung der Objekte wurden anhand des geringsten mittleren quadratischen Fehlers erzielt. Eine auf der Bayes Theorie basierende Klassifizierung erhöht die Zuverlässigkeit der Erkennung nochmals deutlich, was insbesondere bei Teilumrundungen zutrifft.

Als zusätzliche wissenschaftliche Errungenschaft wurde ein Algorithmus entwickelt, der stereoskopische 3D Bilder mithilfe einer räumlich verteilten synthetischen Apertur eines bi-statischen Radars ermittelt.

Um die Leistungsfähigkeit der entwickelten Algorithmen und Systeme in der Realität zu verifizieren, wurden alle in dieser Arbeit entwickelten Algorithmen experimentell validiert und insbesondere das Objekterkennungssystem im Rahmen einer umfangreichen Messkampagne untersucht.

Abstract

This thesis contributes to the field of short-range ultra-wideband (UWB) Radar. In particular, an object recognition approach performed by a bi-static UWB Radar has been investigated in this thesis. The investigated objects consist of simple canonical and some polygonal complex objects which are scanned on a circular track at about 1 m distance. Geometrical features, texture features and moment based features are extracted from the Radar data to carry out the recognition. Yet, the precise temporal evolution is subject to massive distortions, mainly caused by severe interference conditions and transient effects of the hardware.

Thus, super-resolution algorithms have been developed which go far beyond the classical bandwidth given resolution and asked for research on various fields: (i) An innovative wavefront extraction algorithm with polarimetric diversity exploitation has been developed to separate pulses which overlap almost the whole pulse duration; (ii) a highly precise feature extraction algorithm has been developed which localises significant scattering centres by processing the previously extracted wavefronts; (iii) a novel UWB object recognition algorithm has been developed to classify and discriminate the resulting microwave images.

When scanning objects from all sides, exceptional recognition of objects was achieved by a minimum mean squared error classifier. Further improvement in recognition was obtained, especially at severly restricted tracks, by the application of Bayes theory which constitutes a superior classifier to the above.

In addition to the main field of research, a novel stereoscopic 3D UWB imaging algorithm, based on a spatially spanned synthetic aperture in conjunction with ellipsoidal shaped wavefronts, has been developed.

The ultimate test of any model and system is an experimental validation. Consequently in this thesis, all developed algorithms and the object recognition as a whole system are experimentally validated within an elaborate measurement campaign.

Contents

Notation

In the following lists the main Latin and Greek symbols, abbreviations and constants are listed. All are sorted in an alphabetic order in separated lists, while Greek symbols are listed directly after the corresponding Latin symbols. Symbols with the same initial letter are ordered according to the first appearance in the text. The page number of the first appearance is provided in the last column.
Scalar quantities are written in italic letters (a, A), vector valued and matrix valued quantities are written in bold straight letters. Vectors differ from matrices by having an arrow $\vec{\mathbf{A}}$ above whilst matrices $\mathbf{A}$ do not. Time domain quantities are denoted with small letters and frequency domain quantities with capital letters.
The bibiliography is itemised in alphabetic order of the first authors name. This thesis is written in British english notation.

Symbols		Page
$\vec{\mathbf{A}}$	Amplitude vector of the electric field	17
A_x	Component of $\vec{\mathbf{A}}$ in x dimension	19
A_y	Component of $\vec{\mathbf{A}}$ in y dimension	19
$\tilde{a}$	Artefact quantity	74
a	Major axis of an ellipse	82
α_n^i	Angle between the antenna axis of the MUT and the intersection point $\vec{\mathbf{P}}_n^i$	84
α_{opt}	Optimal angle between the antenna axis and the path between the scattering centre and the Rx_{MUT}	85

Symbols		Page
$\vec{\mathbf{B}}$	Magnetic flux density	16
b	Minor axis of an ellipse	82
c_{med}	Velocity of light in a particular medium	17
$\vec{\mathbf{D}}$	Electric flux density	16
Δ_{ab}	Distortion parameter of b with regard to a	40
$\vec{\mathbf{E}}$	Electric field strength	16
$\vec{\mathbf{e}_x}$ $\vec{\mathbf{e}_y}$ $\vec{\mathbf{e}_z}$	Three dimensional Cartesian unit vectors	17
$\vec{\mathbf{E}}_{\text{i}}(f,\theta,\psi)$	Incident electric field in the frequency domain	21
$\vec{\mathbf{E}}_{\text{s}}(f,\theta,\psi)$	Scattered electric field in the frequency domain	21
$\vec{\mathbf{e}}_{\theta,\text{Tx}}$ $\vec{\mathbf{e}}_{\psi,\text{Tx}}$ $\vec{\mathbf{e}}_{r,\text{Tx}}$	Unit vectors of a local spherical coordinate system with regard to the Tx	31
$E_{\text{i}}^{\psi,\text{Tx}}(f,\theta,\psi)$	Component of $\vec{\mathbf{E}}_{\text{i}}(f,\theta,\psi)$ in ψ,Tx dimension	32
$E_{\text{i}}^{\theta,\text{Tx}}(f,\theta,\psi)$	Component of $\vec{\mathbf{E}}_{\text{i}}(f,\theta,\psi)$ in θ,Tx dimension	32
$\vec{\mathbf{e}}_{\theta,\text{Rx}}$ $\vec{\mathbf{e}}_{\psi,\text{Rx}}$ $\vec{\mathbf{e}}_{r,\text{Rx}}$	Unit vectors of a local spherical coordinate system with regard to the Rx	32
$E_{\text{s}}^{\psi,\text{Rx}}(f,\theta,\psi)$	Component of $\vec{\mathbf{E}}_{\text{s}}(f,\theta,\psi)$ in ψ,Rx dimension	32
$E_{\text{s}}^{\theta,\text{Rx}}(f,\theta,\psi)$	Component of $\vec{\mathbf{E}}_{\text{s}}(f,\theta,\psi)$ in θ,Rx dimension	32
$\vec{\mathbf{E}}_{\text{i}}(f,\theta_{\text{Tx}},\psi_{\text{Tx}},r)$	Incident electric field in the frequency domain at a certain distance r induced by the Tx	34
$\vec{\mathbf{e}}_{\text{i}}(t,\theta,\psi,r)$	Incident electric field in the time domain at a certain distance r induced by the Tx	34
$e_{\text{i}}^{\eta}(t,\theta,\psi,r)$	Component of $\vec{\mathbf{e}}_{\text{i}}(t,\theta,\psi,r)$ with η polarisation state	41

Symbols		Page
$e^{\eta}_{\mathrm{i,B}}\left(t,\theta_{\mathrm{B}},\psi_{\mathrm{B}},r\right)$	Component of $\vec{\mathbf{e}}_{\mathrm{i}}(t,\theta,\psi,r)$ with η polarisation state in boresight direction	41
$\mathcal{E}$	Ellipse of identical TOF	80
$\mathcal{E}^{i}_{n}$	i-th ellipse of identical TOF created at the n-th measurement point	82
$\bar{\mathcal{E}}$	Ellipsoid of identical TOF	96
ϵ	Permittivity	16
$\tilde{\epsilon}$	Eccentricity	111
F_{ba}	Fidelity of b with regard to a	40
$F_a(a)$	Cumulative distribution function of the random variable a	74
$\vec{\widetilde{\mathbf{F}}}_{\mathrm{MI}}$	Moment invariant feature	108
$\widetilde{F}_{\mathrm{EC}}$	Eccentricity feature	108
$\widetilde{F}_{\mathrm{FC}}$	Fitting circle feature	108
$\widetilde{F}_{\mathrm{FF}}$	Form factor feature	108
$\widetilde{F}_{\mathrm{IN}}$	Inertia feature	108
$\vec{\widetilde{\mathbf{F}}}_{\mathrm{FD}}$	Fourier descriptors feature	108
$\vec{\widetilde{\mathbf{F}}}_{\mathrm{CS}}$	Curvature scale feature	108
$f_a(a)$	Probability density function of the random variable a	128
φ_x	Constant phase term in x dimension	19
φ_y	Constant phase term in y dimension	19
φ_{xy}	Phase difference between x and y dimension	19
$g(p)$	Gaussian filter	118
η	Polarisation state	28

Symbols		Page
.....		
$\vec{\mathbf{H}}$	Magnetic field strength	16
HH	Co-polarisation channel with horizontal Tx and horizontal Rx	21
HV	Cross-polarisation channel with horizontal Tx and vertical Rx	21
$h(t)$	Impulse response	26
$h^{\eta}(t, \theta, \psi)$	Spatially dependent impulse response with η polarisation state	28
$\vec{\mathbf{H}}_{\mathrm{Tx}}(f, \theta, \psi)$	Spatially dependent transfer function of the Tx	33
$H^{\eta}_{\mathrm{Tx}}(f, \theta, \psi)$	Component of $\vec{\mathbf{H}}_{\mathrm{Tx}}(f, \theta, \psi)$ with η polarisation state	33
$\vec{\mathbf{H}}_{\mathrm{Rx}}(f, \theta, \psi)$	Spatially dependent transfer function of the Rx	33
$H^{\eta}_{\mathrm{Rx}}(f, \theta, \psi)$	Component of $\vec{\mathbf{H}}_{\mathrm{Rx}}(f, \theta, \psi)$ with η polarisation state	33
$\mathbf{H}_{\mathrm{Sc}}(f, \theta, \psi)$	Spatially dependent scattering matrix of an arbitrary scatterer in the frequency domain	33
$\vec{\mathbf{h}}_{\mathrm{Tx}}(t, \theta, \psi)$	Spatially dependent impulse response of the Tx	34
$\vec{\mathbf{h}}_{\mathrm{Rx}}(t, \theta, \psi)$	Spatially dependent impulse response of the Rx	35
$\mathbf{h}_{\mathrm{Sc}}(t, \theta, \psi)$	Spatially dependent scattering matrix of an arbitrary scatterer in the time domain	35
$\vec{\mathbf{H}}_{\mathrm{AUT}}(f, \theta, \psi)$	Spatially dependent transfer function of the AUT	35
$\vec{\mathbf{H}}_{\mathrm{REF}}(f, \theta, \psi)$	Spatially dependent transfer function of the REF	35
$H^{\eta}_{\mathrm{AUT}}(f, \theta, \psi)$	Component of $\vec{\mathbf{H}}_{\mathrm{AUT}}(f, \theta, \psi)$ with η polarisation state	37

Symbols		Page
$h^{\eta}_{\mathrm{AUT}}(t,\theta,\psi)$	Spatially dependent impulse response of the AUT with η polarisation state	37
$h^{\eta+}_{\mathrm{AUT}}(t,\theta,\psi)$	Analytic signal of $h^{\eta}_{\mathrm{AUT}}(t,\theta,\psi)$	38
h_i	i-th Hu moment	110
θ	Elevation angle	21
θ_{Tx}	Elevation angle of the Tx	31
θ_{Rx}	Elevation angle of the Rx	31
I	Moment of inertia	113
$\mathbf{J}_{\vec{\mathbf{f}}}$	Jacobian matrix of the vector $\vec{\mathbf{f}}$	97
$\vec{\mathbf{k}}$	Wave vector of the electric field	17
$\vec{\mathbf{k}}_{\mathrm{P}}(f,\theta,\psi)$	Pauli vector	24
$k_{\mathrm{P},1}(f,\theta,\psi)$	1st element of the Pauli vector which corresponds to odd numbered bounce scattering	24
$k_{\mathrm{P},2}(f,\theta,\psi)$	2nd element of the Pauli vector which corresponds to even numbered bounce scattering	24
$k_{\mathrm{P},3}(f,\theta,\psi)$	3rd element of the Pauli vector which corresponds to diffuse scattering	24
$\kappa(p)$	Curvature of a curve parameterised with the path length p	117
l_1	Travelling path from the Tx to the scattering centre	81
l_2	Travelling path from the scattering centre to the Rx	81

Symbols		Page
$l^i_{1,n}$	Distance between $\mathrm{Tx}_{\mathrm{MUT}}$ and the intersection point determined by $\mathcal{E}_{\mathrm{MUT}}$ and $\mathcal{E}^i_n$	84
$l^i_{2,n}$	Distance between $\mathrm{Rx}_{\mathrm{MUT}}$ and the intersection point determined by $\mathcal{E}_{\mathrm{MUT}}$ and $\mathcal{E}^i_n$	84
λ_{c}	Wavelength of the centre frequency	74
$m_{\mathrm{ref}}(t)$	A priori measured reference pulse	54
$m_{\mathrm{ref,shift}}(t)$	Reference pulse shifted with the peak point to the origin of the time scale	55
$m^{\mathrm{w}}_{\mathrm{ref,shift}}(t)$	windowed version of $m_{\mathrm{ref,shift}}(t)$	55
$m_{\mathrm{MUT}}(t)$	Measured pulse under test	55
$\bar{m}_{\mathrm{MUT}}(t)$	Remaining $m_{\mathrm{MUT}}(t)$ after removing an extracted wavefront	56
$m_{\mathrm{ref,syn}}(t, \tau_{\mathrm{syn}})$	Synthetic reference waveform superposed of $m^{\mathrm{w}}_{\mathrm{ref,shift}}(t)$ and a duplicate delayed by τ_{syn}	58
$m_{\mathrm{MUT,syn}}(t)$	Synthetic $m_{\mathrm{MUT}}(t)$	60
$m^{\mathrm{norm}}_{\mathrm{MUT,syn}}(t)$	Normalised $m_{\mathrm{MUT,syn}}(t)$	61
$m_n(t)$	n-th neighbouring measurement	82
m_{pq}	Regular moment of the order $p+q$	109
$\mathcal{M}$	Feature set of the MUT	120
μ	Permeability	16
μ_{pq}	Central moment of the order $p+q$	109
N_{sub}	Total number of pseudo centres of gravity plus the exact one	123
$o(x, y)$	Discretised image	91
$\hat{\mathrm{o}}^i_{\mathrm{MMSE}}$	Output of the OR algorithm evaluated by the MMSE classifier for the i-th MUT	121

Symbols		Page
$\hat{\mathrm{o}}^i_{\mathrm{Bayes}}$	Output of the OR algorithm evaluated by the Bayes classifier for the i-th MUT	129
$P^{\eta}(\theta,\psi)$	Spatially dependent peak amplitude of the envelope of a pulse with η polarisation state	38
$\vec{\mathbf{P}}^i_n$	Position vector to the intersection point between $\mathcal{E}_{\mathrm{MUT}}$ and $\mathcal{E}^i_n$	82
$\vec{\mathbf{P}}_{\mathrm{tp}}$	Position vector to the target point	87
$\vec{\mathbf{P}}^c_{\mathrm{cl}}$	Position vector to the c-th member of the cluster	112
$P(a\|b)$	Conditional probability of the random variable a given b	125
$P(a)$	Probability of the random variable a	125
q^i_n	Convergence evaluation function for $\mathcal{E}^i_n$	85
Q	Superposition of all elements of q^i_n	85
$R_{ab}(\tau)$	Normalised cross-correlation function between a and b	55
$\vec{\mathbf{Rx}}$	Position vector to the Rx	80
r_{MUT}	Distance between the target point and $\vec{\mathbf{Rx}}_{\mathrm{MUT}}$	87
$r_{\max}$	Radius of the fitting circle	112
$\mathcal{R}$	Feature set of the reference alphabet	13
$\mathbf{S}(f,\theta,\psi)$	Polarisation scattering matrix	21
$\mathbf{S}_{\mathrm{Sc}}(f,\theta,\psi)$	Sinclair scattering matrix	22
$\mathbf{S}_{\mathrm{Odd}}$	Basis matrix of the Pauli decomposed Sinclair scattering matrix which corresponds to odd numbered bounce scattering	24

Symbols		Page
$\mathbf{S}_{\text{Even}}$	Basis matrix of the Pauli decomposed Sinclair scattering matrix which corresponds to even numbered bounce scattering	24
$\mathbf{S}_{\text{Diffuse}}$	Basis matrix of the Pauli decomposed Sinclair scattering matrix which corresponds to diffuse scattering	24
S_{21}	Transmission coefficient in terms of an S-parameter	35
s	Scaling factor	55
$\boldsymbol{\sigma}(f, \theta, \psi)$	Radar cross section	22
σ_α	Standard deviation of q_n^i	85
σ_{cs}	Standard deviation of $g(p)$	118
t	Time	16
T_{w}	Width of a rectangular window	55
T_{pw}	Pulsewidth	59
$\vec{\mathbf{Tx}}$	Position vector to the Tx	80
$\mathcal{T}_{\text{true}}$	Set of true scattering centres	74
$\mathcal{T}_{\text{estimated}}$	Set of estimated scattering centres	74
$\tau^{\eta}_{\text{FWHM}}(\theta, \psi)$	Spatially dependent full width at half maximum of the pulse envelope with η polarisation state	38
$\tau^{\eta}_{\text{r},\alpha}(\theta, \psi)$	Spatially dependent ringing duration of the pulse envelope with η polarisation state until the envelope has decreased from the peak amplitude $P^{\eta}(\theta, \psi)$ below the fraction α of $P^{\eta}(\theta, \psi)$ and remains consistently below it	38

Symbols		Page
τ	Delay time	55
$U_{\mathrm{Tx}}(f)$	Tx stimulating UWB signal in the frequency domain	33
$u_{\mathrm{Tx}}(t)$	Tx stimulating UWB signal in the time domain	34
$U_{\mathrm{Rx}}(f)$	UWB signal induced in the Rx in the frequency domain	34
$u_{\mathrm{Rx}}(t)$	UWB signal induced in the Rx in the time domain	35
v_{ph}	Phase velocity	17
VV	Co-polarisation channel with vertical Tx and vertical Rx	21
VH	Cross-polarisation channel with vertical Tx and horizontal Rx	21
$w(t)$	Window function	59
$w_{\mathrm{invert}}(t)$	$1 - w(t)$	61
ω	Angular frequency	16
$\overline{x}$	x dimension of the centre of gravity	109
$\overline{y}$	y dimension of the centre of gravity	109
ψ	Azimuth angle	21
ψ_{Tx}	Azimuth angle of the Tx	31
ψ_{Rx}	Azimuth angle of the Rx	31
Z_{F}	Wave impedance	17

Symbols		Page
Z_{Tx}	Characteristic impedance of the Tx	34
Z_{Rx}	Characteristic impedance of the Rx	34
$z(p)$	A curve parameterised with the path length p	116
$Z(k)$	Fourier spectrum of $z(p)$	116

Abbreviations		Page
AUT	Antenna under test	35
B	Boresight	41
BST	Boundary Scattering Transform	7
CCF	Cross correlation function	40
DCM	Dynamic correlation method	58
EM	Electromagnetic	18
FCC	US Federal Communications Commission	1
GN	Gauss-Newton method	96
H	Horizontal polarisation state	21
IBST	Inverse Boundary Scattering Transform	7
KM	Kirchhoff migration	90
LTI	Linear time-invariant	26
MMSE	Minimum mean squared error	11
MUT	Measurement under test	13
OR	Object recognition	4
OUT	Object under test	107
PDCM	Polarimetric dynamic correlation method	66
PDF	Probability density function	126
Radar	Radio detection and ranging	1
REF	Reference antenna	35
RCS	Radar cross section	22
Rx	Receiver	21
SAR	Synthetic aperture Radar	13
S3D	Stereoscopic 3 dimensional	11
TOF	Time of flight	3
TEM	Transverse electromagnetic	17
Tx	Transmitter	21

Abbreviations		Page
UWB	Ultra-Wideband	1
V	Vertical polarisation state	21

Constants	
c_0	Velocity of light in vacuum: $2.9979 \cdot 10^8$ m/s
e	Number of Euler: 2.7182...
ϵ_0	Permittivity of the vacuum: $8.854 \cdot 10^{12}$ As/(Vm)
μ_0	Permeability of the vacuum: $4\pi \cdot 10^{-7}$ Vs/(Am)
j	$\sqrt{-1}$
π	Ludolphian number: 3.1415...
Z_0	Characteristic free-space impedance: $120\pi\,\Omega$

FIRST CHAPTER

Introduction

Inspired by Maxwell's work, Heinrich Hertz was the first radio pioneer who experimentally proved the existence of EM waves with his famous spark gap experiments in 1887. By the turn of the century, innovative research in wireless radio transmission was driven foremost by Guglielmo Marconi, Alexander Stepanovich Popov and Nikola Tesla which resulted in the first wireless transatlantic transmission in 1901. The beginning of radio detection and ranging (Radar) technology, to which this doctoral thesis shall contribute to, can be dated back to 1904 when Christian Hülsmeyer applied for a patent entitled "*Verfahren, um entfernte metallische Gegenstände mittels elektrischer Wellen einem Beobachter zu melden*". For the first time in history the reception of scattered EM waves was employed to detect a target which was a ship in this particular case.

From a signal and system theory point of view it can be summarised that the beginning of wireless propagation started with ultra-wideband (UWB) signals since all aforementioned radio pioneers used spark-gap transmitters and coherer-detectors. The generated sparks comply with very short pulses which correspond to a huge occupied frequency spectrum. Afterwards, for more than one century UWB just existed as a niche technology mainly driven by military needs and restricted to a small community of experts. With the first official regulation in 2002 for an unlicensed usage in the range of 3.1 and 10.6 GHz by the US Federal Communications Commission (FCC) a vast ongoing interest was triggered in academia as well as in the civil industry. With regard to the allocated spectrum UWB systems are designed as an overlay

system since a large number of classical radio systems are already established in the intended frequency bands. Hence, the emission of UWB systems is restricted to a power spectral density of -41.3 dBm/MHz EIRP to provide a (i) coexistence with classical narrowband systems without severe interference effects. Consequently, the restriction in terms of radiation power predestines UWB systems to short-range operations. As a matter of principle, short-range communication, sensor networks and short-range Radar systems benefit from abundant absolute bandwidths offered by UWB technology. In the field of communications (ii) higher data-rates can be obtained since the channel capacity is increasing proportionally with the bandwith. For Radar and sensor applications UWB technology provides novel and innovative potentials and has various superior advantages in contrast to classical sensing techniques. Increased bandwidth as the key feature results in (iii) higher down-range resolution (i.e. the capability of separating two point scatterers along the main lobe). This provides provides enhanced multipath immunity, precise ranging and localisation capabilities and super-resolution imaging in delay time domain (temporal dimension within one measured signal due to the huge bandwidth, also known as fast time domain). When the large range of operational frequencies are set in the lower microwave region which starts at 300 MHz (iv) super-resolution UWB Radar systems penetrate dielectric materials to perform subsurface, in- and through-wall sensing. Recently, small and cost effective devices enter the market and due to its (v) non-ionizing nature and low-power emission attributes the admission of UWB to daily life routines with commercial and consumer applications is actually being accelarated.

In summary, due to the huge bandwidth UWB Radar complements the classical Radar technology (applied for air traffic control, weather forecasting, navigation of ships, speed limit enforcement, remote sensing, military utility et cetera) in a revolutionising progression for a wider and less homogenous

audience. From now on, Radar applications not only increase the quantity of information but rather the quality of information which enables new unforeseen dimensions in the field of sensing [60] [112].

1.1 Goal of the Thesis

The extremely huge bandwidth that is provided by UWB systems require completely new approaches and methodologies and faces engineers with new challenges with respect to the system design. The classical characterisation of RF systems is based on power-related spectral quantities, e.g. gain, radiation and directivity patterns which are well adapted to narrowband systems and large transmission distances. Basically, these quantities are also relevant for UWB systems, too. However, in contrast to simple power receivers of classical narrowband Radar systems UWB sensors record the actual time evolution of the pulse and directly provide a time of flight (TOF) by evaluating a previously defined reference feature (e.g. the peak point of a pulse). Thus, the actual pulse shape and its degree of distortion has a direct influence on the possible range resolution. Because of this, power quantities as a unique feature are absolutely not sufficient any more and will consequently lead to information losses and restrict the actual potential of UWB technology.

With regard to this paradigm shift, one of the goals of this thesis is to introduce spatio-temporal performance quantities and methodologies in order to analyse the exact temporal shape and quantify the distortion of UWB pulses after linear interactions like transmission and reception by an antenna or scattering with material. Based on these theoretic considerations ensuing research has to be performed to design, evaluate and optimise the actual super-resolution algorithms.
In particular, this thesis at hand focuses on the precise extraction and efficient processing of 2D target surface information in the short-range up to a couple

of metres by means of super-resolution UWB-Radar. A subsequent classification and object recognition (OR) from a finite alphabet shall conclude the multi-variate contemplation of objects with utmost complex contour structure. The quantification of the term 'utmost complex contour structure' always has to be treated with regard to the resolution capability of the sensing system under test. Thus, the objects have a complex edged structure with variations in the range of sub-wavelengths. Consequently, this causes interference and resonance effects resulting in pulses which overlap almost over the whole pulse width. Hence, super-resolution algorithms have to be developed which separate the pulses robustly even under these circumstances and have to go far beyond the classical resolution quantity specified by the bandwidth. Once the pulses are precisely extracted they afterwards have to be processed for a representation in a suitable image or feature map. The obtained patterns have to satisfy an extraordinary accuracy and exploit object discrepancies to the highest level to enable real-time capable OR. Thus, support vector machines, neural networks and other OR algorithms with vast computational loads shall strictly be avoided.

1.2 State of the Art

On March 11, 2011 a 9.0 earthquake and subsequent tsunami hit the nuclear power plant in Fukushima (Japan) and caused the world's most fatal nuclear disaster since Chernobyl. 150.000 people had to be displaced because of radiation contamination. More than 5 weeks passed away before the first remote controlled security robot could enter the reactor building to inspect the interior! Throughout the inspections all robots were equipped with spotlights to enable optical sensors. The scope indicated by this tragic example is: There is an unsatisfied need of civil research for UWB technology in the field of emergency and security scenarios to combine super-resolution as well as medium penetrating systems. These systems overtop, or at least complement, the classical sensors like optics, infrared, ultrasound and narrowband

Radars. Moreover, upcoming strategies and solutions in the field of future UWB Radar research offer significant humanitarian and social relevance.

There is a wide variety of applications and a notable progress in manifold scenarios which are aimed at by the ongoing UWB research. Among the most popular areas are biomedical diagnostics and imaging [46] [47] [49], archeological inspections [87], non-destructive inspection of internal structures (partially full polarimetric) [62] [113] [130] [141], out-door surveillance up to 150 m [82], food quality monitoring [148], trapped people detection [94], through-wall inspections [80] [154], ranging and localisation [153] [171], ambient assisted living [50], UWB Radar equipped mobile security robots for environmental imaging [133] [143], short-range super-resolution imaging and feature extraction (partially full polarimetric and 3D) [45] [48] [117] [132] [134] [140] [141] [142] [146] [174].

Below, a general review of the state of the art shall be performed solely for the research fields which associate with the goals of this thesis. A particular review of specific methods and distinct algorithms which are improved and overtopped by this thesis are provided later in chapter 1.3 in detail.

Wavefront extraction

The fundamental question behind all super-resolution applications is the precise extraction of the TOF of UWB pulses. The easiest strategy to determine the TOF is to evaluate the measured data with respect to a predefined feature which is mostly the peak point of a pulse [70] [91] [92] [116]. An extended method considers a set of peak points and extracts the relevant ones determined by an additional threshold operator and specific evaluation functions to separate from false TOFs caused by noise, antenna ringing and multiple scattering [2] [74] [115] [118]. A more sophisticated method to extract multiple reflections especially under severe interference conditions is based on

iterative correlation approaches with an a priori taken reference pulse. The main idea of these methods can be interpreted as a successive estimation of channel parameters with a subsequent cancellation. At every iteration the method is applied again to the remaining channel until a termination condition is fulfilled. The beginning of this strategy can be dated back to the seventies when J. A. Högbom introduced his so-called CLEAN algorithm to enhance images of passive Radars in the field of radio astronomy [51]. As this design was based on passive non-coherent radiation derived from independently distributed point sources (stars) an adaption to active coherent Radar applications was introduced as Coherent-CLEAN in [165] and an extension to contiguous and non-isolated targets as Sequence-CLEAN in [17]. An extension to antenna arrays and beamforming utilisation was published in [22] and evaluated for UWB in [61]. SAGE is another representative of this strategy with an application in frequency domain [32] which was adapted to UWB conditions for the first time in [37] with experimental validations in [38] and [144]. Of particular importance with regard to the scope of the thesis at hand is the application of such methods under short-range super-resolution conditions conducted first time with an experimental validation in [41] and utilised with a genetic optimisation approach in [40].

Feature Extraction and Imaging

The reconstruction of a target shape by means of received Radar data bases on the solution of an inverse problem to gather information about the scenario under test and to perform a back projection. First imaging algorithms were performed in the field of geophysics and seismic engineering in the late sixties [103] [149] [155]. Later, ground penetrating Radar applications [58] [104] and spaceborne as well as airborne remote sensing [27] [30] [31] incorporated the technique of migration for their issues. Since more than one decade imaging has been transferred to short-range applications in combination with UWB. So far, all mentioned migration applications and scenarios have in

common that they directly operate on the whole temporal evolution of the Radar data in a summation sense to perform a focusing operation. For this purpose finite difference or boundary integral techniques based on the Helmholtz-Kirchhoff theorem are performed for every pixel with regard to relevant sensor positions of the real or synthetic apperture [90] [150]. Slight modifications were performed mostly to reduce the computational load by performing the summation in the frequency domain [162], by evaluating a cross-correlation with reference measurements from different positions to reduce ambiguities [172] or by an adaption to MIMO-Radar systems [175]. A comprehensive review and comparison about the various migration methods with regard to short-range UWB sensing is provided in [43] [44] [174]. In contrast, wavefront based imaging methods derive target surface points by relating the TOFs of resolved scatterers to the sensor position. Hence, the computational load reduces immensely which enables high-speed accurate imaging. However, these methods basically assume a smooth surface or at least just a gently curved surface because the image quality highly depends on the precise wavefront estimation of each scattering centre. The boundary scattering transform (BST) and its inverse BST (IBST) calculation was first mentioned in 1992 [36] in the field of seismic engineering but yet applied to short-range UWB sensing in 2004 by Sakamoto et al [115]. Up to now, significant research effort has been spent on IBST inspired algorithms based on the evaluation of TOF changes to conduct more robust images with less artifacts even for very complex targets including many edges [48] [73] [74] [75] [117].

Polarimetry

The spatial distribution of scattered energy depends on the target geometry, the operating frequency, the material composition and on the polarisation of the incident wave. Thus, fully polarimetric Radar systems exhibit increased information content of an EM wave. Although polarimetric techniques have proven themselves as one of the most powerful tools in the field of remote

sensing the vast majority of publications in the community of UWB Radar deals with mono-polarised systems. Therewith, the vector nature of an EM wave which can only be described as a vector summation in two orthogonal dimensions is simply ignored and performance degradations result as a consequence.

Object Recognition

The science about OR and the academic contributions in this field cover a quasi immeasurable amount of quantity over several decades. Despite of this, real OR research on short-range super-resolution UWB Radar with a set of complex edged objects cannot be found in the literature. These applications go far beyond classical detection and classification applications and exploit target discrepancies to the highest level of accuracy in the case of utmost complex objects. In the broadest sense, similar approaches can be found in the field of mine detection by ground penetrating Radar to separate mines from clutter in a sense of classification and reduced false alarm rates [77] [145]. In [76] a so-called OR for UWB is performed but actually the paper presents a classification system for planes in long-range ($\sim$ 100 km). A vague system design for an OR Radar application is introduced with a high degree of abstraction in [7] but neither with any concrete OR algorithm nor defined object shapes. The same applies to [9] [10] [108]. A promising OR method is introduced in [69] for buried objects. However, the introduced objects consist of a simple contour which provoke just single reflections and the processed Radar data is obtained by Finite-Difference-Time-Domain simulations with minor practical relevance. In [54] a recognition is performed with respect to the material composition (plastic pipe against metal pipe) which is not comparable to OR performed onto the geometry of the object contour.

1.3 Novelty of the Thesis

The results and technological advancements of this thesis contribute to improve the performance of UWB Radar systems especially in the field of super-resolution imaging, image enhancement, target detection, target clasification as well as target tracking and UWB OR. This progress is established due to the development of sophisticated algorithms and smart signal processing which are well matched to the novel conditions given by the wide occupied frequency band. It is obvious "[...] that signal processing and data mining will become a key point in future development of UWB sensing in order to be able to explore and exploit the wanted information hidden in the captured data. Data processing will gain much more importance than it has in narrowband sensing." [112]
This assumption by J. Sachs who is a senior lecturer with more than three decades experience in the field of Radar sensing technology could be fully confirmed within the research for the thesis at hand.
The synthesis of full polarimetry to the UWB system design further improves the efficiency as well as the performance immensely. Research in this field has been driven significantly by R. S. Thomä who is a distinguished german scientist with more than 3 decades experience in the field of sensing [3] [33] [88] [141] [163]. In the context of OR, the adaptation of the Pauli scattering matrix decomposition into a short-range UWB Radar system is a pioneering issue [3] [33] [134] [137] [139] [140] since up to now this method was only applied in the field of narrowband remote sensing.
Traditionally, high frequency wireless systems are considered and evaluated in the frequency domain with power related quantities. However, with respect to the huge given bandwidth transient effects of devices, components and the scattering processes are not negligible any more. There is an urgent need of so far unusual temporal quality measures and quantification methodologies instead of power related spectral quantities for the evaluation of high frequency systems. Thus, time domain considerations have to be taken into

account to quantify and evaluate UWB systems properly and enable a clearer insight into the dispersive and distortive behavior of UWB devices and systems [99].
In particular, the novelties achieved with this thesis are as follows:

- A superior wavefront extraction algorithm which is able to determine pulses under massive interference effects due to utmost complex objects is presented in **chapter 4**. The main idea of the algorithm is the design of a set of synthetic waveforms which consists of a superposition of differently delayed overlapping pulses. This set of synthetic waveforms serves as a reference pattern for a correlation based search of wavefronts. Further improvement could be achieved by applying a Pauli scattering matrix decomposition onto the Radar data to separate even from odd numbered reflections. The application of the wavefront extraction algorithm on the therewith disjoined Radar data and a subsequent fusion promises for exceptional performance. Weak diffuse scattering responses caused by edges are not masked any more by strong specular reflections from dihedral structures. Finally, a conclusive wavefront optimisation algorithm compensates remaining erroneous wavefronts by means of a signal evolution analysis to an outstanding degree.

- A feature extraction algorithm is developed which performs on an arbitrary scanning trajectory to span an embracing synthetic aperture. This is indispensable to cover the whole target surface as well as to increase the cross-range resolution. However, as soon as the target size drops below the system given resolution an adequate image is actually not possible any more. An alternative Radar system with higher resolution capability would be an option. However, even though an adequate image is not possible due to resolution deficiencies, a feature extraction is very well possible. In this context, edges and corners are defined as

features. In the literature no algorithm for short-range UWB Radar can be found for this case. In **chapter 5** the developed algorithm that satisfies this requirement to a high degree is presented wich is based on the work in [74].

- A distinguished stereoscopic 3D (S3D) imaging algorithm will be introduced in **chapter 6**. A mathematical exact S3D imaging of a bi-static UWB Radar system requires the exact intersection point of 3 arbitrarily distributed and arbitrarily oriented ellipsoids. The solution of this mathematical question is non-trivial and an active topic of research in mathematics and geodesy [53]. Since the equation of the intersection point of 3 arbitrarily distributed and arbitrarily oriented ellipsoids in particular or quadric surfaces in general is non-linear, it cannot be solved directly. An iterative solution will be presented which utilises the Gauss-Newton method to obtain a fast converging estimation with negligible error in the least-square sense. This algorithm does actually not contribute to the OR. However, it is the successor of the award-winning S3D algorithm [132] which was developed within the research for this thesis at hand. The fact that it overtops [132] in various aspects qualifies it to be presented here.

- The final OR algorithm which utilises the data of the previously mentioned algorithms is presented in **chapter 7**. The OR algorithm based on UWB Radar was developed and experimentally verified with 12 objects. They range from simple square objects to complex objects with an echelon form causing multiple interfering single and double bounce reflections. Excellent recognition rates of more than 90% for a full circular track around the object was achieved for all objects except one with a simple minimum mean squared error (MMSE) classifier. For further investigations under severe conditions the track was restricted to 270° and 180°, respectively. As expected, the recognition rate de-

creased but, partially, the decrement is plausible since several objects are similar or even equal under certain restricted viewing angles. However, a Bayesian theory based superior classifier is applied which takes the statistical distribution of the Radar signature of each object into account. Thus, the recognition rates for the evaluations with restricted trajectories could considerably be increased once more compared to the MMSE classifier.

1.4 Organisation and Framework of the Thesis

In order to achieve the stated goals the thesis is organised in 8 chapters:

In **chapter 2** the relevant theoretical foundations from a physical point of view shall be discussed as an entry. Starting the discussion with a brief review of the Maxwell theory and its relevant consequences on Radar utilisation the chapter concludes with a talk about polarisation and the theory of polarimetric scattering decompositions.

The main characteristics of wideband signals are presented in **chapter 3** as well as the consequential differences of those signals with regard to classical narrowband signals. A model of a UWB Link including a scattering at an arbitrary scatterer serves as a theoretical basis from signal and system point of view for the further developments in the course of the thesis at hand. A description of the measurement scenario and the hardware setup for the ultimate experimental validations conclude this chapter.

Based on these theoretical principles the special requirements of a superior wavefront extraction algorithm for super-resolution systems will be discussed and the weaknesses of existing algorithms will be pointed out in **chapter 4**. According to the resulting specifications a novel polarimetric wavefront extraction algorithm was developed and performance evaluations were carried

out.

Chapter 5 introduces a robust feature extraction algorithm for arbitrary trajectories. Complex shaped objects with contour variations in the sub wavelength range cause massive interference effects. These inducing scattering centres need to be detected and extracted precisely. Thus, a synthetic aperture Radar (SAR) focusing algorithm is introduced and a feature extraction algorithm was developed which serves as a basic pattern for the OR algorithm. Numerical evaluations were carried out for a proper analysis of the performance.

A novel S3D imaging algorithm for arbitrary trajectories with a mathematical precise evaluation of the scattering centres will be introduced in **chapter 6**.

In **chapter 7** the actual OR algorithm will be introduced. In this algorithm each object is measured with a circular scanning trajectory. Within the subsequent signal processing a feature tuple which consists of moment based features, geometrical features and texture features is evaluated from the Radar data. The reference alphabet is generated as a set $\mathcal{R}$ which consists of 12 feature tuples, each for one object. The objective of the OR is to evaluate a feature tuple of an arbitrary a priori unknown measurement under test (MUT) and to perform a recognition by comparing the tuple of the MUT against each tuple of $\mathcal{R}$. The recognition is carried out for full circular tracks, 270° and 180° restricted tracks with a simple MMSE classifier as well as with a superior Bayesian classifier based on statistical considerations to achieve highest possible recognition rates.

Chapter 8 concludes the thesis by summarising the obtained main results and a final discussion on the achievements.

The ultimate test of any model and system is an experimental validation. Consequently in this thesis, algorithm performances as well as the OR as a whole system are verified experimentally to prove real-world capability and authenticity under genuine conditions.

The research for the doctoral thesis at hand was part of the 'Cooperative Localisation and Object Recognition in Autonomous UWB Sensor Networks (CoLOR)' project within the nation-wide priority program SPP1202 called 'Ultra Wideband Radio Technologies for Communications, Localization and Sensor Applications (UKoLoS)'. 16 research partners, german universities on the majority, were involved in the research program for 6 years and have conducted 25 projects in this period funded by the German Research Foundation (Deutsche Forschungsgemeinschaft, DFG). The final report with the results achieved in UKoLoS is available as an open source book in [163].

Several Students of the university Duisburg-Essen have contributed in the framework of a bachelor or master thesis to the research results of this doctoral thesis at hand. Especially, D. Damjanov has provided valuable contributions [24].

SECOND CHAPTER

Theoretical Background

In this chapter the basic theoretical knowledge shall be discussed to equip the reader with the necessary fundamental insight as a preparation for the forthcoming chapters. The discussion shall start with a brief physical review based on the Maxwell theory with the derivation of solely the relevant quantities for the sequel of the thesis. Based on the section about polarisation the theory of polarimetric scattering decompositions shall conclude this chapter.

2.1 Fundamentals from a Physical Point of View

UWB systems exploit EM wave propagation to conduct information about manifold possible processes, i.e. in the scope of this thesis the outer contour and geometry, respectively, of an object. Hence, EM waves are the carrier of the Radarinformation which finally shall be extracted by the system. The chain of sensing essentially consists of (i) radiation of EM waves by appropriate antennas, (ii) interaction with the object in the propagation path and subsequent scattering or reflection at the boundary and possibly interior parts in case of non-metallic materials and (iii) a concluding receiving by the antennas of the system. The interaction of the wave within the whole chain can be described mathematically with the Maxwell equations and the corresponding boundary conditions. A very wide variety of literature is available for this field of expertise which is investigated since several decades. Because of this and in order to focus on the scope of this thesis a brief review shall be provided in the following solely for the content which is thematically relevant. Under the assumption of a homogeneous, isotropic, linear propagation medium

free of sources (charges and currents) the Maxwell equations for free space satisfy the following conditions [5]:

$$\nabla \times \vec{\mathbf{E}} = -\frac{\partial \vec{\mathbf{B}}}{\partial t} = -\mu \frac{\partial \vec{\mathbf{H}}}{\partial t} \tag{2.1}$$

$$\nabla \times \vec{\mathbf{H}} = \frac{\partial \vec{\mathbf{D}}}{\partial t} = \epsilon \frac{\partial \vec{\mathbf{E}}}{\partial t} \tag{2.2}$$

$$\nabla \cdot \vec{\mathbf{D}} = \nabla \cdot (\epsilon \vec{\mathbf{E}}) = 0 \tag{2.3}$$

$$\nabla \cdot \vec{\mathbf{B}} = \nabla \cdot (\mu \vec{\mathbf{H}}) = 0 \tag{2.4}$$

With parameter definitions as follows

- $\vec{\mathbf{E}}$:= Electric field strength
- $\vec{\mathbf{H}}$:= Magnetic field strength
- $\vec{\mathbf{B}}$:= Magnetic flux density
- $\vec{\mathbf{D}}$:= Electric flux density
- ϵ := Permittivity
- μ := Permeability
- t := Time

and applying the rotator operator on both sides of (2.1) it yields

$$\nabla \times (\nabla \times \vec{\mathbf{E}}) = -\mu \frac{\partial}{\partial t} (\nabla \times \vec{\mathbf{H}}). \tag{2.5}$$

With the vector calculus identity $\nabla \times (\nabla \times \vec{\mathbf{V}}) = \nabla(\nabla \cdot \vec{\mathbf{V}}) - \nabla^2 \vec{\mathbf{V}}$ which works for any vector $\vec{\mathbf{V}}$ together with (2.2) and under the assumption of charge and current free medium (see (2.3)) the equation (2.5) can be simplified to

$$-\nabla^2 \vec{\mathbf{E}} = -\mu\epsilon \frac{\partial^2 \vec{\mathbf{E}}}{\partial t^2}. \tag{2.6}$$

According to the Fourier theorem (2.6) can be expressed with the angular frequency ω as

$$\nabla^2 \vec{\mathbf{E}} + \omega^2 \mu\epsilon \vec{\mathbf{E}} = 0 \tag{2.7}$$

which is known as the Helmholtz wave equation [98]. Among the infinite number of solutions to the Helmholtz equation (2.7) the most trivial solution

is the one of a constant amplitude monochromatic plane wave which can be described for an arbitrary direction $\vec{\mathbf{r}}$ as

$$\vec{\mathbf{E}}(\vec{r}, t, \omega) = \vec{\mathbf{A}} \cdot \exp\left(\mathrm{j}(\omega t - \vec{\mathbf{k}} \cdot \vec{\mathbf{r}})\right), \tag{2.8}$$

where $\vec{\mathbf{A}}$ is the complex vector of the amplitude and $\vec{\mathbf{k}}$ is the wave vector, both defined in a global Cartesian coordinate system with $\vec{\mathbf{e}_x}$, $\vec{\mathbf{e}_y}$ and $\vec{\mathbf{e}_z}$ as basis unit vectors. Consequently, a unique point in space can be defined with $\vec{\mathbf{r}} = [x \;\; y \;\; z]$ as the position vector. The natural exponential operator is expressed as $\exp(\cdot)$ and j as the imaginary number, respectively. In an isotropic medium the direction of the wave vector equals the propagation direction and it holds $\vec{\mathbf{E}} \cdot \vec{\mathbf{k}} = 0$, i.e. the electric field has just components which are orthogonal to the propagation direction. Without any loss of generality, the propagation direction can be set as the positive z-direction. In that case equation (2.8) can be expressed as

$$\vec{\mathbf{E}}(z, t, \omega) = \vec{\mathbf{A}} \cdot \exp\left(\mathrm{j}(\omega t - kz)\right), \tag{2.9}$$

with the wavenumber $k = 2\pi/\lambda$ and the wavelength λ of the corresponding angular frequency ω. Since the electric field $\vec{\mathbf{E}}$ and the magnetic field $\vec{\mathbf{H}}$ are always related to each other by the Maxwell equations, an analytical expression for the magnetic field yields

$$\vec{\mathbf{H}} = \frac{\vec{\mathbf{k}} \times \vec{\mathbf{E}}}{k Z_{\mathrm{F}}} \tag{2.10}$$

with the wave impedance $Z_{\mathrm{F}} = |\vec{\mathbf{E}}|/|\vec{\mathbf{H}}|$ [89]. In summary, from equation (2.10) it follows that $\vec{\mathbf{H}}$ and $\vec{\mathbf{E}}$ are orthogonal to each other and therewith both field vectors are orthogonal to the propagation direction which is the definition of a transverse electromagnetic (TEM) mode. The phase velocity v_{ph} of the plane wave can be calculated from the argument of equation (2.9) under the assumption of a constant phase front, i.e. $\omega \cdot t - k \cdot z = \text{const}$. Hence, the phase velocity is $v_{\mathrm{ph}} = \mathrm{d}z/\mathrm{d}t = \omega/k = 1/\sqrt{\epsilon\mu} = c_{\mathrm{med}}$ which equals

the velocity of light in a particular medium with the particular material parameters ϵ and μ. The expression $\sqrt{\epsilon\mu}$ simplifies to the physical constants of vacuum $\sqrt{\epsilon_0\mu_0}$ in case of free space which resembles pretty well to the conditions of air under daily routine. In case of a propagation medium which is free of dispersion the phase velocity equals the group velocity or the velocity of the signal, respectively. Thus, it can be concluded that a wave propagates through air with the velocity of light

$$c_0 = \frac{1}{\sqrt{\epsilon_0\mu_0}} = 2.997925 \cdot 10^8 \text{ m/s}. \tag{2.11}$$

So far, the main consequences which are relevant to the scope of this thesis shall be briefly summed up in the following. An EM wave always consists of an electric and magnetic field. In the particular case of a TEM wave, both fields are perpendicular to each other and, due to the transversality, both are perpendicular to the direction of propagation. The propagation takes place as an oscillation both in time and space. The propagation speed is finite which equals c_0 in free space.

2.2 Polarisation

The vector nature of an EM wave is clearly pointed out in (2.9) and (2.10). Thus, both fields are directional quantities with a particular alignment which can be precisely defined. Usually, the issue of polarisation is covered in the literature by means of solely the electric field. This is feasible, because the magnetic field is both perpendicular and proportional to the electric field. Polarisation is a property of an electromagnetic (EM) wave which is defined by the orientation of the electric field. As in the previous section mentioned, a TEM wave which propagates in z-direction just has electric field components in the xy-plane. The trajectory of the tip of the electric field in the xy-plane over one period of oscillation precisely specifies the polarisation of the wave in the context of Radar investigations [34].

A mathematical description in the following will rather enhance the com-

prehensibility: The plane wave solution (2.8) of the the Helmholtz equation (2.7) is complex. By taking the real part of the solution the real valued wave components in dependence of time and space can be calculated as

$$\mathrm{Re}(E_x(z,t)) = A_x \cdot \cos(\omega t - kz + \varphi_x), \tag{2.12}$$

$$\mathrm{Re}(E_y(z,t)) = A_y \cdot \cos(\omega t - kz + \varphi_y), \tag{2.13}$$

$$\mathrm{Re}(E_z(z,t)) = 0 \tag{2.14}$$

where A_x, A_y are arbitrary amplitudes and φ_x, φ_y are arbitrary phase shifts. Without loss of generality, solely the temporal oscillation shall be considered further by assuming $z = 0$. Hence, both equations (2.12) and (2.13) determine a parametric description of an ellipse on the xy-plane which is determined by the phase difference

$$\varphi_{xy} = \varphi_y - \varphi_x. \tag{2.15}$$

Hence, the decomposition of the electric field into 2 orthogonal sinusoidal waves defines a polarisation state in dependence of their amplitudes and the relative phase difference. 3 different states of polarisation are possible, which are defined as follows [166]:

linear polarisation, $\boldsymbol{\varphi_{xy} = 0}$ If both orthogonal components are in phase the vector sum is constant and the tip of the vector traces out a line in the xy-plane. An illustration is shown on the left side of Figure 2.1.

circular polarisation, $\boldsymbol{A_x = A_y \wedge \varphi_{xy} = \frac{\pi}{2} + k\pi}$ with $\boldsymbol{k \in \mathbf{N}}$ If both orthogonal components have exactly the same amplitude and are exactly ninety degrees modulo π out of phase the vector sum traces out a circle in the xy-plane. An illustration is shown on the right side of Figure 2.1.

elliptic polarisation, otherwise In every other case the tip of the vector traces out a helical trajectory in the xy-plane. An illustration is shown in the middle of Figure 2.1.

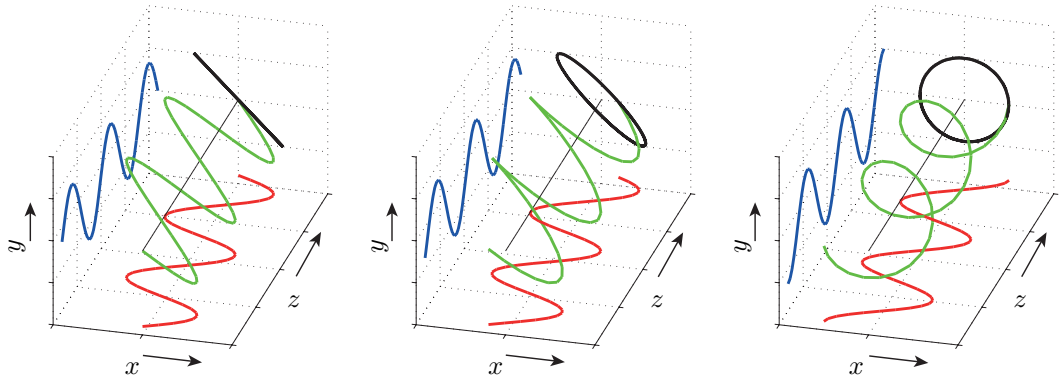

Figure 2.1: Spatial evolution of a linear (left), elliptic (middle) and circular (right) polarised TEM wave illustrated in green. The projection of both decomposed orthogonal components are plotted in blue and red, respectively. The trajectory of the temporal oscillation is plotted at the end of each abscissa z in black.

Commonly, in the field of Radar technology the polarisation state is elliptic which can degenerate to a circular or a linear state, respectively. Because of their simplicity, plane waves are frequently used to describe wave considerations although they are physically not feasible in a strong sense. However, in practice any wave can be considered, at least locally restricted, as a plane wave with negligible errors if it is regarded over a sufficiently large distance from the source which is well known as the far field condition.

To conclude the recapitulation at the end of the last section, a TEM wave can be decomposed into 2 orthogonal components. The linear algebraic relation between both components determines the polarisation of the wave. Thus, an EM wave is not a scalar field which is a negligent assumption of monopolarised Radar systems. Rather, an EM wave is a vector field where both the direction of propagation and the direction of the field forces have to be captured by a full polarimetric Radar system. Thereby, the entire potential

of EM radiation as a carrier of the Radarinformation is fully tapped because the spatial distribution of scattered EM energy depends on:

- Target geometry
- Material composition
- Operating frequency
- Polarisation of the incident wave

In classical Radar technology and particularly in the field of remote sensing the terminology refers to the geological horizon. Horizontal polarisation (H) is obtained when the electric field vector is aligned parallel to the geological horizon and consequently the vertical polarisation (V) is perpendicular to it. In this thesis the terminology is adopted if it is not explicitly mentioned otherwise. To cover the full polarimetric Radar signature of a target 4 channels have to be processed by the Radar device, i.e. HH, VV which are denoted as co-polarisation and HV, VH denoted as cross-polarisation. In this notation the first index refers to the transmitter (Tx) and the second index to the receiver (Rx).

Let $\vec{\mathbf{E}}_{\mathrm{i}}(f,\theta,\psi)$ be the incident electric field with elevation angle θ and azimuth angle ψ on a target and $\vec{\mathbf{E}}_{\mathrm{s}}(f,\theta,\psi)$ the scattered field from the target captured at a distance r from the target. A polarization scattering matrix $\mathbf{S}(f,\theta,\psi)$ can be defined [34] which describes the full polarimetric transformation of the incident field to the scattered field as

$$\vec{\mathbf{E}}_{\mathrm{s}}(f,\theta,\psi) = \mathbf{S}(f,\theta,\psi)\vec{\mathbf{E}}_{\mathrm{i}}(f,\theta,\psi). \tag{2.16}$$

By normalising the scattering matrix with the distance r a more object oriented approach was introduced by G.W. Sinclair in the late 1940's as

$$\vec{\mathbf{E}}_{\mathrm{s}}(f,\theta,\psi) = \frac{1}{\sqrt{4\pi}r}\mathbf{S}_{\mathrm{Sc}}(f,\theta,\psi)\vec{\mathbf{E}}_{\mathrm{i}}(f,\theta,\psi)$$

$$\begin{bmatrix} E_{\mathrm{s}}(f,\theta,\psi)^{\mathrm{H}} \\ E_{\mathrm{s}}(f,\theta,\psi)^{\mathrm{V}} \end{bmatrix} = \frac{1}{\sqrt{4\pi}r} \begin{bmatrix} S_{\mathrm{Sc}}(f,\theta,\psi)^{\mathrm{HH}} & S_{\mathrm{Sc}}(f,\theta,\psi)^{\mathrm{HV}} \\ S_{\mathrm{Sc}}(f,\theta,\psi)^{\mathrm{VH}} & S_{\mathrm{Sc}}(f,\theta,\psi)^{\mathrm{VV}} \end{bmatrix} \begin{bmatrix} E_{\mathrm{i}}(f,\theta,\psi)^{\mathrm{H}} \\ E_{\mathrm{i}}(f,\theta,\psi)^{\mathrm{V}} \end{bmatrix}. \tag{2.17}$$

The expression (2.17) fully covers the polarimetric scattering behaviour of a target. A power related expression which can be derived from the Sinclair scattering matrix $\mathbf{S}_{\mathrm{Sc}}(f)$ is the Radar cross section [111] (RCS)

$$\begin{aligned} \boldsymbol{\sigma}(f,\theta,\psi) &= \begin{bmatrix} \sigma^{\mathrm{HH}}(f,\theta,\psi) & \sigma^{\mathrm{HV}}(f,\theta,\psi) \\ \sigma^{\mathrm{VH}}(f,\theta,\psi) & \sigma^{\mathrm{VV}}(f,\theta,\psi) \end{bmatrix} = 4\pi \left|\mathbf{S}_{\mathrm{Sc}}(f,\theta,\psi)\right|^2 \\ &= 4\pi \begin{bmatrix} \left|S_{\mathrm{Sc}}^{\mathrm{HH}}(f,\theta,\psi)\right|^2 & \left|S_{\mathrm{Sc}}^{\mathrm{HV}}(f,\theta,\psi)\right|^2 \\ \left|S_{\mathrm{Sc}}^{\mathrm{VH}}(f,\theta,\psi)\right|^2 & \left|S_{\mathrm{Sc}}^{\mathrm{VV}}(f,\theta,\psi)\right|^2 \end{bmatrix} \end{aligned} \tag{2.18}$$

which is widely used in the classical Radar technology to quantify the echo characteristic of targets. As the components of the Sinclair scattering matrix $\mathbf{S}_{\mathrm{Sc}}(f,\theta,\psi)$ are in accordance with the spatially dependent frequency domain transfer function $H(f,\theta,\psi)$ of the classical signal and system theory [99], the RCS $\boldsymbol{\sigma}(f,\theta,\psi)$ is proportional to the power distribution of a Radar link in the frequency domain.

2.3 Pauli Scattering Matrix Decomposition

The theory of Radar polarimetry started its evolution in the late 1940's when G.W. Sinclair proved that the polarisation state of a scattered wave can be altered in reference to the polarisation state of the incident wave [156]. The 2x2 Sinclair matrix $\mathbf{S}_{\mathrm{Sc}}(f,\theta,\psi)$ describes the transformation from the incident wave vector to the scattered wave vector and gathers entire information about the scattering process as well as the scatterer itself. Immense

research effort was spent on Radar polarimetry in the following decades in which the fundamental basics were investigated [21] [26] [67] [68]. In 1970 J.R. Huynen published his groundbreaking doctoral thesis [59] in which he utilises Kennaugh's optimal polarisation concept [68] and conducts nine physical parameters extracted from the Kennaugh matrix. Thereby, the relation between Radar applications and physical parameters of the backsscattering of targets was established and can be regarded as the beginning of scattering matrix decomposition theorems in the Radar community. In recent decades and until now the major contributions are those of W.M. Boerner who initiated a critical analysis of Kennaugh's and Huynen's work and extended Kennaugh's optimal polarisation theory [12]. His studies on Radar polarimetry have an essential and irreplaceable role in the remote sensing community [13] [14] [15] [16]. Ordinarily, decomposition theorems can be categorised into two major groups [20] [81]:

Coherent Decomposition Models This group consists of decompositions performed directly on the Sinclair scattering matrix $\mathbf{S}_{\mathrm{Sc}}(f, \theta, \psi)$. The full polarimetric raw Radar data is decomposed into a superposition of even, odd and diffuse scattering contributions. These decomposed signatures can be associated with particular geometries in the surveyed scenario, e.g. buildings with double bounce scattering, sea surface and flat landscapes with single bounce scattering and vegetation canopies with diffuse scattering. The most popular example is the Pauli scattering matrix decomposition.

Non-Coherent Decomposition Models This group of decompositions are based on the decomposition of second order scattering matrices, e.g. coherency or covariance matrices. They are well suited for the use with conventional statistical concepts and were developed for the surveillance of heterogeneous landscapes where e.g. diffuse scattering vegetation is spread close to specular scattering of man-made buildings. In

this case a soft decision in terms of statistical distributions on the scattering properties is rather appropriate than hard decisions on types of scattering contributions in a particular resolution cell.

For the objective of short-range super-resolution OR the Pauli scattering matrix decomposition was adapted in this thesis to Radar systems which offer a huge spectral band occupation with the consequence of a fine temporal resolution. According to the Pauli theorem the Sinclair scattering matrix can be represented as the following linear combination [81]:

$$\begin{aligned}\mathbf{S}_{\mathrm{Sc}}(f,\theta,\psi) &= k_{\mathrm{P},1}(f,\theta,\psi)\mathbf{S}_{\mathrm{Odd}} + k_{\mathrm{P},2}(f,\theta,\psi)\mathbf{S}_{\mathrm{Even}} + k_{\mathrm{P},3}(f,\theta,\psi)\mathbf{S}_{\mathrm{Diffuse}} \\ &= k_{\mathrm{P},1}(f,\theta,\psi)\begin{bmatrix}1 & 0\\ 0 & 1\end{bmatrix} + k_{\mathrm{P},2}(f,\theta,\psi)\begin{bmatrix}1 & 0\\ 0 & -1\end{bmatrix} + k_{\mathrm{P},3}(f,\theta,\psi)\begin{bmatrix}0 & 1\\ 1 & 0\end{bmatrix}\end{aligned} \tag{2.19}$$

with $k_{\mathrm{P},1}(f,\theta,\psi)$, $k_{\mathrm{P},2}(f,\theta,\psi)$ and $k_{\mathrm{P},3}(f,\theta,\psi)$ as the weighting factors for single bounce (odd), double bounce (even) and diffuse scattering contributions, respectively, with their corresponding basis matrices $\mathbf{S}_{\mathrm{Odd}}$, $\mathbf{S}_{\mathrm{Even}}$ and $\mathbf{S}_{\mathrm{Diffuse}}$, respectively. Hence, the Pauli vector can be defined as [81]

$$\vec{\mathbf{k}}_{\mathrm{P}}(f,\theta,\psi) = \frac{1}{\sqrt{2}}\begin{bmatrix}k_{\mathrm{P},1}(f,\theta,\psi)\\ k_{\mathrm{P},2}(f,\theta,\psi)\\ k_{\mathrm{P},3}(f,\theta,\psi)\end{bmatrix} = \frac{1}{\sqrt{2}}\begin{bmatrix}S_{\mathrm{Sc}}(f,\theta,\psi)^{\mathrm{HH}} + S_{\mathrm{Sc}}(f,\theta,\psi)^{\mathrm{VV}}\\ S_{\mathrm{Sc}}(f,\theta,\psi)^{\mathrm{HH}} - S_{\mathrm{Sc}}(f,\theta,\psi)^{\mathrm{VV}}\\ S_{\mathrm{Sc}}(f,\theta,\psi)^{\mathrm{HV}} + S_{\mathrm{Sc}}(f,\theta,\psi)^{\mathrm{VH}}\end{bmatrix}. \tag{2.20}$$

The exploitation of full polarimetric systems in the field of short-range sensing ensures a diversity gain. W. Wiesbeck, a distinguished german researcher with more than four decades of experience in Radar technology had already remarked in 1989 that "The best information source for fixed target aspect angles is the wide-band polarimetric behavior of the RCS." [111]
For example, a horizontally oriented wire concealed under clothes and not visible by optics just induces HH returns. The same applies for vertically oriented wires for VV polarisation state. A tilt of the wire will induce stronger

echoes in both cross polarised states. Hence, significant features of a target may be invisible for mono polarised systems in worst case. The integration of decomposition techniques into UWB systems enhance the superior potentials of wideband Radar further more. Actually, the particular preferences are twofold:
Firstly, polarimetric techniques can be performed in delay time domain. UWB systems can resolve multiple scattering centres within one measurement and evaluate each centre with regard to their polarimetric signature, whereas narrowband systems classify one measurement as a whole due to the lack of resolution.
Secondly, by decomposing the Radar data into odd bounce reflections and even bounce reflections super-resolution wavefront extraction algorithms could be immensely improved. In mono polarised systems specular as well as diffuse scattering contributions superimpose in interfering scenarios. The extraction of weak diffuse odd scattering centres (e.g. edges) which are masked by strong specular reflections from dihedral structures is a tremendous challenge.

Within the framework of the research for the thesis at hand comprehensive investigations were performed [133] [137] [139] [140] [141] [142] including experimental validations. These validations were performed for the first time in the field of wideband sensing and shall be discussed later in the chapter 4.

THIRD CHAPTER

Ultra-Wideband Precautionary Measures

In this chapter the particularity of an impulse-based wide occupation of bandwidth and the resulting consequences shall be discussed. The crucial differences between narrowband and wideband systems will be pointed out and the consequential paradigm shift with regard to the description and evaluation of wideband systems will be highlighted. Indispensable time domain quality measures and quantification methodologies, respectively, shall be derived from a full polarimetric spatio-temporal bi-static model of a UWB Radar Link. This model serves as a theoretical basis from a signal and system point of view for the further developments in the course of the thesis at hand. A description of the measurement scenario and the hardware setup for the ultimate experimental validations conclude this chapter.

3.1 The Paradigm Shift of Impulse based UWB Systems

In the field of classical signal and system theory the actual scientific practice is more or less 'narrowband'. The majority of publications and educational books in this field deals with sinusoidal signals and waves. The basic reasoning is straightforward; in the linear time-invariant (LTI) theory any system that exhibits the properties of linearity and time invariance can be described entirely by the system's impulse response $h(t)$. The output of an LTI system can be calculated via the convolutional operator applied onto any type of

time domain input signal and $h(t)$. Any LTI system exhibits eigenfunctions or basis functions, respectively, that equal complex exponentials [102]. Thus, if the input is a complex exponential then the output preserves the input's shape as well as the frequency. Only the amplitude and a time delay which is mostly expressed in terms of a phase shift may change. Ab initio, the academic research on civil radio propagation analysed almost all narrowband systems with sinusoidals at the carrier frequency of the system. This is feasible, since the occupied bandwidth is commonly just a few percentages of the carrier frequency (e.g. 20 MHz @ 5.5 GHz, IEEE 802.11a; 20 MHz @ 2.45 GHz, IEEE 802.11b, g; 1 MHz @ 2.4 GHz, IEEE 802.15.1; 300 MHz @ 9.65 GHz, TerraSAR-X). System design, hardware architecture, implementation as well as algorithms were entirely matched to the carrier frequency. In the early days of radio development this strategy was efficient, e.g. with regard to feasible interference mitigation, modulation- and access schemes.
In the field of narrowband Radar systems it is not only the antennas which exhibit a nearly negligible transient influence. Also the fact that in most cases the dimensions of the surveyed objects are smaller than the envelope of the sounding signal prevents a significant distortion and shape variation [112]. Considering the discussed signal shape preservation capabilities of narrowband systems, it is feasible to quantify the transmission specifications in the frequency domain [158]. This is a very well established 'narrowband' strategy; significant transmission properties are characterised by power related spectral quantities, e.g. antenna gain, radiation pattern, efficiency, effective area, RCS etc.

For wider bandwidths, the frequency dependent propagation characteristics are not negligible any more and the straightforward evaluation of wider bandwidths with narrowband methods is not sufficient since transient effects are not taken into account [66] [161]. For UWB super-resolution applications the above discussed paradigms and convenient properties which are well matched

to narrowband conditions drastically change or, at least, exhibit a large error potential. The pulse width in pulsed systems or the coherence length in M-sequence devices, respectively, may usually be in the sub nanosecond range which is finally determined by the operating bandwidth. Meanwhile, low cost (in comparison with a vector network analyser) devices occupy the spectrum from 1 GHz up to 15 GHz [55] which equals a theoretical pulse width of slightly more than 2 cm in free space. Consequently, common target dimensions are approximately in the same size as the coherence length of the sounding signal or even larger. "Since the geometric structure of a body strongly influences the electromagnetic fields, every action - transmission/scattering/reception - leads to signal deformation [...]." [112]
Additionally, with the provided temporal resolution also the antenna behaviour has to be considered from a different point of view than in classical narrowband systems [6] [168] [169]:

- In contrast to the narrowband case where the transient influence of the antenna is nearly negligible, in UWB systems the temporal evolution of sub nanosecond pulses are very well distorted by the antenna's transient response. For robust super-resolution applications these distortions have to be quantified to enable efficient compensation algorithms.

- The term 'distance' has to be adapted qualitatively for UWB systems. Mathematically, an unambiguous distance can be measured between two points. With the side condition of 'shortest distance' it is also possible to determine the distance unambiguously between a point and a curve or a flat plane.

As a consequence of both aspects, UWB systems unquestionably require a consideration of the transient behaviour, which can be satisfied with the spatio-temporal polarimetric impulse response $h^{\eta}(t, \theta, \psi)$ where the polarisation state is indicated with η and the angular behaviour with both the elevation angle θ and the azimuth angle ψ. Therewith, a time domain anal-

ysis of the Radar link can be obtained which is more appropriate to cover the pulse distortion than merely with power related spectral quantities. This aspect is also officially emphasized in the 'IEEE Standard for Ultrawideband Radar Definitions Std 1672-2006' [1] where it says:

> "**3.16 time-domain radar:** An early term for UWB radar. It was so named because the analysis required a time-domain approach to account for transient effects, as opposed to the frequency-domain analysis assuming constant steady-state sinusoidal signal. Had a brief period of use in the 1980s before the term ultrawideband came into common use."

Moreover, a reference (peak point or centre of gravity) for precise TOF measurements can be recovered directly from $h^{\eta}(t, \theta, \psi)$. This provides resolution capabilities with antennas of finite dimension and significantly larger than the range resolution.

Unsurprisingly, the conventional way to analyse and operate narrowband Radar systems is based on power related quantities. "Although technology has been significantly improved, state of the art Radars for most applications are mostly still what they have always been in terms of their RF system design since the past 30 to 50 years." [167]
Actually, classical Radar receivers still consist more or less of simple power receivers which are basically made of low noise amplifiers, down converters, filters and analogue digital converters with a subsequent digital processing unit. Hence, the received radiation energy is successively recorded and evaluated depending on a power related threshold. The main objective is to decide whether there is an echo or not. For this purpose, it is even a common procedure in narrowband Radar systems to consciously violate the Nyquist theorem to reduce cost and complexity [86]. A lower sampling frequency will foremost distort the shape of the signal which is irrelevant for narrowband cases.

The absolute opposite applies for UWB Radar receivers. Here, the exact temporal shape of the cumulated waves has to be captured and rendered with a subsequent classification which is carried out in the time domain and goes far beyond formerly detection operations.

The initially mentioned paradigm shift does not mean that classical power related quantities are unnecessary in the field of UWB systems, but rather it indicates that time domain transient behaviour quantities definitely have to be considered as an urgent supplement. As T. Zwick stated in the foreword of [99] "[...] that for such extremely wideband systems a frequency domain analysis is absolutely insufficient."

3.2 The Bi-Static Ultra-Wideband Radar Link

As in the previous section mentioned, a time domain evaluation is indispensable for UWB systems to treat physical processes as transient excitations of finite duration. A full polarimetric spatio-temporal analytic description of a UWB-Radar link shall be derived in this section from a signal and system theory point of view. It should be noted that it is essential to consider the spatial behaviour of the description since (i) full polarimetry shall be coped with, (ii) the spatial filtering characteristic of the antennas shall be taken into account and (iii) a close practical relevance shall be provided since in practical scenarios an ideal mutual alignment between the target and the antenna main beam cannot be guaranteed in any case. Especially the spatial filtering characterisic induces that a signal is weighted with the antenna's stereoscopic pattern and is radiated in different directions with a different temporal evolution.

Assume a bi-static configuration of directive antennas which is illustrated in Figure 3.1. The polarised incident electric field $\vec{\mathbf{E}}_{\mathrm{i}}(f, \theta, \psi)$ is radiated from the Tx towards an arbitrary scatterer which reradiates the wave, due to its composition and geometry, isotropically. The fraction of the scattered field

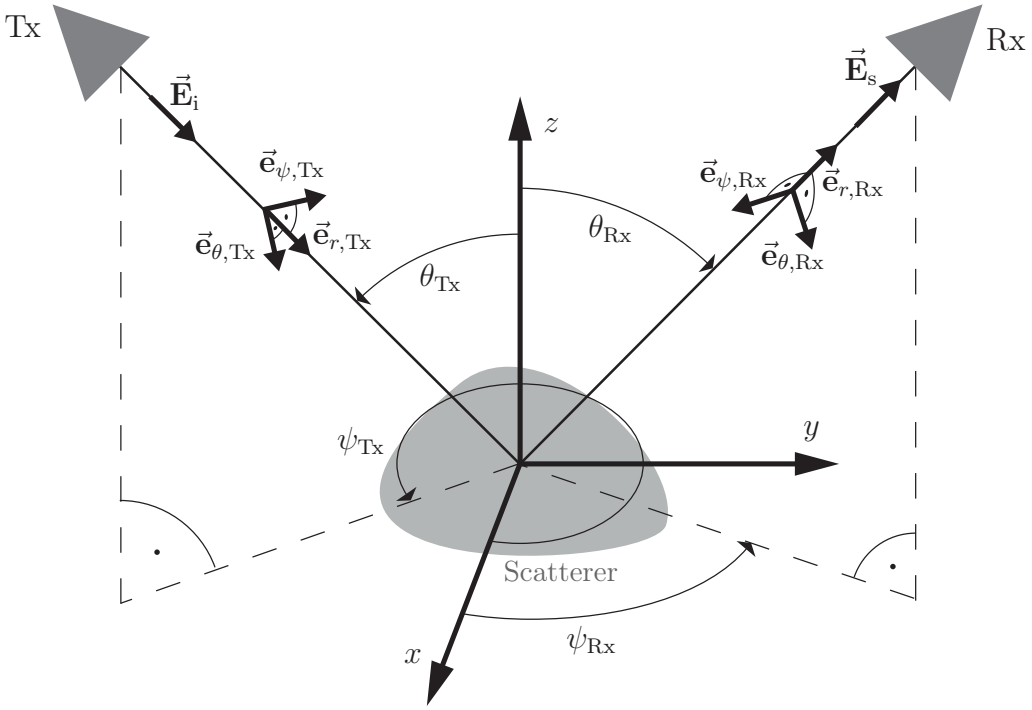

Figure 3.1: Illustration of a target scattering in a bi-static UWB Radar link.

$\vec{\mathbf{E}}_{\mathrm{s}}(f,\theta,\psi)$ which is aligned with the orientation of the Rx will be recorded. The cross-talk between both antennas shall not be considered further. In a practical scenario, this stationary content can be faded out to some degree within calibration routines. A global three dimensional Cartesian coordinate system shall be located with its origin in the scatterer. $\vec{\mathbf{E}}_{\mathrm{i}}(f,\theta,\psi)$ illuminates the scatterer with the elevation angle θ_{Tx} and with ψ_{Tx} azimuthal coordinate. Analogously, the scattered field $\vec{\mathbf{E}}_{\mathrm{s}}(f,\theta,\psi)$ is received with an elevation angle θ_{Rx} and azimuthal coordinate ψ_{Rx}. Further, it shall be assumed that the antennas are utilised in the far field and, consequently, the TEM waves can be assumed to be planar waves with negligible deviation from planarity.
Hence, the transmitting local orthogonal basis is formed by three spherical unit vectors $\vec{\mathbf{e}}_{\theta,\mathrm{Tx}}$, $\vec{\mathbf{e}}_{\psi,\mathrm{Tx}}$ and $\vec{\mathbf{e}}_{r,\mathrm{Tx}}$ which define a left-handed vector triplet.

Thus, the incident electric field can be expressed as a vectorial sum

$$\vec{\mathbf{E}}_{\mathrm{i}}(f,\theta_{\mathrm{Tx}},\psi_{\mathrm{Tx}}) = E_{\mathrm{i}}^{\psi,\mathrm{Tx}}(f,\theta_{\mathrm{Tx}},\psi_{\mathrm{Tx}})\vec{\mathbf{e}}_{\psi,\mathrm{Tx}} + E_{\mathrm{i}}^{\theta,\mathrm{Tx}}(f,\theta_{\mathrm{Tx}},\psi_{\mathrm{Tx}})\vec{\mathbf{e}}_{\theta,\mathrm{Tx}} \tag{3.1}$$

where $E_{\mathrm{i}}^{\psi,\mathrm{Tx}}$ is the component in the direction of the unit vector $\vec{\mathbf{e}}_{\psi,\mathrm{Tx}}$ and $E_{\mathrm{i}}^{\theta,\mathrm{Tx}}$ is the component in the direction of the unit vector $\vec{\mathbf{e}}_{\theta,\mathrm{Tx}}$. Analogously, the scattered electric field shall be expressed by means of the local orthogonal basis formed by the three spherical unit vectors $\vec{\mathbf{e}}_{\theta,\mathrm{Rx}}$, $\vec{\mathbf{e}}_{\psi,\mathrm{Rx}}$ and $\vec{\mathbf{e}}_{r,\mathrm{Rx}}$ which define a left-handed vector triplet. Hence, the scattered field may be expressed as

$$\vec{\mathbf{E}}_{\mathrm{s}}(f,\theta_{\mathrm{Rx}},\psi_{\mathrm{Rx}}) = E_{\mathrm{s}}^{\psi,\mathrm{Rx}}(f,\theta_{\mathrm{Rx}},\psi_{\mathrm{Rx}})\vec{\mathbf{e}}_{\psi,\mathrm{Rx}} + E_{\mathrm{s}}^{\theta,\mathrm{Rx}}(f,\theta_{\mathrm{Rx}},\psi_{\mathrm{Rx}})\vec{\mathbf{e}}_{\theta,\mathrm{Rx}} \tag{3.2}$$

where $E_{\mathrm{s}}^{\psi,\mathrm{Rx}}$ is the component in the direction of the unit vector $\vec{\mathbf{e}}_{\psi,\mathrm{Rx}}$ and $E_{\mathrm{s}}^{\theta,\mathrm{Rx}}$ is the component in the direction of the unit vector $\vec{\mathbf{e}}_{\theta,\mathrm{Rx}}$. Since the wave is a TEM wave by assumption, there is a lack on components with regard to the radial direction. For the sake of clarity, the relations of both local coordinate systems shall be summarized as

$$\begin{aligned}
&\langle \vec{\mathbf{e}}_{\theta,\mathrm{Tx}}, \vec{\mathbf{e}}_{\theta,\mathrm{Rx}} \rangle = 1, \\
&\langle \vec{\mathbf{e}}_{\psi,\mathrm{Tx}}, \vec{\mathbf{e}}_{\psi,\mathrm{Rx}} \rangle = -1, \\
&\langle \vec{\mathbf{e}}_{\theta,i}, \vec{\mathbf{e}}_{\psi,j} \rangle = 0 \quad \text{and} \quad \langle \vec{\mathbf{e}}_{\psi,i}, \vec{\mathbf{e}}_{r,j} \rangle = 0 \qquad \text{with } i,j = \mathrm{Tx} \text{ or } \mathrm{Rx}
\end{aligned}$$

where $\langle \cdot, \cdot \rangle$ is the scalar product operator between two vectors.

Under the assumption that the targets do not move too fast with regard to the hardware given recording time the antennas as well as the scatterer may be considered as LTI systems in the Radar link [112]. In this case, the electrodynamics of transmission, scattering and reception can be formally described by impulse response functions or, by means of the Fourier theorem, as transfer functions, respectively. On this basis, time-domain quantities shall be introduced which serve more appropriate as quality criteria than classical

frequency dependent quantities to gather pulse shape distortions.
In practical applications polarimetry is established by the antennas. Hence, for a full polarimetric system both antennas are designed with two ports which radiate or receive simultaneously in two orthogonal planes (a description of the employed antennas follows in the corresponding chapter). Hence, the vector valued transfer function $\vec{\mathbf{H}}_{\mathrm{Tx}}(f, \theta_{\mathrm{Tx}}, \psi_{\mathrm{Tx}})$ of the Tx with particular orientation θ_{Tx} and ψ_{Tx} according to the propagation path illustrated in Figure 3.1 can be denoted as

$$\vec{\mathbf{H}}_{\mathrm{Tx}}(f, \theta_{\mathrm{Tx}}, \psi_{\mathrm{Tx}}) = H_{\mathrm{Tx}}^{\theta,\mathrm{Tx}}(f, \theta_{\mathrm{Tx}}, \psi_{\mathrm{Tx}})\vec{\mathbf{e}}_{\theta,\mathrm{Tx}} + H_{\mathrm{Tx}}^{\psi,\mathrm{Tx}}(f, \theta_{\mathrm{Tx}}, \psi_{\mathrm{Tx}})\vec{\mathbf{e}}_{\psi,\mathrm{Tx}} \quad (3.3)$$

where $H_{\mathrm{Tx}}^{\theta,\mathrm{Tx}} = \langle \vec{\mathbf{H}}_{\mathrm{Tx}}, \vec{\mathbf{e}}_{\theta,\mathrm{Tx}} \rangle$ and $H_{\mathrm{Tx}}^{\psi,\mathrm{Tx}} = \langle \vec{\mathbf{H}}_{\mathrm{Tx}}, \vec{\mathbf{e}}_{\psi,\mathrm{Tx}} \rangle$ are the components of $\vec{\mathbf{H}}_{\mathrm{Tx}}(f, \theta_{\mathrm{Tx}}, \psi_{\mathrm{Tx}})$ in the $\vec{\mathbf{e}}_{\theta,\mathrm{Tx}}$ and $\vec{\mathbf{e}}_{\psi,\mathrm{Tx}}$ direction, respectively. Analogously, the vector valued transfer function of the Rx with θ_{Rx} and ψ_{Rx} orientation can be expressed as

$$\vec{\mathbf{H}}_{\mathrm{Rx}}(f, \theta_{\mathrm{Rx}}, \psi_{\mathrm{Rx}}) = H_{\mathrm{Rx}}^{\theta,\mathrm{Rx}}(f, \theta_{\mathrm{Rx}}, \psi_{\mathrm{Rx}})\vec{\mathbf{e}}_{\theta,\mathrm{Rx}} + H_{\mathrm{Rx}}^{\psi,\mathrm{Rx}}(f, \theta_{\mathrm{Rx}}, \psi_{\mathrm{Rx}})\vec{\mathbf{e}}_{\psi,\mathrm{Rx}} \quad (3.4)$$

with $H_{\mathrm{Rx}}^{\theta,\mathrm{Rx}} = \langle \vec{\mathbf{H}}_{\mathrm{Rx}}, \vec{\mathbf{e}}_{\theta,\mathrm{Rx}} \rangle$ and $H_{\mathrm{Rx}}^{\psi,\mathrm{Rx}} = \langle \vec{\mathbf{H}}_{\mathrm{Rx}}, \vec{\mathbf{e}}_{\psi,\mathrm{Rx}} \rangle$ as the components of $\vec{\mathbf{H}}_{\mathrm{Rx}}(f, \theta_{\mathrm{Rx}}, \psi_{\mathrm{Rx}})$ in the $\vec{\mathbf{e}}_{\theta,\mathrm{Rx}}$ and $\vec{\mathbf{e}}_{\psi,\mathrm{Rx}}$ direction, respectively. The transfer function of the scatterer which converts the transmit signal into the receive signal can be modelled as a matrix valued transfer funtion which coincides with the Sinclair scattering matrix and can be expressed in this particular scenario as

$$\mathbf{H}_{\mathrm{Sc}}(f, \theta_{\mathrm{Sc}}, \psi_{\mathrm{Sc}}) = \begin{bmatrix} H_{\mathrm{Sc}}(f, \theta_{\mathrm{Sc}}, \psi_{\mathrm{Sc}})^{\theta,\mathrm{Tx}\ \ \theta,\mathrm{Rx}} & H_{\mathrm{Sc}}(f, \theta_{\mathrm{Sc}}, \psi_{\mathrm{Sc}})^{\theta,\mathrm{Tx}\ \ \psi,\mathrm{Rx}} \\ H_{\mathrm{Sc}}(f, \theta_{\mathrm{Sc}}, \psi_{\mathrm{Sc}})^{\psi,\mathrm{Tx}\ \ \theta,\mathrm{Rx}} & H_{\mathrm{Sc}}(f, \theta_{\mathrm{Sc}}, \psi_{\mathrm{Sc}})^{\psi,\mathrm{Tx}\ \ \psi,\mathrm{Rx}} \end{bmatrix}. \quad (3.5)$$

Let $U_{\mathrm{Tx}}(f)$ be the UWB signal generated by the Radar device which stimulates the Tx, then the incident electric field at a certain distance r is [168]

$$\frac{\vec{\mathbf{E}}_{\mathrm{i}}(f, \theta_{\mathrm{Tx}}, \psi_{\mathrm{Tx}}, r)}{\sqrt{Z_0}} = \frac{\mathrm{e}^{-\mathrm{j}2\pi f r/c_0}}{2\pi r c_0}\, \vec{\mathbf{H}}_{\mathrm{Tx}}(f, \theta_{\mathrm{Tx}}, \psi_{\mathrm{Tx}})\, \mathrm{j}2\pi f\, \frac{U_{\mathrm{Tx}}(f)}{\sqrt{Z_{\mathrm{Tx}}}} \quad (3.6)$$

where Z_{Tx} is the real and frequency independent characteristic impedance of the Tx antenna and $Z_0 = 120\pi\,\Omega$ denotes the characteristic free-space impedance. By means of the Fourier theorem (3.6) can be indicated in the time domain as

$$\frac{\vec{\mathbf{e}}_{\mathrm{i}}(t,\theta_{\mathrm{Tx}},\psi_{\mathrm{Tx}},r)}{\sqrt{Z_0}} = \frac{1}{2\pi r c_0}\,\delta\left(t-\frac{r}{c_0}\right) * \vec{\mathbf{h}}_{\mathrm{Tx}}(t,\theta_{\mathrm{Tx}},\psi_{\mathrm{Tx}})\,\frac{\partial}{\partial t}\frac{u_{\mathrm{Tx}}(t)}{\sqrt{Z_{\mathrm{Tx}}}} \tag{3.7}$$

where $\vec{\mathbf{e}}_{\mathrm{i}}(t,\theta_{\mathrm{Tx}},\psi_{\mathrm{Tx}},r)$ is the incident electric field in the time domain, $\vec{\mathbf{h}}_{\mathrm{Tx}}(t,\theta_{\mathrm{Tx}},\psi_{\mathrm{Tx}})$ is the polarimetric spatio-temporal transient response of the Tx, $u_{\mathrm{Tx}}(t)$ is the Tx stimulating UWB signal in the time domain and $*$ is the convolution operator. The convolution with the Dirac function $\delta\left(t-{}^{r}/_{c_0}\right)$ respects the time delay due to the finite velocity of light c_0 and the distance r. The overall full polarimetric spatio-temporal description of a bi-static UWB Radar scattering process which fully covers the input-output relationship is hence given by [161]

$$\begin{aligned}\frac{U_{\mathrm{Rx}}(f)}{\sqrt{Z_{\mathrm{Rx}}}} = {} & \frac{\mathrm{e}^{-\mathrm{j}2\pi f r_0/c_0}}{2\pi r_0 c_0}\vec{\mathbf{H}}_{\mathrm{Rx}}(f,\theta_{\mathrm{Rx}},\psi_{\mathrm{Rx}})^{\mathrm{T}} \\ & \left(\mathbf{H}_{\mathrm{Sc}}(f,\theta_{\mathrm{Sc}},\psi_{\mathrm{Sc}})\,\vec{\mathbf{H}}_{\mathrm{Tx}}(f,\theta_{\mathrm{Tx}},\psi_{\mathrm{Tx}})\right)\mathrm{j}2\pi f\,\frac{U_{\mathrm{Tx}}(f)}{\sqrt{Z_{\mathrm{Tx}}}}\end{aligned} \tag{3.8}$$

where $U_{\mathrm{Rx}}(f)$ is the UWB signal in the frequency domain induced in the Rx, Z_{Rx} is the real and frequency independent characteristic impedance of the Rx, r_0 is the distance from the Tx antenna to the Rx by way of the scatterer and $(\cdot)^{\mathrm{T}}$ denotes the transpose operator. The polarisation states and the depolarisation effects are included in the transfer functions of the Tx, Rx and the scatterer, respectively. In the time domain (3.8) yields to

$$\begin{aligned}\frac{u_{\mathrm{Rx}}(t)}{\sqrt{Z_{\mathrm{Rx}}}} = {} & \frac{1}{2\pi r_0 c_0}\,\delta\left(t-\frac{r_0}{c_0}\right) * \vec{\mathbf{h}}_{\mathrm{Rx}}(t,\theta_{\mathrm{Rx}},\psi_{\mathrm{Rx}})^{\mathrm{T}} \\ & * \left(\mathbf{h}_{\mathrm{Sc}}(t,\theta_{\mathrm{Sc}},\psi_{\mathrm{Sc}}) * \vec{\mathbf{h}}_{\mathrm{Tx}}(t,\theta_{\mathrm{Tx}},\psi_{\mathrm{Tx}}) * \frac{\partial}{\partial t}\frac{u_{\mathrm{Tx}}(t)}{\sqrt{Z_{\mathrm{Tx}}}}\right).\end{aligned} \tag{3.9}$$

with $\vec{\mathbf{h}}_{\mathrm{Rx}}(t, \theta_{\mathrm{Rx}}, \psi_{\mathrm{Rx}})$ and $\mathbf{h}_{\mathrm{Sc}}(t, \theta_{\mathrm{Sc}}, \psi_{\mathrm{Sc}})$ as the polarimetric spatio-temporal transient response of the Rx and the full polarimetric spatio-temporal scattering matrix of the scatterer, respectively. The transmission coefficient S_{21} is finally the parameter which is measured according to the whole propagation path in practical analysis. From signal and system point of view the transmission coefficient comprises

$$S_{21}(f, \theta_{\mathrm{Tx}}, \psi_{\mathrm{Tx}}, \theta_{\mathrm{Sc}}, \psi_{\mathrm{Sc}}, \theta_{\mathrm{Rx}}, \psi_{\mathrm{Rx}}) = \frac{U_{\mathrm{Rx}}(f)}{U_{\mathrm{Tx}}(f)}. \tag{3.10}$$

With the common assumption of most practical devices that $Z_{Tx} = Z_{Rx} = 50\,\Omega$ equation (3.8) can be reformulated in vectorial notation as

$$\vec{\mathbf{S}}_{21}(f, \theta_{\mathrm{Tx}}, \psi_{\mathrm{Tx}}, \theta_{\mathrm{Sc}}, \psi_{\mathrm{Sc}}, \theta_{\mathrm{Rx}}, \psi_{\mathrm{Rx}}) = \vec{\mathbf{H}}_{\mathrm{Rx}}(f, \theta_{\mathrm{Rx}}, \psi_{\mathrm{Rx}}) \circ \left(\mathbf{H}_{\mathrm{Sc}}(f, \theta_{\mathrm{Sc}}, \psi_{\mathrm{Sc}})\, \vec{\mathbf{H}}_{\mathrm{Tx}}(f, \theta_{\mathrm{Tx}}, \psi_{\mathrm{Tx}}) \right) \frac{\mathrm{j}f}{r_0 c_0}\, \mathrm{e}^{-\mathrm{j}2\pi f r_0/c_0} \tag{3.11}$$

where the $\circ$ operator is the Hadamard product. As previously mentioned, the polarisation states of the Tx and Rx are included in the corresponding transfer functions and the scatterer is described by its scattering transfer matrix.

A polarimetric analysis of the Radar link according to the whole propagation path can be utilised as follows: Let the transmit antenna Tx be the reference antenna (REF) whose parameters are known and the receive antenna Rx be the antenna under test (AUT) which is subjected to analysis. Under these assumptions the transfer function of the AUT can be expressed as

$$\vec{\mathbf{H}}_{\mathrm{AUT}}(f, \theta_{\mathrm{Rx}}, \psi_{\mathrm{Rx}}) = \frac{r_0 c_0}{\mathrm{j}f}\, \vec{\mathbf{S}}_{21}(f, \theta_{\mathrm{Tx}}, \psi_{\mathrm{Tx}}, \theta_{\mathrm{Sc}}, \psi_{\mathrm{Sc}}, \theta_{\mathrm{Rx}}, \psi_{\mathrm{Rx}}) \circ^{-1} \left(\mathbf{H}_{\mathrm{Sc}}(f, \theta_{\mathrm{Sc}}, \psi_{\mathrm{Sc}})\, \vec{\mathbf{H}}_{\mathrm{REF}}(f, \theta_{\mathrm{Tx}}, \psi_{\mathrm{Tx}}) \right) \mathrm{e}^{\mathrm{j}2\pi f r_0/c_0} \tag{3.12}$$

where $\vec{\mathbf{H}}_{\mathrm{REF}}(f, \theta_{\mathrm{Tx}}, \psi_{\mathrm{Tx}})$ is the transfer function of the REF and the $\circ^{-1}$ operator which expresses the inverse Hadamard product.

For the case of a deterministic scatterer, e.g. a conductive sphere the scattering matrix equals an identity matrix with a specific reflection weight [158] which can be compensated within the calibration procedure. A sphere has no depolarization characteristic and its Radar signature is independent of the orientation. Hence, in this particular case the transfer function of the AUT can be recovered as

$$\vec{\mathbf{H}}_{\mathrm{AUT}}(f,\theta_{\mathrm{Rx}},\psi_{\mathrm{Rx}}) = \frac{r_0 c_0}{\mathrm{j}f}\,\vec{\mathbf{S}}_{21}(f,\theta_{\mathrm{Tx}},\psi_{\mathrm{Tx}},\theta_{\mathrm{Rx}},\psi_{\mathrm{Rx}}) \circ^{-1} \vec{\mathbf{H}}_{\mathrm{REF}}(f,\theta_{\mathrm{Tx}},\psi_{\mathrm{Tx}})\,\mathrm{e}^{\mathrm{j}2\pi f r_0/c_0} \tag{3.13}$$

which equals a two antenna measurement with mutual alignment towards each other. For the particular case that both antennas AUT and REF are identical, the transfer function of the AUT simplifies to

$$\vec{\mathbf{H}}_{\mathrm{AUT}}(f,\theta_{\mathrm{Rx}},\psi_{\mathrm{Rx}}) = \sqrt{\frac{r_0 c_0}{\mathrm{j}f}\,\vec{\mathbf{S}}_{21}(f,\theta_{\mathrm{Tx}},\psi_{\mathrm{Tx}},\theta_{\mathrm{Rx}},\psi_{\mathrm{Rx}})\mathrm{e}^{\mathrm{j}2\pi f r_0/c_0}} \tag{3.14}$$

where the square root operator is performed elementwise. In literature, this method is referred to as the two-antenna method for the extraction of the antenna transfer function [160].

3.3 Transient Behaviour Analysis

It is not too well known that UWB antenna radiation is strongly dependent on the angular direction of the radiation. In particular, for impulse based systems where the pulse width (or the coherence time, respectively) is minor or similar to the antenna dimension this effect is even more emphasised. In frequency domain this effect does not attract much significance and is mostly omitted. However, in time domain this effect is not negligible [79] and especially in super-resolution applications this effect decreases the performance significantly.

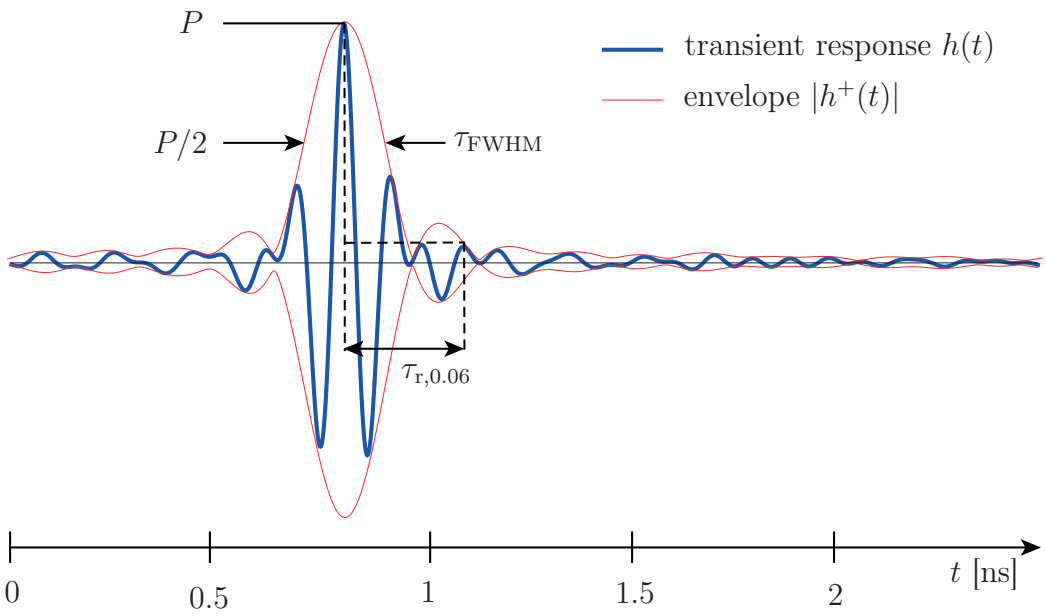

Figure 3.2: Time domain characterisation of a transient response with eligible parameters

Without loss of generality, the derived transfer function from equation (3.14) shall be notated simplified for the sake of clarity as $H^{\eta}_{\mathrm{AUT}}(f,\theta,\psi)$ where the polarisation state is expressed by the parameter η which equals θ or ψ. Consequently, $H^{\theta}_{\mathrm{AUT}} = \langle \vec{\mathbf{H}}_{\mathrm{AUT}}, \vec{\mathbf{e}}_{\theta,\mathrm{AUT}} \rangle$ and $H^{\psi}_{\mathrm{AUT}} = \langle \vec{\mathbf{H}}_{\mathrm{AUT}}, \vec{\mathbf{e}}_{\psi,\mathrm{AUT}} \rangle$ are the components of $\vec{\mathbf{H}}_{\mathrm{AUT}}$ in the $\vec{\mathbf{e}}_{\theta,\mathrm{AUT}}$ and $\vec{\mathbf{e}}_{\psi,\mathrm{AUT}}$ direction, respectively. With the inverse Fourier transformation the time domain transient response can be determined as

$$h^{\eta}_{\mathrm{AUT}}(t,\theta,\psi) \tag{3.15}$$

and the analytic transient response as

$$h^{\eta+}_{\mathrm{AUT}}(t,\theta,\psi) = \left(h^{\eta}_{\mathrm{AUT}}(t,\theta,\psi) + \mathrm{j}\,\mathcal{H}\left\{h^{\eta}_{\mathrm{AUT}}(t,\theta,\psi)\right\}\right) \tag{3.16}$$

with $\mathcal{H}$ as the Hilbert transformation operator [105]. Hence, the envelope of the transient response can be determined as $\left|h^{\eta+}_{\mathrm{AUT}}(t,\theta,\psi)\right|$ which implies the square root of signal energy distribution versus delay time and is thus a direct indication for the dispersion of the signal. In the following, three time domain quality measures shall be discussed which can be extracted directly from the transient signal or its envelope, respectively. An illustration of these quality measures are shown with an example pulse in Figure 3.2.

Peak Amplitude $P^{\eta}(\theta,\psi)$ of the envelope $\left|h^{\eta+}_{\mathrm{AUT}}(t,\theta,\psi)\right|$ is a quantity for the maximum value of the strongest peak which can be expressed mathematically as

$$P^{\eta}(\theta,\psi) = \max_{t} \left|h^{\eta+}_{\mathrm{AUT}}(t,\theta,\psi)\right|. \tag{3.17}$$

The peak amplitude is an indicator for the peak power which can be achieved in maximum. A high peak amplitude value is desirable.

Full Width at Half Maximum $\tau^{\eta}_{\mathrm{FWHM}}(\theta,\psi)$ is determined as the full width at half maximum of the envelope and can be expressed as

$$\begin{aligned}\tau^{\eta}_{\mathrm{FWHM}}(\theta,\psi) =& t_1\big|_{\left|h^{\eta+}_{\mathrm{AUT}}(t_1,\theta,\psi)\right|=P^{\eta}(\theta,\psi)/2} \\ &- t_2\big|_{t_2<t_1 \wedge \left|h^{\eta+}_{\mathrm{AUT}}(t_2,\theta,\psi)\right|=P^{\eta}(\theta,\psi)/2}.\end{aligned} \tag{3.18}$$

It describes the system's dispersive character which consequently leads to a broadening of the pulse. A low $\tau^{\eta}_{\mathrm{FWHM}}(\theta,\psi)$ is desirable.

Ringing is defined as the time duration $\tau^{\eta}_{\mathrm{r},\alpha}(\theta,\psi)$ until the envelope has decreased from the peak amplitude $P^{\eta}(\theta,\psi)$ below a fraction α of the peak amplitude and remains consistently below it:

$$\begin{aligned}\tau^{\eta}_{\mathrm{r},\alpha}(\theta,\psi) =& t_1\big|_{\left|h^{\eta+}_{\mathrm{AUT}}(t_1,\theta,\psi)\right|=\alpha P^{\eta}(\theta,\psi)} \\ &- t_2\big|_{t_2<t_1 \wedge \left|h^{\eta+}_{\mathrm{AUT}}(t_2,\theta,\psi)\right|=P^{\eta}(\theta,\psi)}\end{aligned} \tag{3.19}$$

The ringing is a quantity for undesired oscillations in the pulse after the peak point and is usually caused by resonance effects due to energy storage or multiple reflections within the antenna [168]. A low $\tau^{\eta}_{\mathrm{r},\alpha}(\theta,\psi)$ is desirable.

These time domain quality measures provide a more appropriate quantification of the signal's temporal evolution than classsical power related spectral quantities [99]. As opposed to common frequency dependent parameters which are functions over frequency, these time domain quantities are scalar features which just exhibit one single scalar to cover relevant information about signal distortions. However, time domain quantities shall serve as a complementary rather than a replacement to classical frequency domain quantities. These theoretically derived quantities serve as a basis for the development of the wavefront extraction algorithm, imaging and feature extraction algorithms in particular. In fact, the impact should also be of high significance for prospective optimisation and weakness compensation strategies of any super-resolution UWB system in general.

However, to fully capture the shape distortion of UWB pulses also the impact of the spatial domain has to be quantified and provided for subsequent algorithm developments. The angular impact has been considered throughout the analysis since the azimuth and the elevation dependency were respected in the transfer function (3.14), in the transient response (3.15) and in the derived quantities (3.17), (3.18) and (3.19), respectively. In the following, this consideration shall be confirmed with a quality measure for practical evaluations.

The spatial quantification of the signal shape distortion is performed by means of a fidelity analysis [107]. In the field of wideband operating antennas the fidelity expresses the degree of the angular dependent pulse distortion by means of a correlation operation with the mainbeam reference pulse. In

practical systems the alignment of the Radar system with regard to the target cannot be assumed ideal in any case. However, with an a priori fidelity evaluation hardware caused distortions can be separated from the echo and systematic errors can be compensated. This is essential for super-resolution systems since the variation of the received signal contains the target signature.

The fidelity analysis is performed on signals which are normalised and compensated with regard to their temporal shifts. Thus, a parameter that expresses the variation between two signals is the distortion parameter

$$\Delta_{ab} = \min_{\tau} \int \left(a_{\mathrm{n}}\left(t+\tau\right) - b_{\mathrm{n}}\left(t\right)\right)^2 \mathrm{d}t \tag{3.20}$$

with the arbitrary signals

$$a_{\mathrm{n}}\left(t\right) = \frac{a\left(t\right)}{\left\|a\left(t\right)\right\|_2}, \quad b_{\mathrm{n}}\left(t\right) = \frac{b\left(t\right)}{\left\|b\left(t\right)\right\|_2}$$

which are normalised to unitary signal energy with the Euclidean norm. The integral can be expanded by factoring out the square operator and omitting the terms which do not influence the minimum which yields

$$\Delta_{ab} = 2 \min_{\tau} \left(1 - \left| \int a_{\mathrm{n}}\left(t+\tau\right) b_{\mathrm{n}}\left(t\right) \mathrm{d}t \right| \right). \tag{3.21}$$

The maximum of the integral term is the so-called fidelity F_{ba}, i.e. the fidelity of $b\left(t\right)$ with regard to $a\left(t\right)$. Actually, the fidelity function coincides with the normalised cross correlation function (CCF) whose absolute value ranges between zero and one. For identical shapes (but not inevitably the same amplitude and same temporal position) the maximum of the CCF equals one and, consequently, the minimum distortion Δ_{ab} equals zero. Hence, it can be concluded that the more the CCF increases the more the distortion decreases.

As a quality measure the fidelity is applied onto the spatially varying incident electric field (3.7) with η polarisation induced by the Tx

$$e_{\mathrm{i}}^{\eta}(t,\theta,\psi,r) = \frac{\mathrm{C}}{r}\,\delta\left(t - \frac{r}{c_0}\right) * h_{\mathrm{Tx}}^{\eta}(t,\theta,\psi)\,\frac{\partial}{\partial t} u_{\mathrm{Tx}}(t) \tag{3.22}$$

with regard to the η polarised boresight (B) incident electric field

$$e^{\eta}_{\mathrm{i,B}}\left(t,\theta_{\mathrm{B}},\psi_{\mathrm{B}},r\right)=\frac{\mathrm{C}}{r}\,\delta\left(t-\frac{r}{c_0}\right)*h^{\eta}_{\mathrm{Tx}}\left(t,\theta_{\mathrm{B}},\psi_{\mathrm{B}}\right)\,\frac{\partial}{\partial t}u_{\mathrm{Tx}}\left(t\right) \tag{3.23}$$

of the Tx. For the sake of clarity, the constant terms are comprised in $\mathrm{C}=\sqrt{Z_0}/\sqrt{Z_{\mathrm{Tx}}}\cdot 1/2\pi c_0$ since constants do not influence the fidelity

$$F_{e^{\eta}_{\mathrm{i}}(t,\theta,\psi,r)\,e^{\eta}_{\mathrm{i,B}}(t,\theta_{\mathrm{B}},\psi_{\mathrm{B}},r)}(\theta,\psi)$$
$$=\max_{\tau}\left|\int e^{\eta}_{\mathrm{i,B}}\left(t+\tau,\theta_{\mathrm{B}},\psi_{\mathrm{B}},r\right)e^{\eta}_{\mathrm{i}}(t,\theta,\psi,r)\mathrm{d}t\right| \tag{3.24}$$

anyway. A high fidelity close to one over a large radiation and reception area is desirable.

3.4 Hardware and Measurement Setup

The ultimate test of any model is experimental validation. To highly meet the demands of practical systems and to closely match real world conditions all developed algorithms and methods described in this thesis were experimentally evaluated. The transfer from purely theoretical considerations to an executable system with at least adequate performance appeared to be enormously challenging within the research for the thesis at hand. Model based results of simulated Radar data degraded massively after compiling the developed algorithms in a real UWB Radar system. Systematic errors, non-linearities of the devices, non-ideal behaviour of the components and other unforeseen issues asked for advanced re-designs and sophisticated adaption of the algorithms.

3.4.1 Hardware and Transient Behaviour Evaluation

The operational absolute bandwidth for the development of the algorithms is 9 GHz. Starting from 4.5 GHz until the cut-off frequency 13.5 GHz results in a centre frenquency of 9 GHz with a corresponding relative bandwidth of 100%. Mostly, the algorithms are evaluated with an M-Sequence Radar. The

main idea of M-sequence technology is the utilisation of the same pseudo-random binary code as transmit signal as well as for a matched filter in the receive chain. The system clock triggers each code element by a circular shift register and thus directly synthesizes the sub-nanosecond UWB pulse. In contrast to the classical impulse radiation the M-sequence Radar equally distributes its radiation energy over the code length. Thus, high peaks are avoided which are a challenging issue from hardware design point of view [112] [114].

Partly, the algorithms were also validated with a standard laboratory vector network analyser. As expected, neither performance differences nor other noteworthy deviations compared with an M-sequence device occured. Since the focus of the thesis is the algorithm development the interested reader may be refered to the vast existing literature for detailed hardware information [112] [113] [114].

Calibration, or more precisely *system error correction* is at least as mature as Radar technology itself. No RF system can be operated without a proper calibration process. In order not to exceed the framework of this thesis, solely the main ideas and strategies of a calibration procedure shall be depicted in the following. The research on UWB calibration techniques are well exploited and documented in the literature and can be reviewed in detail e.g. in [42] [99] [100] [101]. As opposed to classical narrowband Radar systems the calibration for UWB systems can be carried out in the time domain with a couple of targets with well known reflectivity signatures (e.g. flat plates, dihedrals, spheres). The reason for a proper calibration is that substantial information is exhibited in the amplitude as well as in the phase ratio differences between both co- and cross-polarized channels. Antenna crosstalk, hardware given gain imbalances and phase delays have to be compensated to ensure that the recorded Radar data mostly consist of solely the target

signature itself.

The antenna used in this thesis exhibits a polarisation purity of 20 dB. Thus, the crosstalk between both channels of a single antenna can be neglected. The antenna crosstalk as well as phase differences between the Tx and Rx can be compensated by means of a reference measurement with a flat plate at a certain distance. Gain imbalances per channel are normalised by utilising a dihedral measurement with well known reflectivity signature. Hence, the amount of attenuation and amplification, respectively, can be assessed and a subsequent equalisation performed. Basically, if an imbalance can be quantified precisely, in most cases it can be largely corrected by a calibration procedure and misleading interpretation of the data can be avoided.

As discussed in the previous section, one of the most crucial components of a Radar system with deep impact potential are the antennas. A pair of novel dual-polarised Vivaldi based antennas are utilised for the experiments [109]. To highly meet the demands on accuracy the antennas have been exclusively developed and matched to the hardware given operational bandwith, namely from 4.5 GHz to 13.5 GHz. An illustration of the used antenna is given in Figure 3.3. To cover this huge bandwidth two tapered slot line antennas were designed on a single substrate which is completely embedded in a coned teflon body. The rod shape is designed to maintain a smoother transition of the guided wave into free space. The chosen dielectric material provides an increased gain while reducing the beam width. To gather both polarisations two substrates were integrated perpendicular to one element. The main features of the antenna which are well usable for super-resolution applications are:

- A high gain with more than 10 dBi in the main beam.
- A polarisation purity (gain difference between co and cross polarisation)

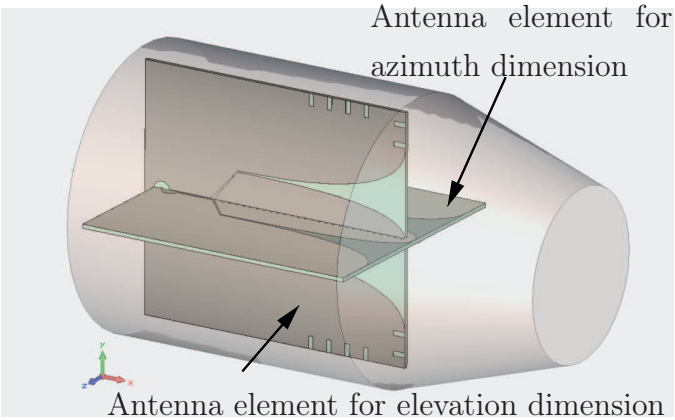

Figure 3.3: Teflon embedded dual polarised UWB antennas utilised for the validations. *(The antenna was designed and developed at the Institut für Hochfrequenztechnik und Elektronik of the Karlsruher Institut für Technologie)*

with more than 20 dB.

- An impedance matching of the antenna ports S11 and S22 with less than -10 dB.
- A decoupling of both ports with S12 and S21 less than -25 dB.
- A narrow 3 dB beam width of 30° with relatively constant gain.

A more detailed description including plots of the mentioned quantities which are omitted here for the sake of brevity can be reviewed in [139] [140]. However, as mentioned in the previous section, these classical power related parameters are not sufficient to fully assess the antenna ability and impact on wideband super-resolution operations. In fact, none of the listed quantities reveal directly (i) information about spatially dependent pulse preserving capabilities, (ii) pulse distorting antenna oscillations or (iii) favourable angular operation directions. An experimental evaluation was performed to gather

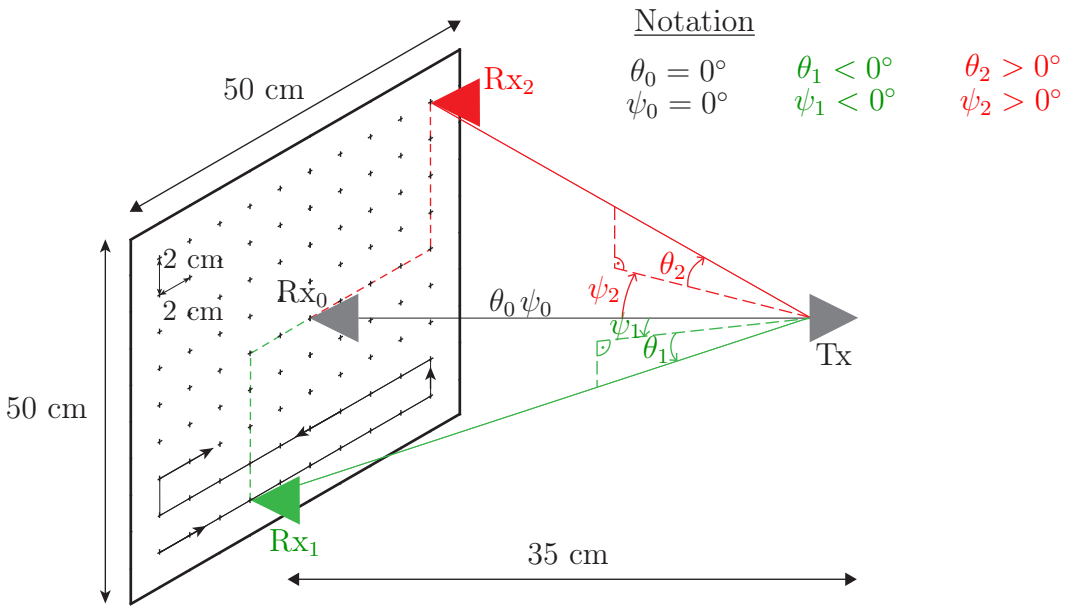

Figure 3.4: Time domain quality measure evaluation experiment.

the previously introduced time domain quality measures. For this purpose the experiment was carried out according to Figure 3.4. Both the Tx and the Rx antenna were placed in front of each other with a distance of 0.35 m. The Tx was fixed at this position and the Rx was moved at a 0.02 m intervall while both antennas keep their horizontal alignment. For the sake of brevity, at every grid point one measurement was carried out solely in the HH channel and evaluated with regard to previously introduced time domain quality measures. The results are presented in Figure 3.5 to 3.8 as colour coded images subject to the azimuth dimension ψ and the elevation dimension θ.

The antenna exhibits its best performance for $-15° < \theta < 15°$ and $-15° < \psi < 15°$ where the fidelity leads to values of $F(\theta, \psi) > 90\%$ between the signal under test and the signal in boresight, i.e $\theta = 0°$ and $\psi = 0°$.

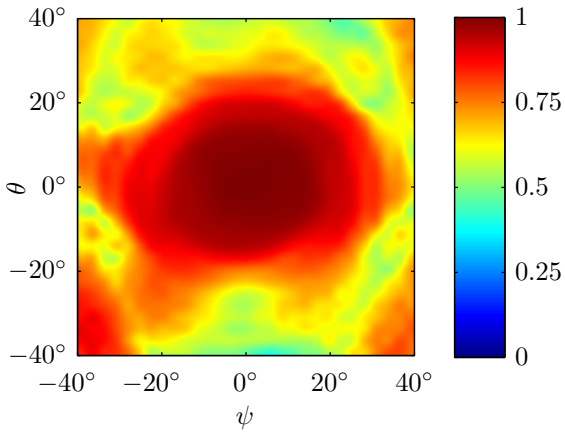

Figure 3.5: Fidelity $F(\theta, \psi)$

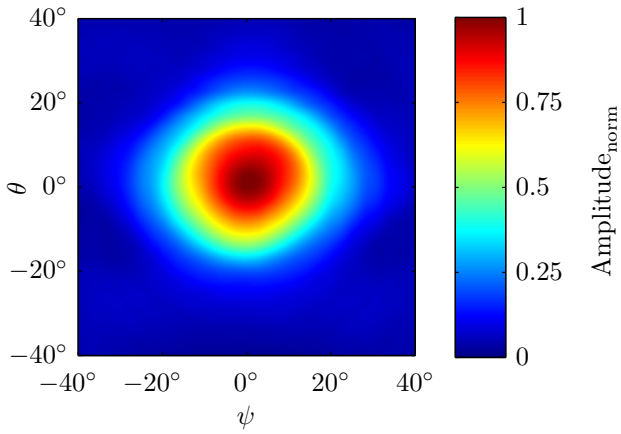

Figure 3.6: Peak amplitude $P(\theta, \psi)$

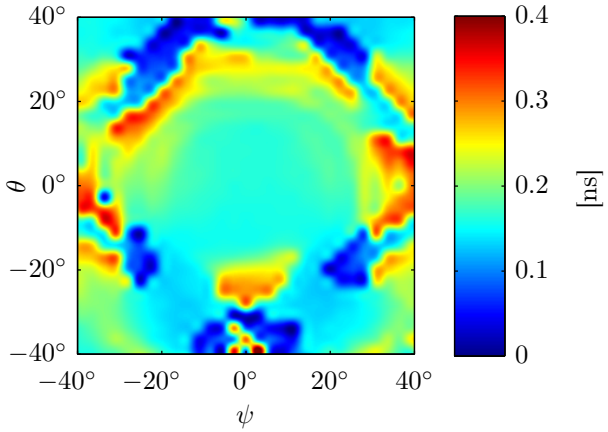

Figure 3.7: FWHM $\tau_{\mathrm{FWHM}}(\theta, \psi)$

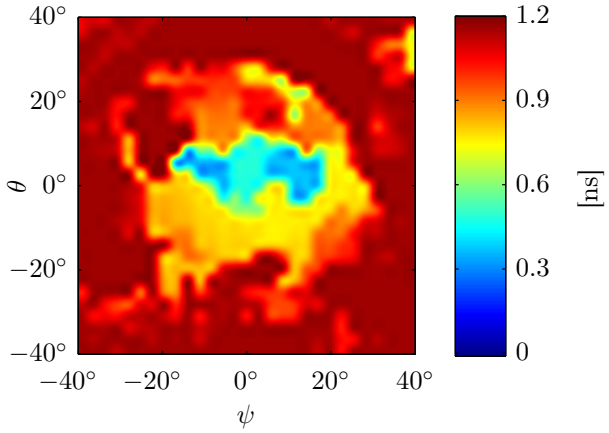

Figure 3.8: Ringing $\tau_{\mathrm{r},0.06}(\theta, \psi)$

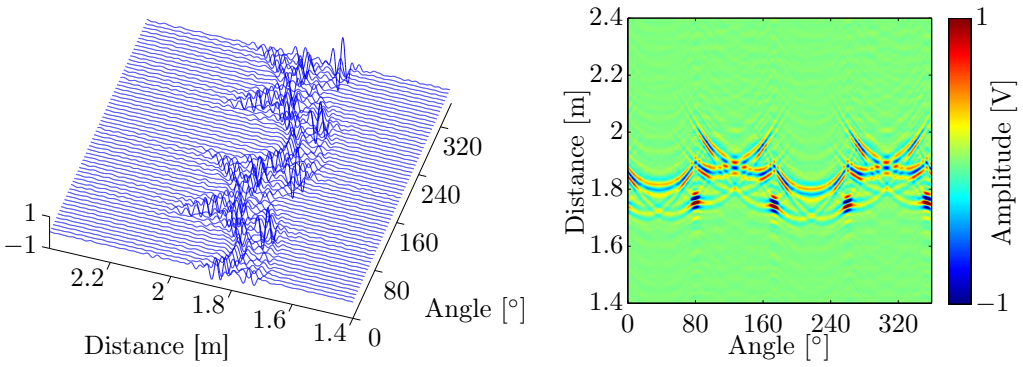

Figure 3.9: Example Radar data successively aligned (*left*) and colour coded as a radargram (*right*)

Simultaneously, in the same spatial region the normalised peak amplitude decreases approximately by 20% compared to the boresight link. Actually, both parameters the fidelity and the peak amplitude have to be analysed exclusively in conjunction; a high fidelity of a low energy signal is just as well challenging as a heavily distorted high energy signal.
In the favourable spatial region for $-15° < \theta < 15°$ and $-15° < \psi < 15°$ the full width at half maximum τ_{FWHM} is approximately 200 ps. The ringing is evaluated for a pretty severe case of $\alpha = 6\%$ to satisfy the demands of super-resolution applications. Thus, the region for this requirement $\tau_{\mathrm{r},0.06}$ slightly shrinks for an appropriate value of $\tau_{\mathrm{r},0.06} < 600$ ps compared with the region indicated by the previous parameters.

3.4.2 Measurement Setup of the Object Recognition Validation

The experimental validations have been carried out within a vast measurement campaign at the chair of communications systems of the university Duisburg-Essen. The principle framework of the measurements are circular tracks with a radius of 1 m using a 0.5° measurement grid. Such Radar data

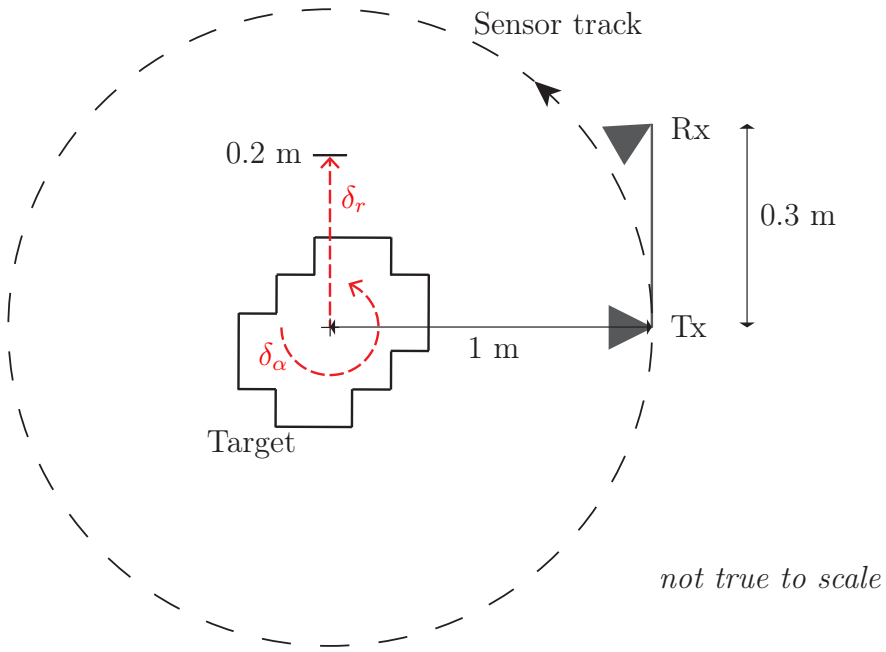

Figure 3.10: Illustration of the measurement setup for the OR validations.

can be visualised successively ordered in a three dimensional plot as shown on the left side of Figure 3.9. In this plot, the TOF corresponding distance is plotted on the ordinate, the angle in degree on the abscissa and the amplitude in the 3$^{\text{rd}}$ dimension. An alternative representation is shown on the right side of Figure 3.9 where the amplitude is RGB coded which provides an image in the form of a so-called radargram. The latter approach will be used throughout the thesis at hand.

A bi-static antenna configuration is utilised with an antenna axis length of 0.3 m. For the sake of clarity, an illustration of the measurement setup is provided in Figure 3.10 including all relevant specifications. To provide more practical relevance and to avoid too idealised specifications, the measurements for the OR validations are not performed with ideally positioned objects with a proper alignment in the centre of the track. This is just reserved for the reference measurements.

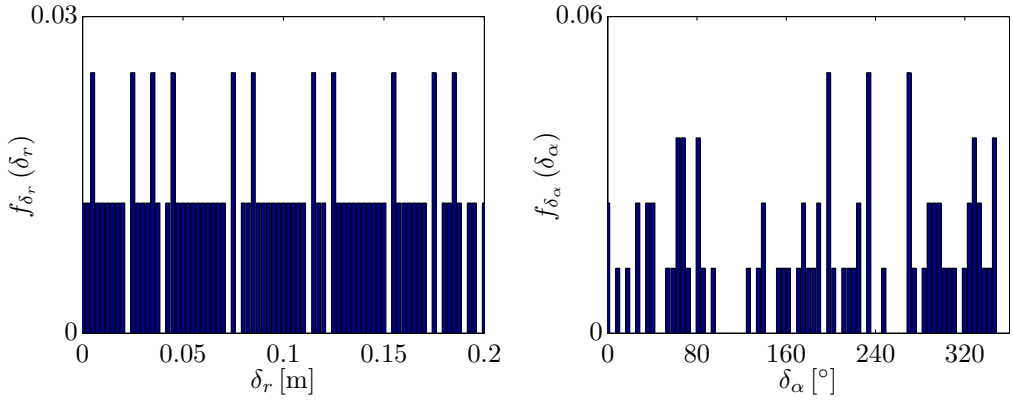

Figure 3.11: Discrete probability density function of δ_r and δ_α

Actually, the measurements under test are subject to a random translative offset δ_r up to 0.2 m from the centre of the circular track. Additionally, the orientation of the object is subject to an arbitrary offset δ_α up to 360°.

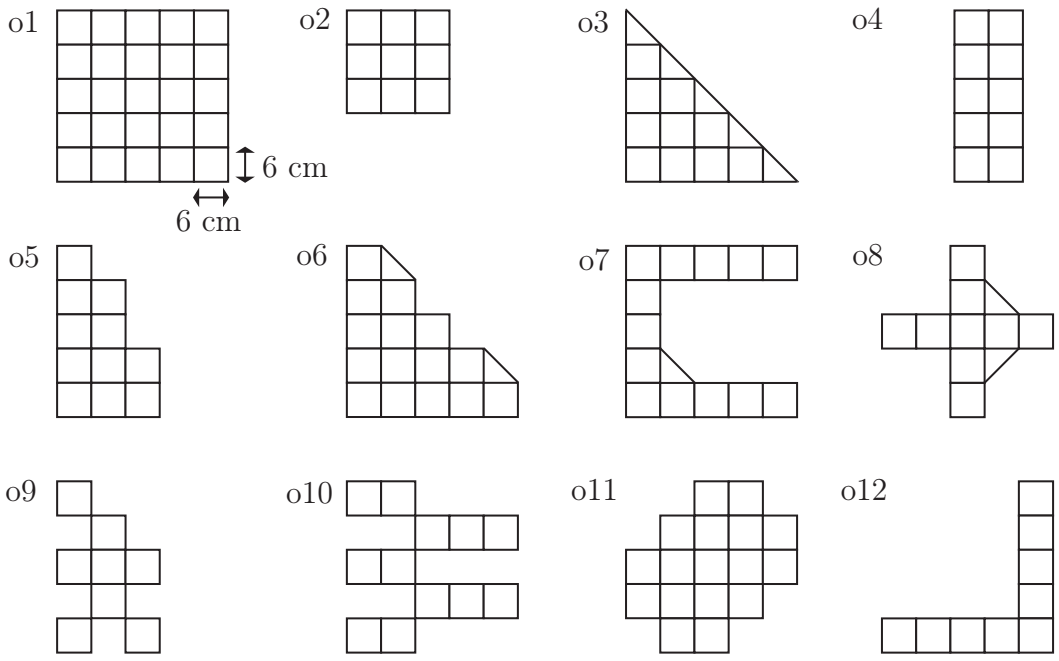

Figure 3.12: Objects under test.

Therewith, the performance of all algorithms including wavefront extraction, feature extraction and OR are subject to a non-ideal illumination due to an improper sensor track. For the sake of completeness, the probability density function of both parameters δ_r and δ_α are presented in Figure 3.11. A more or less uniform distribution of both offset parameters allow a high degree of translative and rotational diversity within the measurements. The OR is investigated with the objects depicted in Figure 3.12. They consist of simple canonical as well as polygonal complex objects in the form of beams with no variance in the 3$^{\text{rd}}$ dimension. To provide strong echoes the objects are composed of conductive material.

As a basic principle, a reference alphabet may be synthesised from a priori known information. The OR can hence be applied onto an object under test or a sample of the object to identify an element of the reference alphabet which maximises the likelihood of a correct recognition. The adoption of this principle on a UWB-Radar system and 12 uniquely defined objects results in a reference alphabet with 12 elements according to Figure 3.12. For each element data are obtained on a full circular track with the object placed in the centre. The specifications of the OR measurement campaign are as follows:

- Every object is measured 80 times fully polarimetric following a complete 360° track.
- Every measurement is subject to an arbitrary translative as well as an arbitrary rotational offset δ_r and δ_α, respectively.
- The reference feature set obtained from the objects explained later in detail consists of one full 360° track per object with neither a translative nor a rotational offset. Thus, the reference set consists of 12 elements.
- In order to investigate the OR under more severe conditions a 2$^{\text{nd}}$ series

of 80 measurements were performed with the sensor track restricted to 270°.

- To further handicap the conditions and enable a system investigation under extreme conditions a 3rd series of 80 measurements were performed with the sensor track restricted to 180°.

- Both restricted track measurements equal, except the premature stop of the track, the 80 full track measurements, particularly with equal δ_r and δ_α, respectively. This enables a fair comparison and evaluation of the whole OR system depending solely on the influence of a restriction of the sensor track.

In order to reduce the hardware effort all motions are provided by rotatable platforms and linear rails which are driven by highly accurate step motors.

FORTH CHAPTER

Wavefront Extraction

The current state of research in the theory of wavefront extraction of wideband signals has been reviewed in chapter 1.2. The discussion has revealed that the application of two algorithms have become apparent, namely

- the genetic algorithmic extraction and
- the correlation based extraction.

The former mentioned genetic algorithm for the extraction of wavefronts in UWB signals has been first published in [40] by Hantscher et al and further investigated by himself in [39]. The main idea to recover wavefronts with the genetic algorithm is to resemble the MUT as a superposition of modified reference pulses. The modification consists of (i) the estimated TOF of the wavefront and (ii) the estimated amplitude of the wavefront in terms of a weight value. Hence, 2 parameters per wavefront per MUT have to be recovered which is solved as an evolutionary optimisation task. The genetic algorithm belongs to the group of heuristic techniques which means that the search for the best parameters are performed in a 'trial and error' iterative sense. Thus, in every iteration a set of possible parameters are considered and the MUT is reassembled with reference pulses modified with the parameters. Subsequently, the set is evaluated to minimise the difference between the MUT and every reassembly of the set in the least square sense. Afterwards, the reassemblies with the highest deviation are rejected while the others are slightly modified, recombined and investigated with the same strategy in the next iteration. The wavefront extraction is terminated

as soon as the difference between the reassembly with the highest deviation and the reassembly with the lowest deviation is below an empirically chosen constant. Within the research for the thesis at hand the genetic algorithm for the extraction of wavefronts proposed by Hantscher has been investigated extensively [131] [135]. It has been established that the genetic algorithm is suboptimal for the real-time extraction of wavefronts for the following reasons:

- Hantscher investigated solely one well defined scenario with 2 water filled plastic pipes in a gas concrete wall. Thus, the number of wavefronts was assumed to be 3 - one for each pipe and the last for the surrounding wall. Hantscher used this essential a priori information to tune his genetic algorithm for a fixed search of exclusively 3 wavefronts. However, in Radar applications the number of scatterers is not known and, in principle, this nescience *is* the actual motivation for Radar applications. This means that one has to either estimate previously the number of scatterers or assume to exhibit this information a priori to finally set the parameters in the forefront. Irrespective of whether there are so many scatterers or not, the reassembly will definitely consist of the previously defined number of wavefronts. In the latter case phantom wavefronts are extracted in unwanted clutter or in the ringing range. Thus, for a blind search of wavefronts, which is the usual case for Radar applications, the algorithm is not suitable.

- In the theory of genetic algorithms the effect of getting stuck in a local minimum is well known [8] [23] [64]. In the field of the genetic optimisation for wavefront extraction this is relatively often the case because of the multimodality of interference effects. This means, a pulse can be reassembled by either one similar pulse or by two or more destructively interfering pulses. This ambiguity cannot be resolved robustly by the genetic algorithm in any case.

- The vast computational load due to the iterative 'trial and error' strategy with a high number of reassemblies exclude any real-time potential.

The latter mentioned correlation based algorithm has proven to perform superior. However, in this thesis at hand the correlation based algorithm is drastically improved to resolve scattering centres of complex edged objects which provoke pulses that overlap almost the whole pulse width. These novel algorithms are still based on the matched filtering correlation principle. Hence, the classical correlation algorithm shall be introduced first in the next section followed by two versions developed in the framework of this thesis.

4.1 Classical Correlation Method

The beginning of wavefront extraction in the field of Radar by means of correlation dates back to the field of radio astronomy in the seventies [51]. However, the transfer and adaption of these methods to separate interfering pulses in UWB signals was first proposed in [41]. The basic idea of this algorithm is to locate echoes iteratively by evaluating the normalised cross-correlation function of the MUT with a reference pulse. A reference pulse can either be obtained with a two antenna measurement where the antennas are aligned towards each other or with a reflection on a flat conductive surface. For the sake of a precise TOF evaluation a reference has to be determined due to the finite narrowness of a pulse (see the discussion in chapter 3.1). Most commonly, the peak point of the pulse serves as the reference feature for the indication of a scattering effect. Let $m_{\mathrm{ref}}(t)$ be the a priori measured reference pulse. The point in time at which the peak amplitude is exhibited can be obtained as

$$t_{\mathrm{ref,max}} = \arg\max_{t} \left(|m_{\mathrm{ref}}(t)| \right). \tag{4.1}$$

For further processing the reference pulse is shifted circularly until the peak point is located in the origin of the time-axis which yields

$$m_{\mathrm{ref,shift}}(t) = m_{\mathrm{ref}}(t + t_{\mathrm{ref,max}}). \tag{4.2}$$

Irrelevant parts of the signal are removed by means of a time domain window which results in

$$m^{\mathrm{w}}_{\mathrm{ref,shift}}(t) = m_{\mathrm{ref,shift}}(t)\,\mathrm{rect}\left(\frac{t}{T_{\mathrm{w}}}\right). \tag{4.3}$$

Here, T_{w} is the width of the rectangular window which equals $1.5\lambda_{\mathrm{c}}$ where λ_{c} is the wavelength that corresponds to the centre frequency in free space. This window ensures to compensate the ringing range in the further processing. Let $m_{\mathrm{MUT}}(t)$ be the measurement under test to be investigated. The normalised cross-correlation function $R(\tau)$ between m_{MUT} and $m^{\mathrm{w}}_{\mathrm{ref,shift}}(t)$ is carried out as

$$R_{m_{\mathrm{MUT}}\, m^{\mathrm{w}}_{\mathrm{ref,shift}}}(\tau) = \frac{\int\limits_{-\infty}^{\infty} m_{\mathrm{MUT}}(t)\, m^{\mathrm{w}}_{\mathrm{ref,shift}}(t-\tau)\mathrm{d}t}{\|m_{\mathrm{MUT}}(t)\|_2 \left\|m^{\mathrm{w}}_{\mathrm{ref,shift}}(t)\right\|_2} \tag{4.4}$$

where τ is the time delay parameter and $\|\cdot\|_2$ is the Euclidean norm operator. The point in delay time

$$\tau_{\mathrm{max}} = \arg\max_{\tau}\left(R_{m_{\mathrm{MUT}}\, m^{\mathrm{w}}_{\mathrm{ref,shift}}}(\tau)\right) \tag{4.5}$$

where the maximum of the cross-correlation function is reached indicates the temporal shift at which $m^{\mathrm{w}}_{\mathrm{ref,shift}}(t)$ has the highest similarity within $m_{\mathrm{MUT}}(t)$. A scaling factor

$$s = \max_{t}\left|m_{\mathrm{MUT}}(t)\right| / \max_{t}\left|m^{\mathrm{w}}_{\mathrm{ref,shift}}(t)\right| \tag{4.6}$$

is determined which is the relation of the maximum of the MUT and the maximum of the reference pulse. Subsequently, this scaling factor is applied onto the reference pulse which is shifted by τ_{max} to exhibit highest similarity

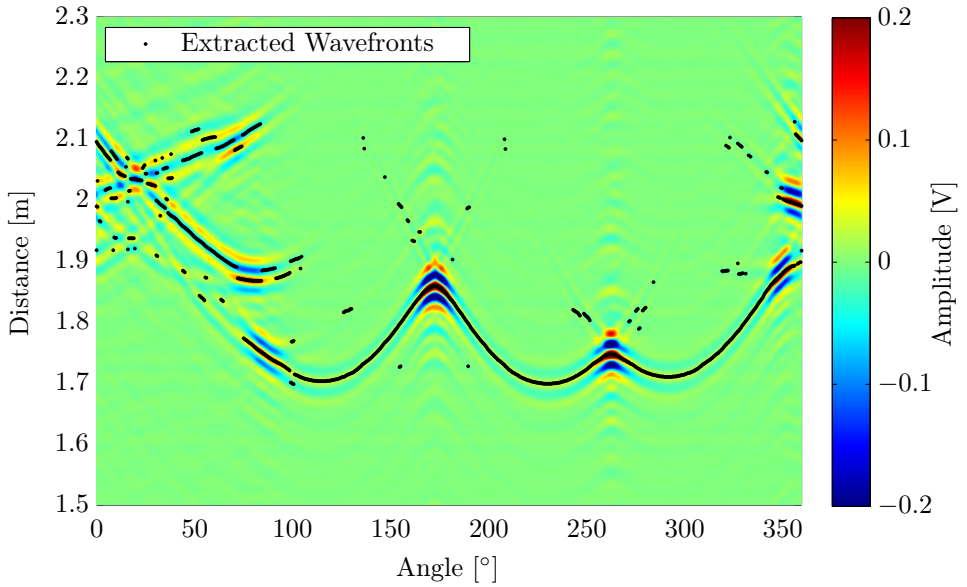

Figure 4.1: Extracted wavefronts by the classical correlation method for object o5

with the MUT. A substraction operation provides the remaining part of the MUT as

$$\bar{m}_{\mathrm{MUT}}(t) = m_{\mathrm{MUT}}(t) - s \cdot m_{\mathrm{ref,shift}}(t - \tau_{\max}) \tag{4.7}$$

after removing the extracted wavefront. Note here, that the whole temporal signature shall be removed from the MUT. A termination condition can be evaluated either with a signal energy comparison in the least squares sense and a certain threshold or by evaluating the absolute value of the normalised correlation coefficient. In the event of a negative termination evaluation the search for a further wavefront is carried out in the next iteration by applying the equation (4.4) and the adjacent ones onto $\bar{m}_{\mathrm{MUT}}(t)$.

In Figure 4.1 the result of the classical correlation method applied on the object o5 is shown. The object is not subject to an offset, i.e. $\delta_r = \delta_\alpha = 0$. The correlation coefficient is evaluated as a termination condition. In this particular case, as long as the coefficient exhibits a value more than 0.5

another iteration is carried out according to the proposed strategy in [41].

4.2 Improvement I - Dynamic Correlation Method

The classical correlation method performs most robust in the case of smooth curved simple objects where just a single reflection is induced, e.g. objects o1 to o4 or convex and concave shaped objects. Alternatively, it performs adequate when at least the number of scatterers are known a priori.
The main drawbacks of the classical correlation method are twofold:

- The classical correlation method searches for wavefronts with a fixed temporal evolution of a single reference pulse. However, a MUT might be composed of an echo with a superposition of several reradiated pulses depending on the contour of the object and the scattering centres, respectively. In that case, the resulting MUT exhibits a temporal evolution which has actually less in common with the reference pulse. This undertaking is the more handicaped (i) the more wavefronts are composed of in the MUT and (ii) the more the nearby pulses overlap. Hence, under severe interference circumstances the classical correlation method cannot resolve multiple wavefronts.

- The fixed termination threshold does not adapt to scenarios which exhibit various energy levels. Within the progress of the classical correlation method the signal energy decreases due to the substraction operator but the threshold value keeps constant. Both the evaluation of the energy comparator and the evaluation of the correlation coefficient need to be adapted since both features vary for multiple wavefronts in one MUT. The reason is that the substraction of one shifted and weighted reference pulse from a superposition of several pulses also removes contents of other wavefronts which have to be extracted in the further iterations.

One of the thesis goals is to perform super-resolution applications applied on utmost complex objects whose echoes consist of pulses which overlap almost the whole pulse width. Due to the lack of satisfying algorithms a novel wavefront extraction algorithm has been developed [135] within the research for the thesis at hand. In the following, the dynamic correlation method (DCM) shall be introduced. Starting with the same reference pulse of equation (4.3) which is windowed and shifted to the origin of the time scale a design of a synthetic waveform yields

$$m_{\mathrm{ref,syn}}(t, \tau_{\mathrm{syn}}) = m^{\mathrm{w}}_{\mathrm{ref,shift}}(t) + m^{\mathrm{w}}_{\mathrm{ref,shift}}(t - \tau_{\mathrm{syn}}) \tag{4.8}$$

where τ_{syn} equals a time retardation. Hence, the new synthetic waveform consists of a set of synthetic reference pulses which are designed by a superposition of a former reference pulse and a delayed duplicate. One synthetic reference pulse is distinguished from the others by exhibiting a different delay τ_{syn}. Thus, interference effects are respected by taking into account the consequential interference patterns. Hence, the correlation based similarity search is extended to a 2 dimensional normalised cross correlation operation

$$R_{m_{\mathrm{MUT}}\, m_{\mathrm{ref,syn}}}(\tau, \tau_{\mathrm{syn}}) = \frac{\int_{-\infty}^{\infty} m_{\mathrm{MUT}}(t)\, m_{\mathrm{ref,syn}}(t - \tau, \tau_{\mathrm{syn}})\mathrm{d}t}{\|m_{\mathrm{MUT}}(t)\|_2 \, \|m_{\mathrm{ref,syn}}(t, \tau_{\mathrm{syn}})\|_2} \tag{4.9}$$

which depends both on the classical delay parameter τ of the cross correlation and the delay time τ_{syn} of the synthetic waveform itself. In other words, one cross correlation is carried out for each synthetic reference pulse. Consequently, the highest degree of similarity is obtained in the global maximum of the correlation result which depends on 2 parameters, namely

$$\tau_{\max}, \tau_{\mathrm{syn}_{\max}} = \arg\max_{\tau, \tau_{\mathrm{syn}}} \left(R_{m_{\mathrm{MUT}}\, m_{\mathrm{ref,syn}}}(\tau, \tau_{\mathrm{syn}}) \right). \tag{4.10}$$

Both parameters indicate up to 2 wavefronts with the following quantification:

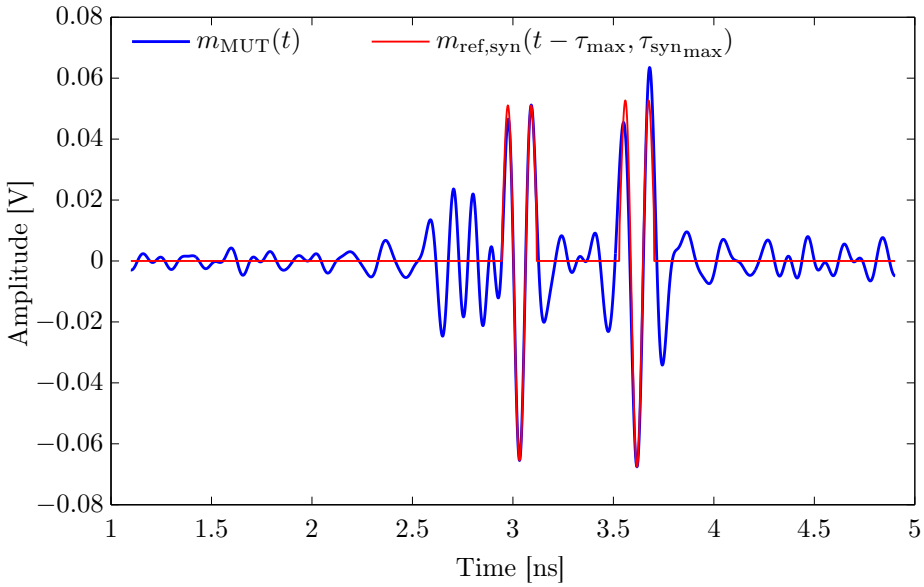

Figure 4.2: Two extracted wavefronts with the synthetic reference waveform

- 1^{st} wavefront at τ_{max}
- 2^{nd} wavefront at $\tau_{\mathrm{max}} + \tau_{\mathrm{syn}_{\mathrm{max}}}$

In the case that $0 \lesssim \tau_{\mathrm{syn}_{\mathrm{max}}} \lesssim T_{\mathrm{pw}}/2$ with the pulsewidth $T_{\mathrm{pw}} \approx 1/B$ solely a single extracted wavefront located at τ_{max} can be assumed and the algorithm can be terminated.
In Figure 4.2 the result of this processing is depicted with the MUT and a synthetic reference pulse synthesised with τ_{max} and $\tau_{\mathrm{max}} + \tau_{\mathrm{syn}_{\mathrm{max}}}$.
For further wavefronts in the next iteration a window is defined as follows:

$$w(t) = \begin{cases} 1, & \text{for} \quad m_{\mathrm{ref,syn}}(t-\tau_{\mathrm{max}},\tau_{\mathrm{syn}_{\mathrm{max}}}) \neq 0 \\ 0, & \text{for} \quad m_{\mathrm{ref,syn}}(t-\tau_{\mathrm{max}},\tau_{\mathrm{syn}_{\mathrm{max}}}) = 0. \end{cases} \tag{4.11}$$

This window equals 1 in the time samples at the extracted wavefronts and 0 else. For the sake of a better overview, the MUT of Figure 4.2 is shown with

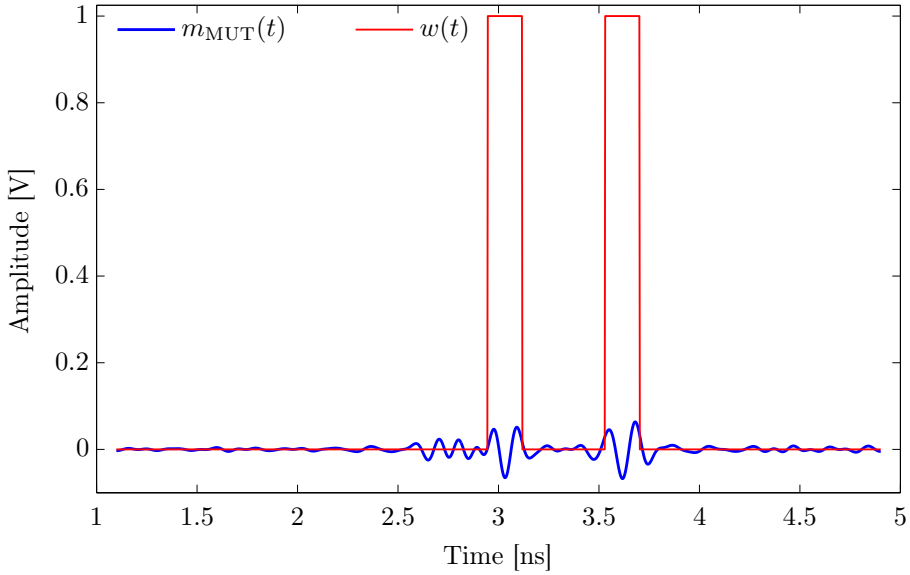

Figure 4.3: Windowing operation at the extracted wavefronts

the particularly designed window in Figure 4.3. As opposed to the classical correlation method an improved termination condition needs to be adapted to the actually processed MUT in every iteration. Thus, in order to avoid a static condition an adaptive energy comparison shall be performed. For this purpose, a synthetic MUT

$$m_{\mathrm{MUT,syn}}(t) = m_{\mathrm{ref,shift}}(t - \tau_{\max}) + m_{\mathrm{ref,shift}}(t - \tau_{\max} - \tau_{\mathrm{syn}_{\max}}) \tag{4.12}$$

is synthesised out of reference pulses at the time instances of the extracted pulses. Note here, that the non-windowed $m_{\mathrm{ref,shift}}(t)$ reference pulses are utilised to assimilate the real signature as a whole.

A normalisation and an adaption of the synthetic MUT is performed according to the power level of the MUT at the time instances of the windowed and extracted pulses as

$$m^{\mathrm{norm}}_{\mathrm{MUT,syn}}(t) = m_{\mathrm{MUT,syn}}(t) \frac{\|m_{\mathrm{MUT}}(t) \cdot w(t)\|_2}{\|m_{\mathrm{MUT,syn}}(t) \cdot w(t)\|_2}. \tag{4.13}$$

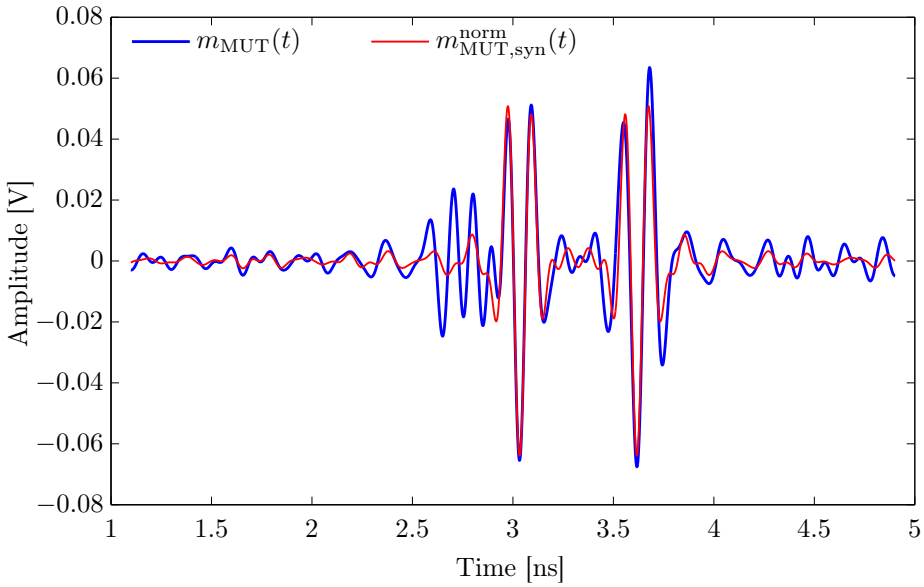

Figure 4.4: The synthetic MUT waveform with equalised power level

This step provides that $m^{\mathrm{norm}}_{\mathrm{MUT,syn}}(t)$ shows the same peak levels as $m_{\mathrm{MUT}}(t)$ after applying the window $w(t)$. An illustration of the MUT and the corresponding $m^{\mathrm{norm}}_{\mathrm{MUT,syn}}(t)$ is depicted in Figure 4.4. Depending on the energy comparison between $m_{\mathrm{MUT}}(t)$ and $m^{\mathrm{norm}}_{\mathrm{MUT,syn}}(t)$ according to

$$\|m_{\mathrm{MUT}}(t)\|_2 \gtrsim \left\|m^{\mathrm{norm}}_{\mathrm{MUT,syn}}(t)\right\|_2 \tag{4.14}$$

further wavefronts have to be extracted and the wavefront extraction algorithm is repeated for the remaining parts of the signal.
Therefore, $m_{\mathrm{MUT,syn}}(t)$ can be windowed with the inverted window $w_{\mathrm{invert}}(t) = 1 - w(t)$ to extract the remaining parts of the signal which is illustrated in Figure 4.5. Thus, $\bar{m}_{\mathrm{MUT}}(t) = m_{\mathrm{MUT}}(t) \cdot w_{\mathrm{invert}}(t)$ can be investigated for further wavefronts in the next iteration by applying the equation (4.9) and the adjacent ones onto $\bar{m}_{\mathrm{MUT}}(t)$. In this particular case a 3$^{\mathrm{rd}}$ wavefront is extracted and finally the algorithm is terminated for the MUT.

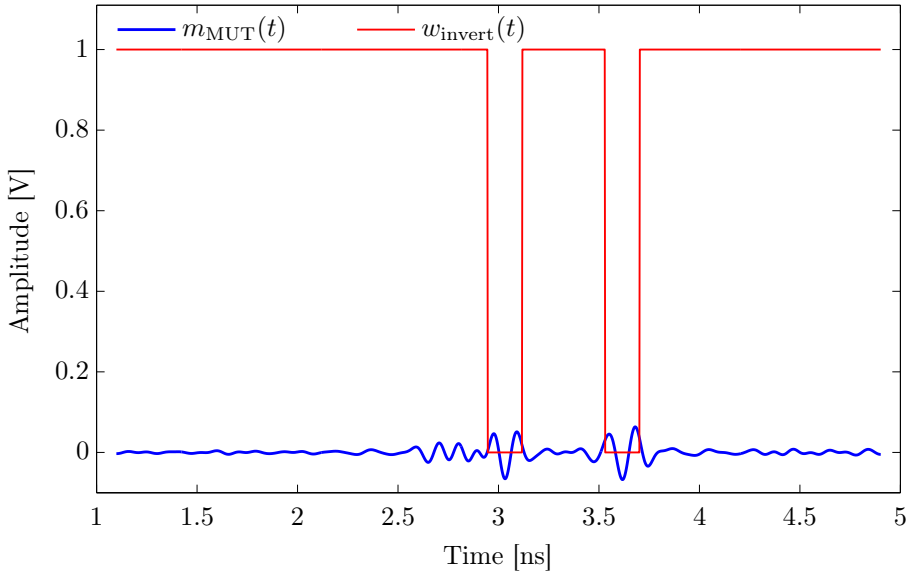

Figure 4.5: Application of the inverted window

The corresponding result can be reviewed in Figure 4.6. In comparison with the classical correlation method, the main differences of the DCM are:

- The iterative search with a synthetic waveform which respects the interference pattern. Hence, severely overlapping pulses are separated more robustly since the resulting superposed time evolution is synthesised as a whole.

- A substraction operation of extracted wavefronts is avoided since a substraction always removes non associated parts of other wavefronts. Instead, the time samples of already extracted wavefronts are marked and avoided in the subsequent iterations.

- A termination condition is carried out with a synthetic MUT which is adapted to the MUT of the actual iteration in terms of an energy adaption. The adaptive termination of the DCM outperforms the fixed

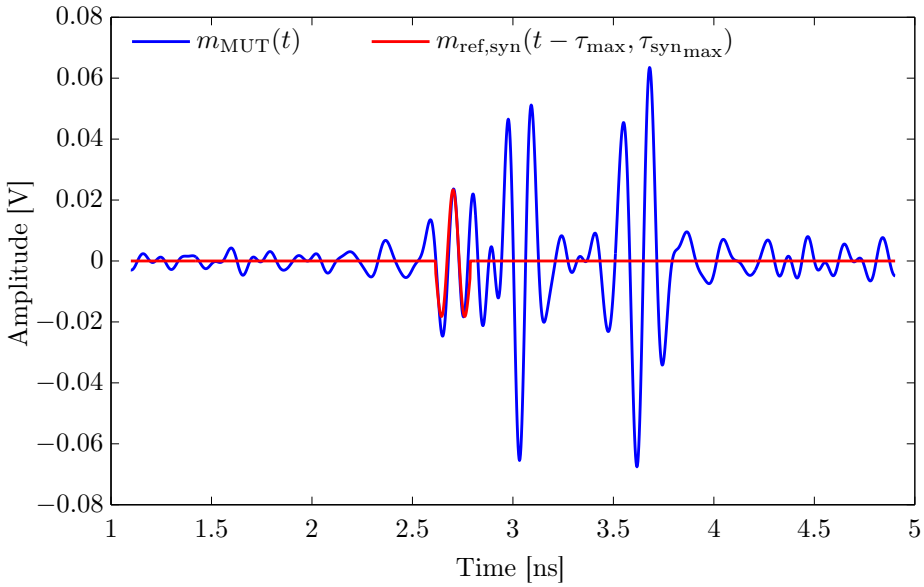

Figure 4.6: 3rd extracted wavefront in the iterative search

termination condition of the classical correlation method in a way, that even weaker wavefronts are extracted in subsequent iterations.

For the sake of a meaningful comparison, the same measurement of Figure 4.1 is processed with the DCM. The result is shown in Figure 4.7.

4.3 Improvement II - Polarimetric Dynamic Correlation Method

The objects under test except the first four ones consist of corner as well as dihedral structures which shall be precisely extracted for the long-term objective of an OR. It is well known, that edges induce weak diffuse scattering with an omni radiation characteristic. Whereas, dihedral corner structures cause, due to the mutual orthogonality of the surfaces, an internal specular reflection and a strong output radiation. Depending on the length of the

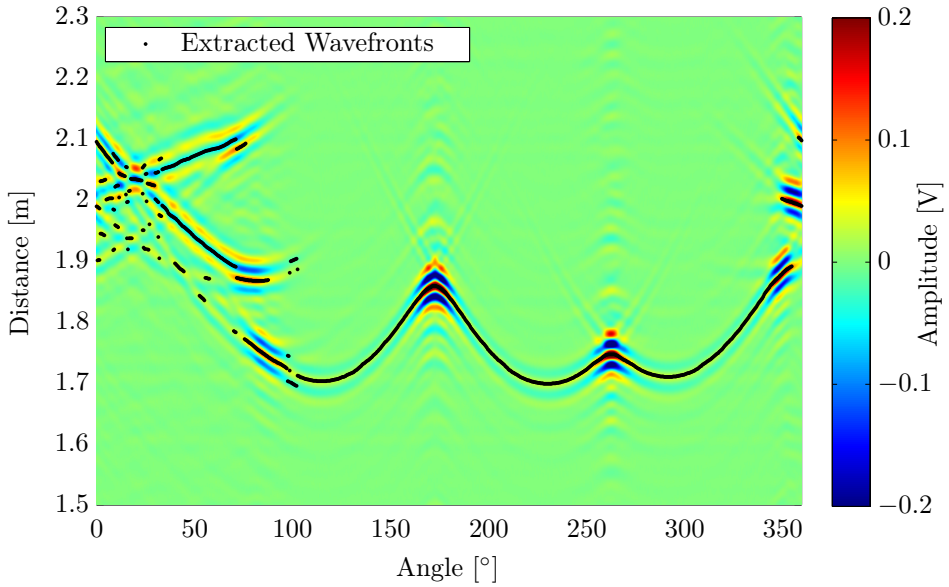

Figure 4.7: Extracted wavefronts by the dynamic correlation method for object o5

edge and the operational frequencies the difference may be more than 10 dB. An approximation of the RCS for both geometries can be found in the literature [158]. The RCS of a dihedral approximates $4\pi A_{\text{eff}}^2/\lambda^2$ where A_{eff} is the "[...] effective area contributing to multiple internal reflections." The RCS of a straight edge can be estimated as l^2/π with the edge length l. It is obvious that the RCS of a dihedral may be larger the more extended the geometry is (due to increased A_{eff}) and the higher the frequencies are. In fact, "[...] the RCS of a corner reflector seen along its axis of symmetry is identically that of a flat plate whose physical area matches the effective area of the corner reflector." [158]
Thus, effectively the echoes of the complex objects are composed of weak diffuse scattering contributions which are masked by strong specular reflections.

In chapter 2.3 the Pauli scattering matrix decomposition has been introduced

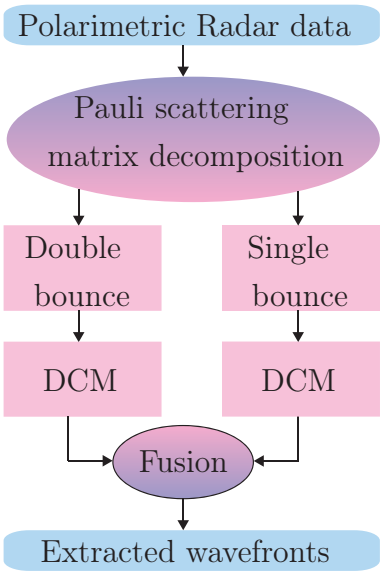

Figure 4.8: Flow chart of the polarimetric dynamic correlation method.

which allows to break down the fully polarimetric backscattering signature into a sum of elementary scattering contributions. For the sake of an improvement of the DCM the first two elements of the Pauli vector $\vec{\mathbf{k}}_{\mathrm{P}}$ which correspond to single bounce and double bounce, respectively, are computed for the MUT. Consequently, the amount of the Radar data is doubled compared with a mono-polarised system. The preferences of the joint polarimetric decomposition theorem and the DCM for the sake of wavefront extraction are in particular:

- By means of the decomposition weak scattering contributions are isolated and not masked any more by strong specular reflections. Especially with regard to the synthetic waveform in (4.8) an improvement can be achieved. By means of a decomposition energetic unbalanced contributions are disjoined and can be processed independently.

- In the case of a mono-polarised system a dihedral return exhibits a

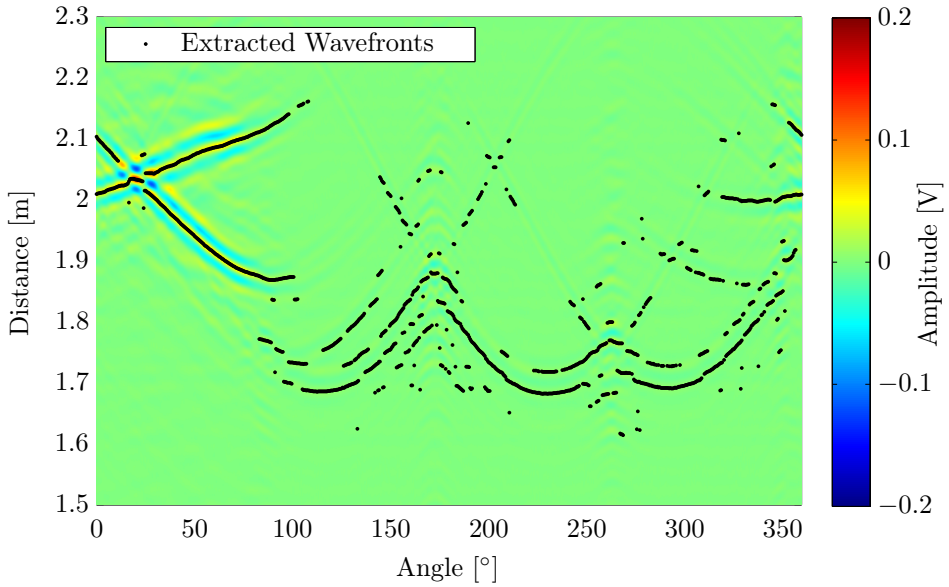

Figure 4.9: Extracted wavefronts by the polarimetric dynamic correlation method for object o5 - Double bounce

change of sign compared with a single bounce return [99]. This means, scattering may occur at positive peaks as well as negative peaks. This bi-polarity feature is not exclusively covered with the DCM because the DCM utilises a pair of peaks with same peak polarity. By means of a decomposition this bi-polarity feature reduces to a simple mono-polarity issue and creates processing conditions for enhanced accuracy.

The precise processing of the polarimetric dynamic correlation method (PDCM) is given in the flowchart illustrated in Figure 4.8. In contrast to the DCM the PDCM imperatively requires polarimetric Radar data. However, the PDCM is based on the DCM and hence the similarities are large. After applying the Pauli scattering matrix decomposition onto the Radar data a couple of decomposed data sets is provided, each for single bounce contributions and double bounce contributions, respectively. Afterwards, the DCM is per-

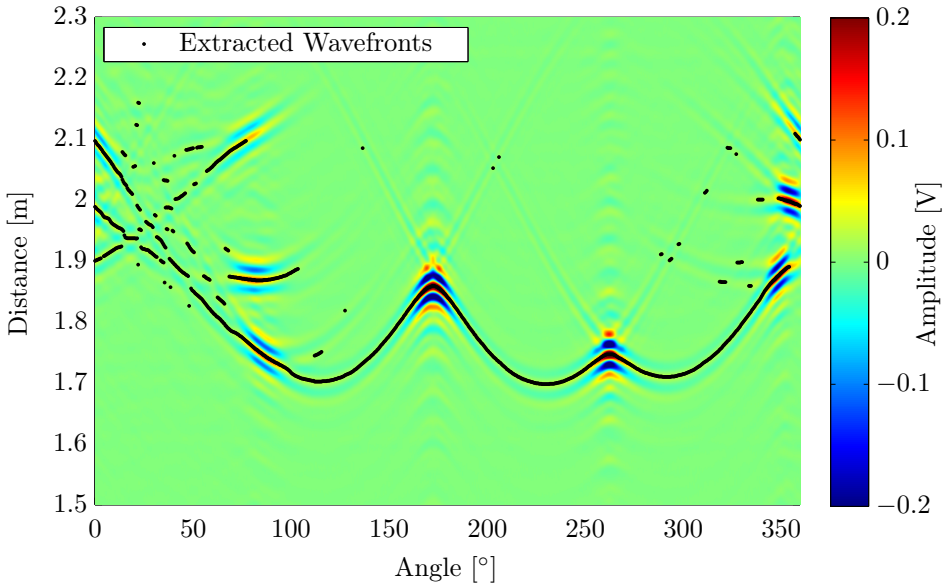

Figure 4.10: Extracted wavefronts by the polarimetric dynamic correlation method for object o5 - Single bounce

formed on both data sets separately which results in a couple of wavefront sets. In conclusion, the final set of extracted wavefronts of the MUT is provided by the fusion of both partial sets. The fusion is carried out by taking the wavefront distance information of both (if existent) the single bounce contribution and the double bounce contributions for a single measurement point and apply an or-operator on both to relate them jointly to that measurement point. Subsequently, the Radar system exhibits both wavefronts for a single antenna track. This is performed successively for each measurement point. For the sake of comparison, the wavefronts of the same object in the previous sections are processed with the PDCM. The result for the double bounce decomposition is shown in Figure 4.9 and the corresponding result for the single bounce decomposition is shown in Figure 4.10, respectively.

4.4 Improvement III - Optimisation in the Slow Time Dimension

In the field of UWB the term 'time' needs to be quantified more precisely. Due to the fine time resolution two time evolutions have to be taken into account. In the literature the terminology *fast time* and *slow time* are established. Fast time is called the actual time progress within a single measurement. Hence, the temporal elaboration of the EM wave from the Tx to the Rx by a possible scatterer is referred to as the fast time. This effect takes place with the velocity of light c_0 which finally contributes to the terminology *fast time*. On the contrary, slow time represents the time variance of the scenario or the channel, respectively. In the particular case of short-range UWB-Radar this time variance is caused by the motion of the antennas and hence different measurement points. The scenario under test can be considered stationary over the fast time while the measured target physically interacts with the wave. Due to the equiangular grid of the circular track the slow time is expressed as the angle of the covered track in this thesis.

So far, the optimisation of the classical wavefront extraction with the DCM and the PDCM is restricted to the fast time; one or multiple wavefronts have to be recovered within one measurement as precise as possible. However, an optimisation by means of wavefront history evaluation or an optimisation in the slow time dimension is feasible and shall be introduced in the following. The scanning grid which equals a spatial sampling has to fulfill certain requirements, namely the Nyquist theorem. In [85] the spatial sampling criteria of a versatile Radar system is investigated in detail and the required sampling steps to satisfy the Nyquist theorem are given. In order to not exceed the framework, the interested reader may be referred to the reference. Up to now, under the assumption of a fine measurement grid it can be seen in the radargrams that the change of the signal and radiation signature occurs

smoothly. Hence, the history of the Radar data provides information which contributes to enhanced processing potential.
The optimisation in the slow time dimension is applied separately on both chains of the PDCM after the DCM operation and before the fusion. In particular the optimisation algorithm consists of the following steps:

1. Nearby wavefronts are clustered. Every wavefront is consecutively processed and merged to a cluster if the distance to the cluster is less than half of the pulsewidth $T_{\mathrm{pw}} \approx 1/B$. Otherwise, if the distance is larger the wavefront under test starts a new cluster.

2. Due to the successive fine grid of the measurement points a cluster exhibits a smoothly curved shapes. Hence, every cluster is resembled with a polynomial curve fitting algorithm of the degree 4. For this purpose the MATLAB functions *polyfit* and *polyval* are used.

3. Gaps in the wavefront are detected by the comparison of the wavefront and the polynomial fitted curve. Gaps are substituted with interim wavefronts.
   Spikes are isolated wavefronts which exhibit a larger distance than half of the pulsewidth to the wavefront and the polynomial fitted curve. Spikes are shifted to the wavefront or removed if they exhibit unrealistic distances to the wavefront or the polynomial fitted curve.

4. Finally, every cluster with less than a minimum number of wavefront points are removed. In this work this minimum number was chosen to be 15.

Due to the antennas finite polarisation purity of approximately 20 dB also very weak scattering centres are located outside dihedral structures in the double bounce chain (see Figure 4.9). However, the signal energy of those phantom wavefronts are slightly above the noise floor. An energy evaluating filter which removes phantom wavefronts which are attenuated 15 dB or more

than the peak wavefront is applied onto the double bounce wavefront set as well as onto the single bounce wavefront set.

The results for the optimised single bounce chain, the optimised double bounce chain and the final fusioned PDCM result with the slow time optimisation are depicted in Figure 4.11, 4.12 and 4.13, respectively. For the sake of clarity, the results for the classical correlation method and the PDCM result with the slow time optimisation for the more complex object o11 is depicted in 4.14 and 4.15, respectively. The degree of the 3 levels of improvement can also be regarded clearly by comparing Figure 4.1 to Figure 4.13.

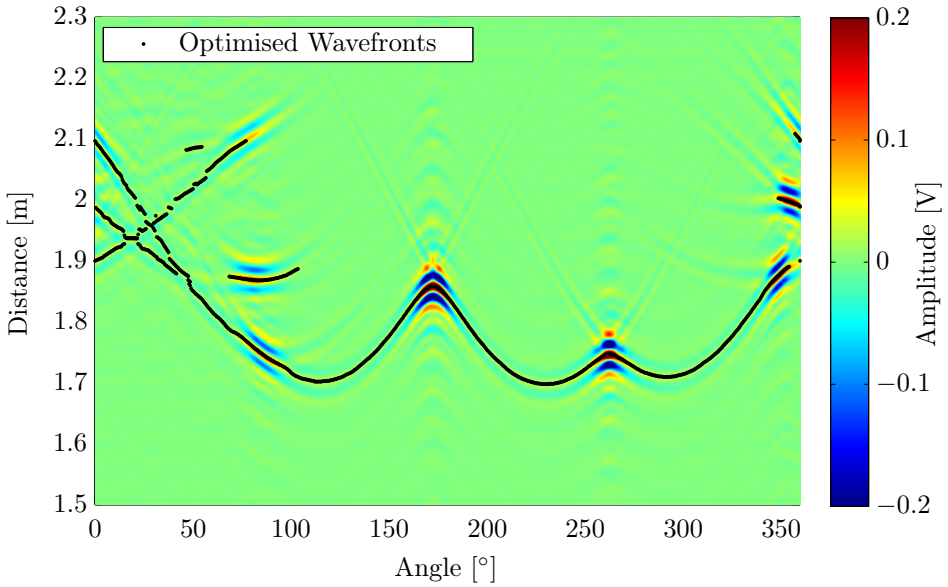

Figure 4.11: Optimised wavefronts for object o5 - Single bounce

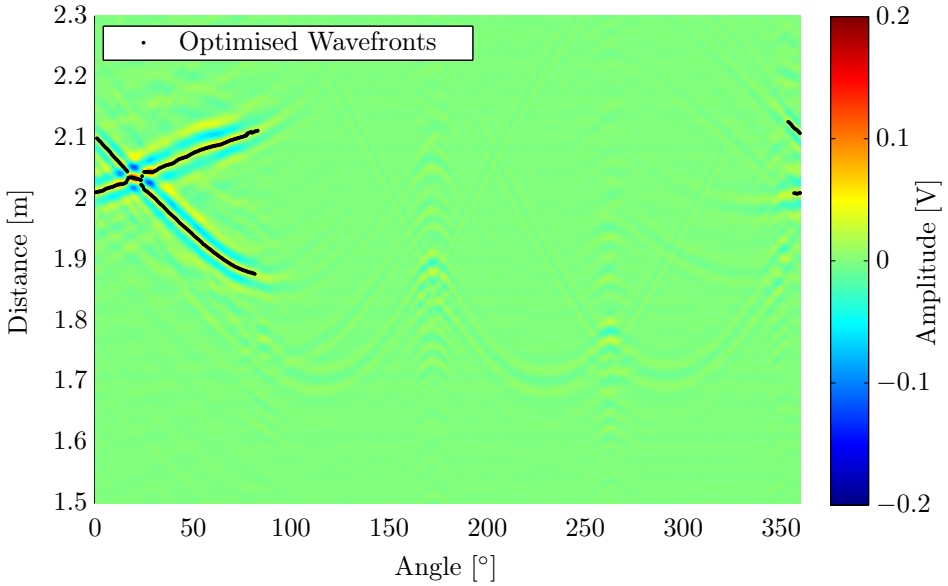

Figure 4.12: Optimised wavefronts for object o5 - Double bounce

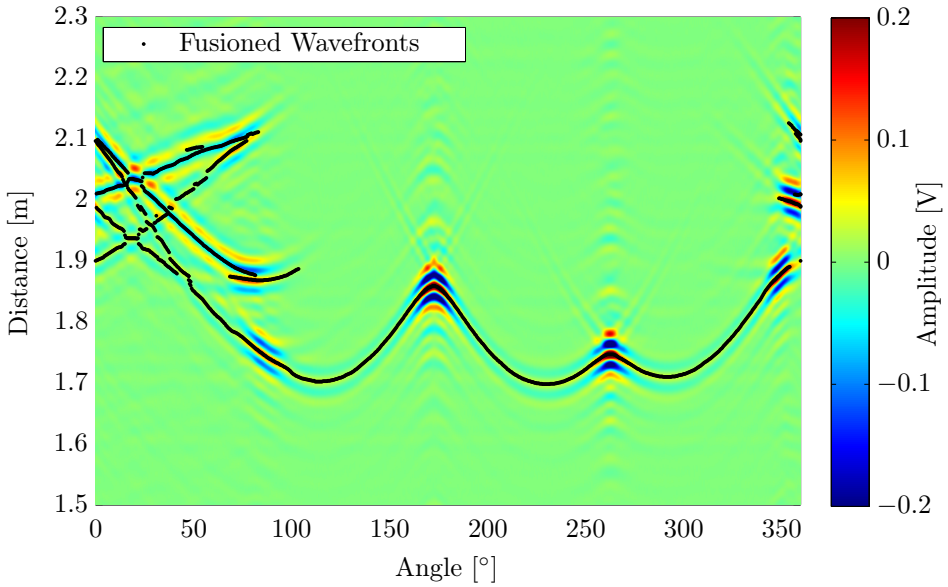

Figure 4.13: Optimised and fusioned wavefronts for object o5

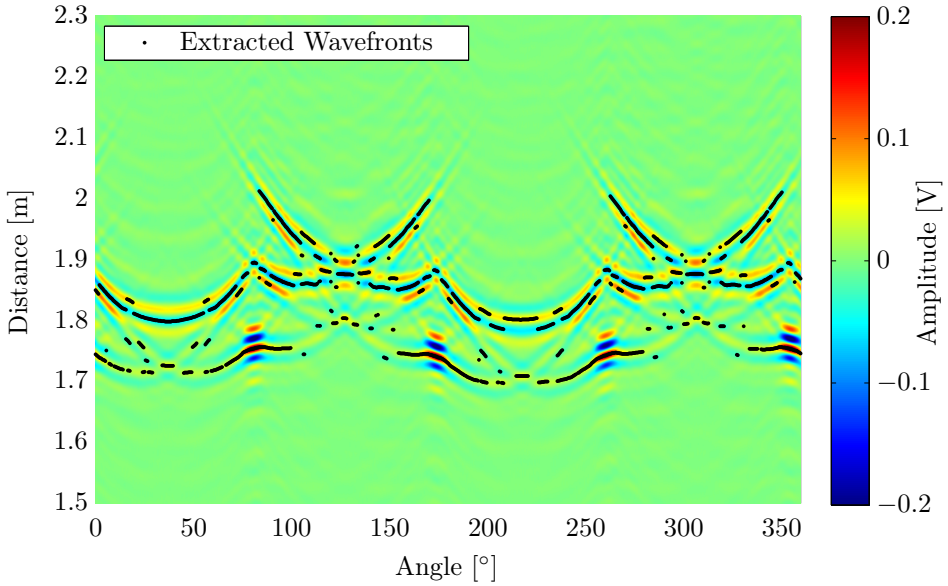

Figure 4.14: Extracted wavefronts by the classical correlation method for object o11

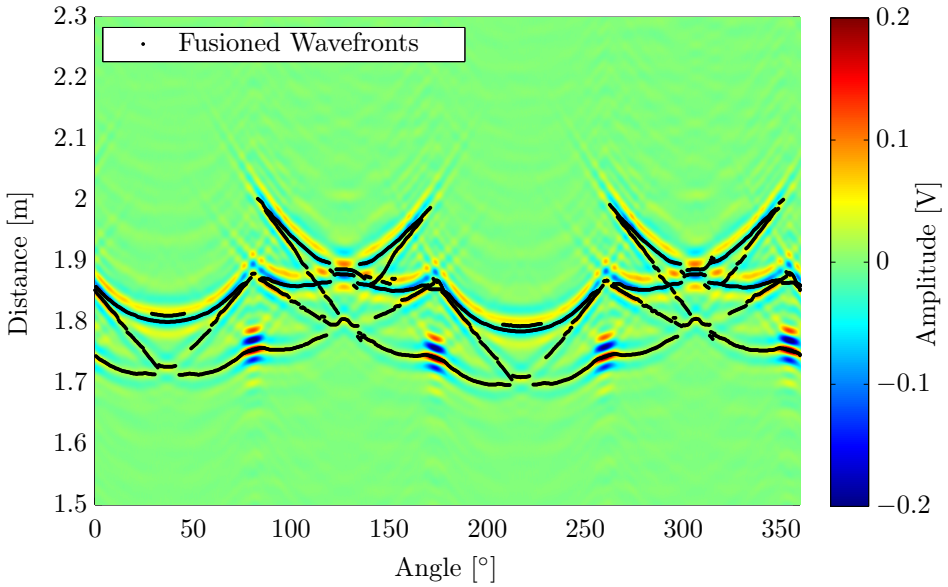

Figure 4.15: Optimised and fusioned wavefronts for object o11

4.5 Evaluation

With regard to the objective of super-resolution OR an evaluation of the wavefront extraction algorithms shall be provided which coincides with the requirements of the used OR. The OR processes the extracted features of the objects, i.e. significant scattering centres which are the edges and corners of the objects. The features in turn are computed from the wavefronts with a super-resolution feature extraction algorithm introduced in the next chapter. Thus, a joint efficiency and performance evaluation of the various wavefront extraction algorithms shall be performed as a feature map whose feature extraction capability are directly depending on the accuracy of the processed wavefronts.

Therewith, a qualitative comparison of each algorithm shall be provided. In Figure 4.16, 4.17, 4.18 and 4.19 the extracted features of object o11 for the classical correlation method, the DCM, the PDCM and the PDCM with the

slow time optimisation, respectively, is provided. Note here, every improvement not only enhances the extraction accuracy of each feature but also the number of correct target points (which equals the number of wavefronts) is significantly higher. For the sake of an extended evaluation overview the corresponding results of object o5 are depicted in Figure 4.20, 4.21, 4.22 and 4.23.

In addition to a visual evaluation also a numerical accuracy evaluation of the wavefront extraction algorithms shall be provided. An artefact quantity [75]

$$\tilde{a}_n = \min_{\mathcal{T}_{\text{true}}} |\mathcal{T}_{\text{true}} - \mathcal{T}^n_{\text{estimated}}| \qquad \text{with } n = 1, \ldots, N \tag{4.15}$$

is defined where N is the total number of target points which equals the number of extracted wavefronts. $\mathcal{T}_{\text{true}}$ and $\mathcal{T}_{\text{estimated}}$ are the sets of true scattering centres (i.e. the a priori known coordinates of the edges and the corners) and the estimated target points, respectively. The cumulative distribution function $F_{\tilde{a}}(\tilde{a})$ of the artefact quantity for the same objects of the visual evaluation o11 and o5 are plotted in Figure 4.24 and 4.25, respectively. An iso-artefact level of $\tilde{a} = 0.4\lambda_{\text{c}} \approx 0.0133$ m where λ_{c} equals the wavelength of the centre frequency of 9 GHz is marked.
It can be seen that in the case of the object o11 the PDCM with the slow time optimisation exhibits 99% of all target points with less than a translative error of $\tilde{a} = 0.4\lambda_{\text{c}}$ whereas this value degenerates for the PDCM to 94%, for the classical correlation to 83% and for the DCM to 77%.
In the case of the object o5 the PDCM with the slow time optimisation the percentage of the target points which exhibit a translative error less than $\tilde{a} = 0.4\lambda_{\text{c}}$ is 98%, for the PDCM 96%, for the DCM 91% and for the classical correlation 87%.

To conclude, the PDCM with slow time optimisation represents a novel wavefront extraction algorithm with super-resolution capability which is by far

superior than the state of the art algorithms found in the literature. It not only extracts wavefronts which exhibit an enhanced precision under severe interference influence but also the amount of wavefronts and consequently the amount of target points are higher. Until now, polarimetric techniques and a robust optimisation which exhibits the slow time signal 'history' was not considered. The resulting wavefronts are the input data for the feature extraction algorithm introduced in the next chapter.

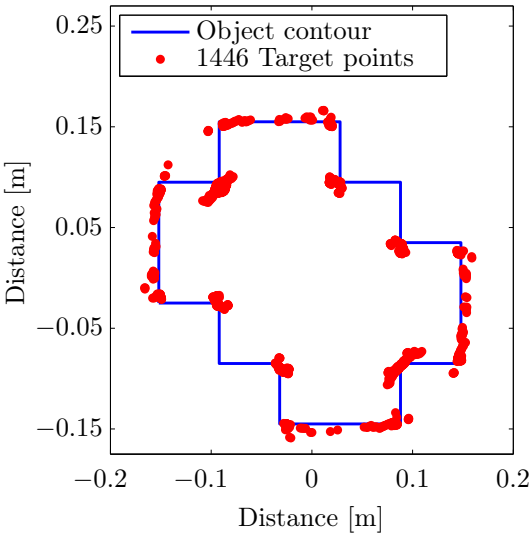

Figure 4.16: Classical correlation

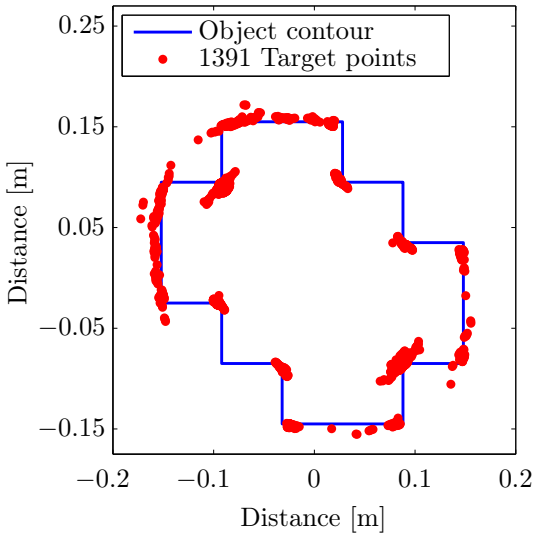

Figure 4.17: DCM

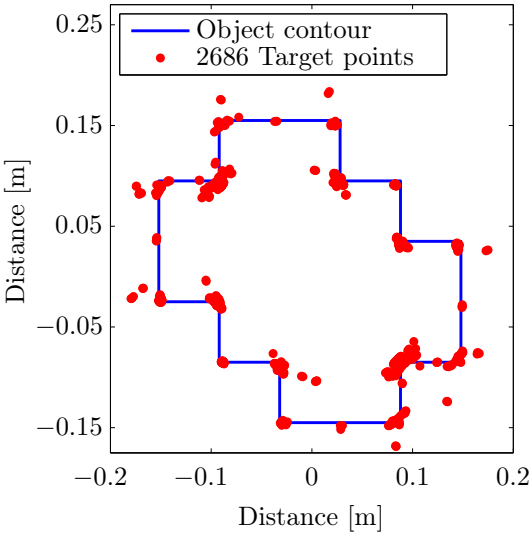

Figure 4.18: PDCM

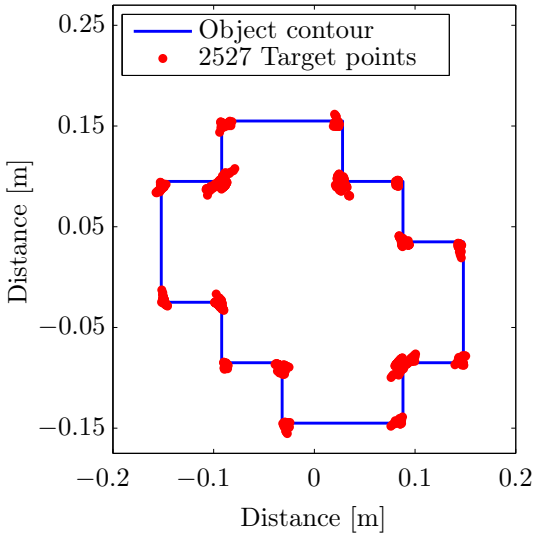

Figure 4.19: PDCM with slow time optimisation

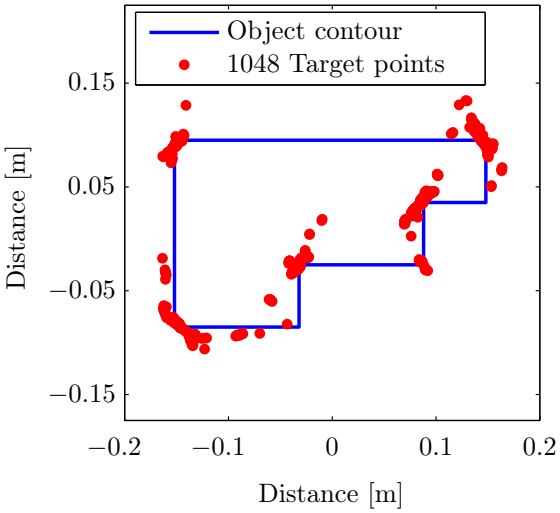

Figure 4.20: Classical correlation

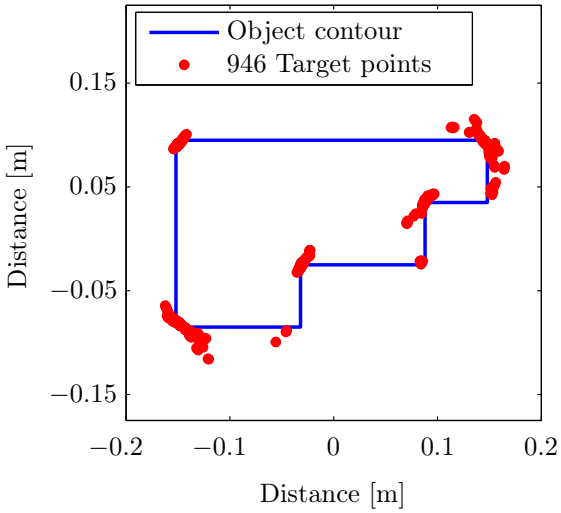

Figure 4.21: DCM

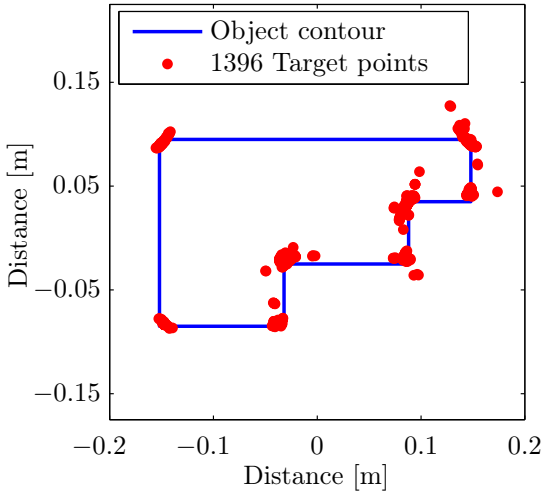

Figure 4.22: PDCM

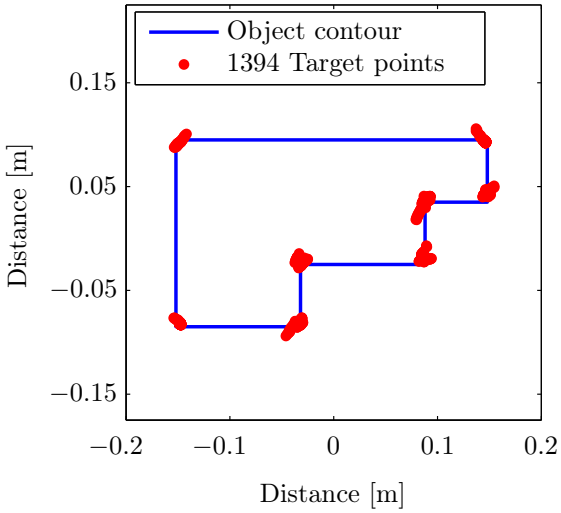

Figure 4.23: PDCM with slow time optimisation

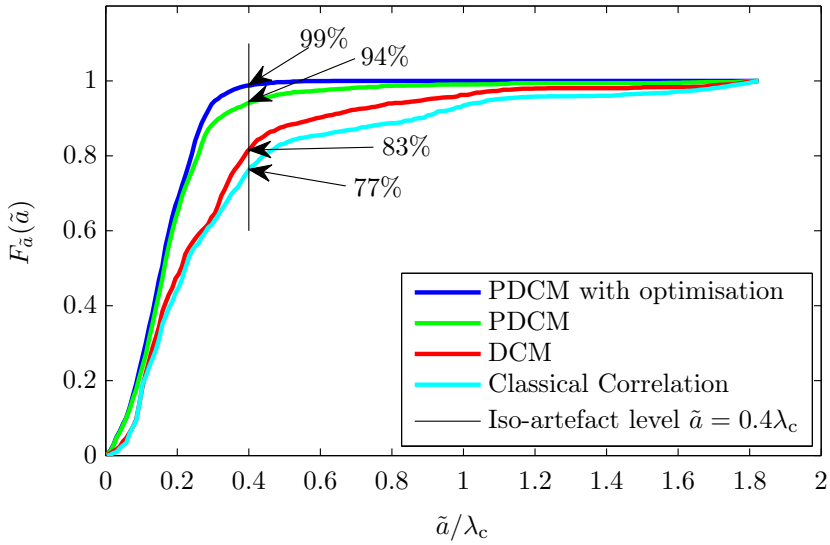

Figure 4.24: Cumulative distribution function of the artefact quantity $\tilde{a}$ for object o11

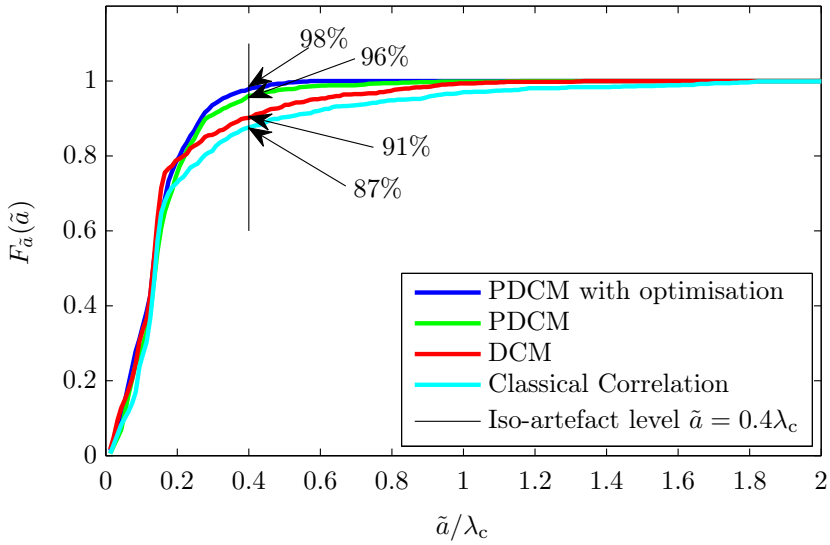

Figure 4.25: Cumulative distribution function of the artefact quantity $\tilde{a}$ for object o5

FIFTH CHAPTER

Feature Extraction and Imaging

All imaging or feature extraction algorithms that are based on EM scattering perform a kind of back projection for image reconstruction. In chapter 1.2 a review about Radar imaging and feature extraction algorithms with focus and relevance on the thesis goals has already been provided. Two grand strategies are apparent, namely

- migration based imaging,
- wavefront based imaging and feature extraction,

respectively. In principle, both methods have much in common and basically the wavefront based methods are akin to migration based ones; while the migration based algorithms process the *whole* temporal evolution of the Radar data in a summation sense to compose a focusing, the wavefront based algorithms just exploit a *unique* time sample which coincides with the wavefront. Evidently, the type of resulting Radar images becomes obvious:
The migration based algorithms compute a matrix output where all coordinates are assigned with amplitudes, whether they belong to the target or not. In contrast, the wavefront based algorithm calculates single coordinates which coincide with the scattering centres of the target. In the ideal case, the migrated image exhibits a high peak in the area of the scatterer while the remaining part of the image is of low energy and the wavefront based algorithm exhibits negligible translative errors between the true target points and the estimated ones. Obviously, a migrated image always needs some kind of post-processing to extract the true und unambiguous coordinates of the

target (contour), whereas the wavefront based algorithms directly compute the coordinates ready to process from a subsequent system.
Since a migrated image is as well processed in the final OR system the basics of the migration based imaging shall be introduced in a subsequent section. Firstly, a novel feature extraction algorithm shall be introduced in the following.

For the sake of a highly performing OR system the objects are abstracted to their significant scattering centres, namely edges and corners.
The scattering signature of a flat surface is restricted most. According to Snell's law the scattered angle equals the angle of incident which requires a perfect alignment of the antennas. Hence, a serious handicap can result when sharp focusing directive antennas are used and nearby flat surfaces are simply not recognisable because they reradiate all the energy away from the Rx.
Thus, both edges and corners are suitable as features as they are 'visible' from a wide range of orientation from an EM scattering point of view. In the last chapter a super-resolution capable algorithm to extract the wavefronts provoked of these features has been introduced. In this chapter, the super-resolution capable processing of those wavefronts shall be discussed to map the wavefronts into coordinates.

5.1 Super-Resolution capable Feature Extraction

For the sake of clarity and simplicity, the discussion starts with a simple bi-static configuration according to the illustration provided in Figure 5.1. Under the assumption of a 2 dimensional Euclidean space with the unit normal vectors $\vec{\mathbf{e}}_x$ and $\vec{\mathbf{e}}_y$ the omni-directional Tx and Rx are unambigiously defined with the position vectors $\vec{\mathbf{Tx}}$ and $\vec{\mathbf{Rx}}$. A single MUT provides the

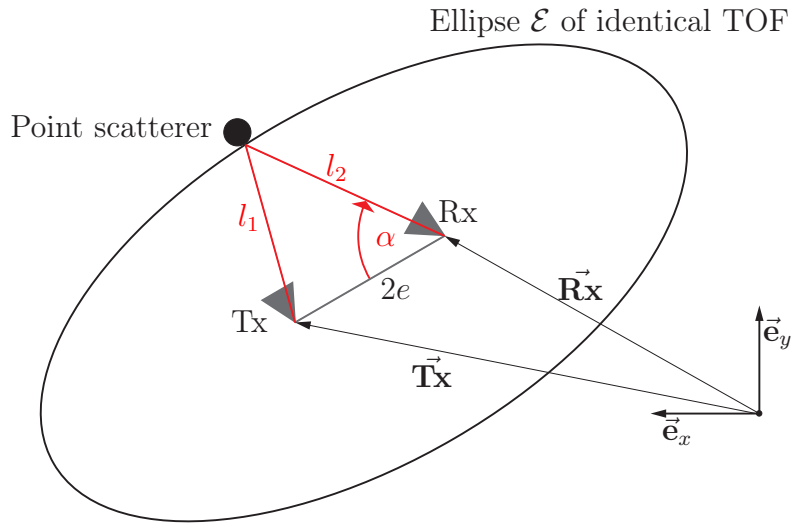

Figure 5.1: Illustration of a scattering process at a point scatterer observed by a bi-static antenna configuration.

TOF $(l_1+l_2)/c_0$ or the travelling path l_1+l_2, respectively, where l_1 equals the path from the Tx to the scatterer and l_2 equals the path from the scatterer to the Rx. Due to the lack of a priori information the exact coordinates of the point scatterer are not known and the only information gathered by a Radar system is the *precise* TOF due to the wide occupied frequency band. Thus, in the case of a bi-static antenna configuration the point scatterer may be located anywhere on an ellipse of identical TOF (circle of identical TOF in a mono-static configuration). The focal points of the ellipse coincide with the Tx and Rx and in accordance to the mathematical habitus the distance between both focal points, the antenna axis, shall equal $2e$ with e the half offset between both antennas. Hence, the ellipse may be defined unambigiously as

$$\mathcal{E}(x,y) = \frac{x^2}{a^2} + \frac{y^2}{b^2} - 1 = 0 \tag{5.1}$$

with the major axis $a = (l_1 + l_2)/2$ and the minor axis $b = \sqrt{a^2 - e^2}$. In the particular case of directive antennas, the ellipse may be trivially restricted to an arc since the boresight of an antenna is of finite extension. However, even in that case the challenge is to estimate the angle α between l_2 and the antenna axis to subsequently provide the localisation of the point scatterer as the ultimate objective of the feature extraction algorithm.

Apparently, a set of measurements is a prerequisite to solve the ambiguity. Thus, a larger aperture is synthesised by an antenna motion with a single measurement on every sample of the track. The following discussion is in accordance to Figure 5.2. Again, a two dimensional Euclidean space with the unit normal vectors $\vec{\mathbf{e}}_x$ and $\vec{\mathbf{e}}_y$ shall be assumed. As an example the object o11 is sensed by the MUT with the same bi-static configuration of the previous discussion. The location of the $\mathrm{Tx}_{\mathrm{MUT}}$ and $\mathrm{Rx}_{\mathrm{MUT}}$ are unambigiously determined by the position vectors $\vec{\mathbf{Tx}}_{\mathrm{MUT}}$ and $\vec{\mathbf{Rx}}_{\mathrm{MUT}}$, respectively. For the sake of clarity and simplicity, let the MUT exhibit solely a single wavefront which determines unambigiously the ellipse $\mathcal{E}_{\mathrm{MUT}}$ or an arc as a part of the ellipse in the case of directive antennas.

Additionally, the n-th neighbouring measurement $m_n(t)$ with $n = 1, \ldots, N$ and $N = 2$ in this particular case is performed. In the n-th measurement position $i = 1, \ldots, I$ wavefronts are detected. Thus, the i-th ellipse created at the n-th measurement point is denoted as $\mathcal{E}_n^i$ which intersects with $\mathcal{E}_{\mathrm{MUT}}$ in the location determined by the position vector $\vec{\mathbf{P}}_n^i$. The determination of intersection points of two arbitrary ellipses is well documented in the mathematical literature. Within this thesis the algorithm in [29] is used. Thus, the outward and backward travelling distances between the antennas of the MUT and the corresponding intersection points can be computed unambigiously

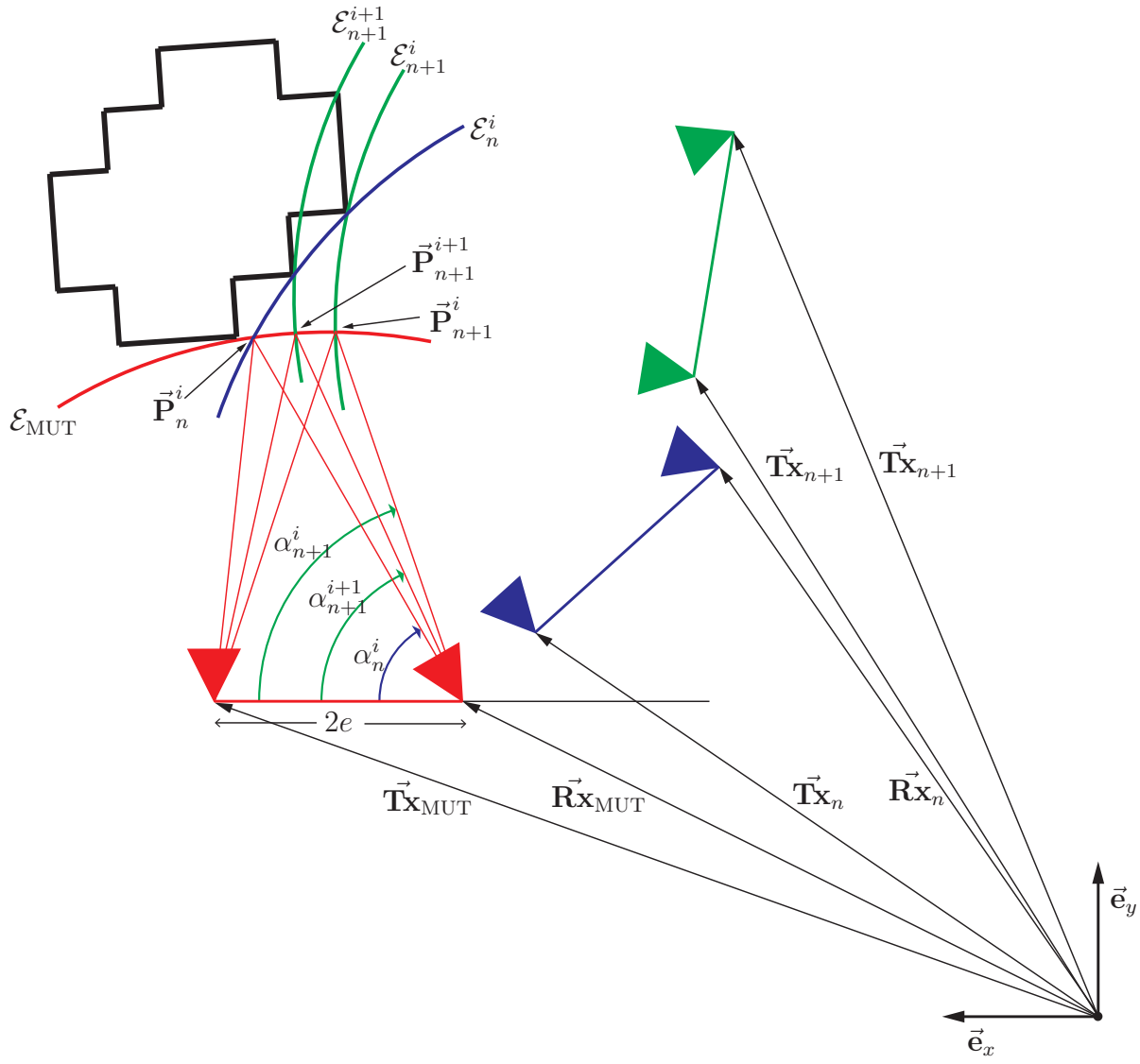

Figure 5.2: Illustration of the measurement setup with relevant quantities. *Not true to scale*

as

$$l_{1,n}^{i} = \left| \vec{\mathbf{Tx}}_{\mathrm{MUT}} - \vec{\mathbf{P}}_{n}^{i} \right| \qquad \text{with } i = 1, \ldots, I; n = 1, \ldots, N \tag{5.2}$$

$$l_{2,n}^{i} = \left| \vec{\mathbf{Rx}}_{\mathrm{MUT}} - \vec{\mathbf{P}}_{n}^{i} \right| \qquad \text{with } i = 1, \ldots, I; n = 1, \ldots, N \tag{5.3}$$

where $l_{1,n}^{i}$ is the distance between $\mathrm{Tx}_{\mathrm{MUT}}$ and the intersection point determined by $\mathcal{E}_{\mathrm{MUT}}$ and $\mathcal{E}_{n}^{i}$. Analogously, $l_{2,n}^{i}$ is the distance between $\mathrm{Rx}_{\mathrm{MUT}}$ and the intersection point determined by $\mathcal{E}_{\mathrm{MUT}}$ and $\mathcal{E}_{n}^{i}$.

By means of the 'Law of Cosines' [65] an unambigious angle between the antenna axis of the MUT and the intersection point $\vec{\mathbf{P}}_{n}^{i}$ can be computed as

$$\alpha_{n}^{i} = \arccos\left(\frac{\left(l_{2,n}^{i}\right)^{2} + (2e)^{2} - \left(l_{1,n}^{i}\right)^{2}}{2\, l_{2,n}^{i}\, (2e)} \right) \tag{5.4}$$

$$\text{with } i = 1, \ldots, I; n = 1, \ldots, N$$

Hence, α_{n}^{i} is a function defined uniquely with the Rx position of the MUT $\vec{\mathbf{Rx}}_{\mathrm{MUT}}$ and the intersection points $\vec{\mathbf{P}}_{n}^{i}$. So far, a set of angles α_{n}^{i} induced by neighbouring measurement locations is obtained. An explicit target point can be determined by computing an unique optimal angle $\alpha_{\mathrm{opt}}\left(\vec{\mathbf{Rx}}_{\mathrm{MUT}}\right)$ which assigns every $\mathrm{Rx}_{\mathrm{MUT}}$ an angle towards the scattering centre.

By exploiting the previously discussed spatially wide reradiating signature of the features a so-called convergence evaluation function [74] depending on the angular variable ξ for the i-th ellipse of the n-th measurement point can be performed as

$$q_{n}^{i}\left(\xi, \vec{\mathbf{Rx}}_{\mathrm{MUT}}, \vec{\mathbf{P}}_{n}^{i}\right) = \exp\left(-\frac{\left(\xi - \alpha_{n}^{i}\left(\vec{\mathbf{Rx}}_{\mathrm{MUT}}, \vec{\mathbf{P}}_{n}^{i}\right)\right)^{2}}{2\sigma_{\alpha}^{2}} \right) \tag{5.5}$$

$$\text{with } i = 1, \ldots, I; n = 1, \ldots, N$$

where the quantity σ_α is a hardware dependent constant. Obviously, with equation (5.5) the set of angles α_n^i are represented as Gaussian functions with the standard deviation σ_α. The Gaussian shape of the evaluation functions $q_n^i\left(\xi, \vec{\mathbf{Rx}}_{\mathrm{MUT}}, \vec{\mathbf{P}}_n^i\right)$ are directly influenced by the standard deviation. As a crucial quantity the focusing capability of the algorithm strongly depends on the quantification of the standard deviation. However, a numerical determination will be discussed in the subsequent evaluation section.

In order to obtain a single quantity for the prospected α_{opt} the superposition of the weighted evaluation functions is carried out which yields [74]

$$Q\left(\xi, \vec{\mathbf{Rx}}_{\mathrm{MUT}}\right) = \left| \sum_{n=1}^{N} \sum_{i=1}^{I} m_n\left(\left(l_{1,n}^i + l_{2,n}^i\right)/c_0\right) q_n^i\left(\xi, \vec{\mathbf{Rx}}_{\mathrm{MUT}}, \vec{\mathbf{P}}_n^i\right) \right|. \tag{5.6}$$

Here, the weight $m_n\left(\left(l_{1,n}^i + l_{2,n}^i\right)/c_0\right)$ consists of the signal amplitude of the MUT in the time sample when the wavefront is extracted or the EM wave hits the object, respectively. An optimal α_{opt} can be estimated by evaluating equation (5.6) for the maximum:

$$\alpha_{\mathrm{opt}}\left(\vec{\mathbf{Rx}}_{\mathrm{MUT}}\right) = \arg\max_{\xi}\left(Q\left(\xi, \vec{\mathbf{Rx}}_{\mathrm{MUT}}\right)\right). \tag{5.7}$$

Thus, a target point can be determined with the available information, namely the known antenna positions, the measured TOF and the resulting unique ellipse of identical TOF and the optimal angle towards the scattering centre obtained by equation (5.7). An illustration of the convergence evaluation function q as well as the superposition Q is provided in Figure 5.3 and 5.4.
The distance between the estimated target point and $\vec{\mathbf{Rx}}_{\mathrm{MUT}}$ can be calculated by means of the 'Law of Cosines' as

$$r_{\mathrm{MUT}} = \frac{(2e)^2 - \left(l_{1,\mathrm{MUT}} + l_{2,\mathrm{MUT}}\right)^2}{(2e) \cdot 2\cos\left(\alpha_{\mathrm{opt}}\right) - 2\left(l_{1,\mathrm{MUT}} + l_{2,\mathrm{MUT}}\right)}. \tag{5.8}$$

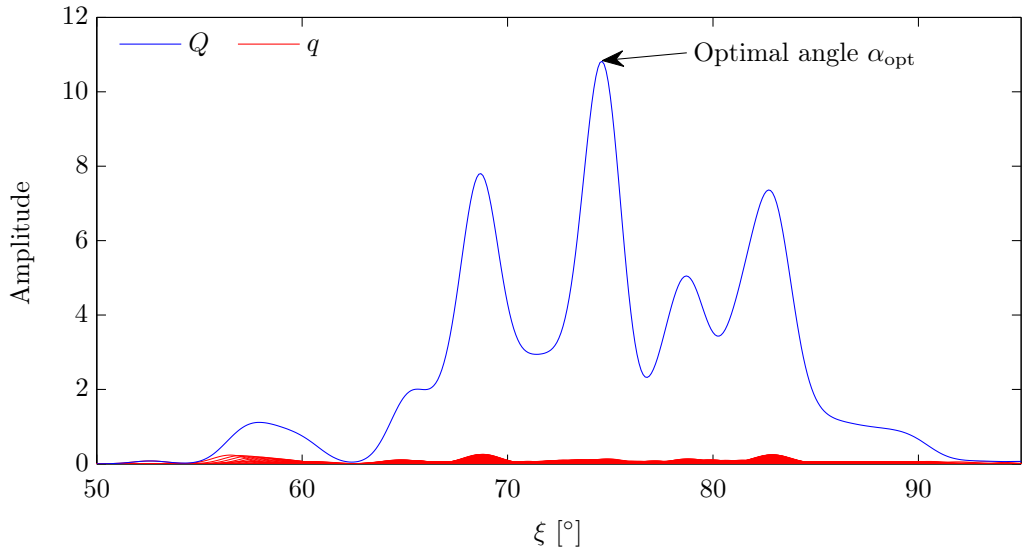

Figure 5.3: Set of convergence evaluation functions $q(\xi)$ and accumulation $Q(\xi)$ for an example MUT.

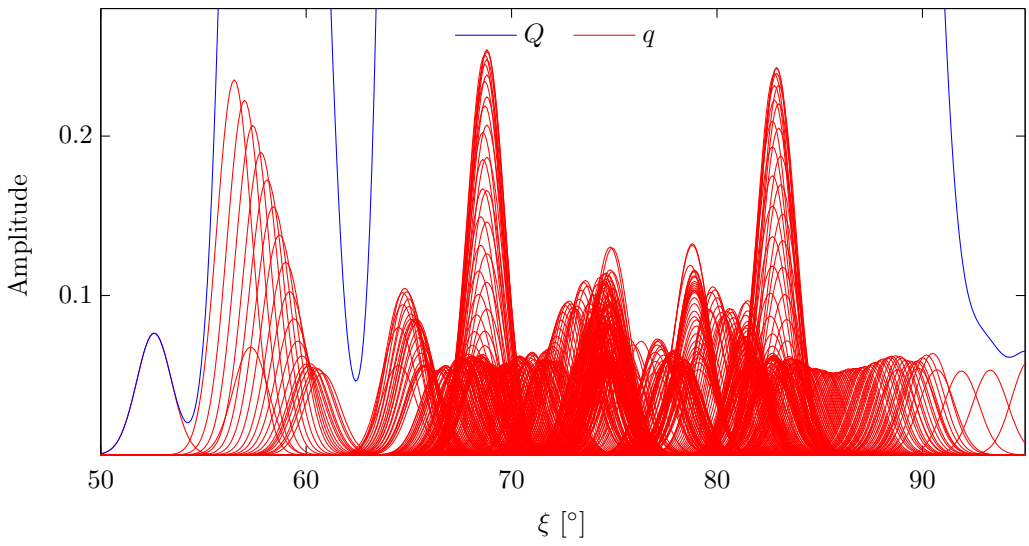

Figure 5.4: Zoom of set of convergence evaluation functions $q(\xi)$ and accumulation $Q(\xi)$ for an example MUT.

Finally, the ultimate target point of the scatterer can be expressed by combining the distance from equation (5.8) and the orientation from equation (5.7) as

$$\vec{\mathbf{P}}_{\mathrm{tp}} = \vec{\mathbf{Rx}}_{\mathrm{MUT}} + r_{\mathrm{MUT}} \cdot \exp\left(\mathrm{j}\left(\pi - \alpha_{\mathrm{opt}}\left(\vec{\mathbf{Rx}}_{\mathrm{MUT}}\right)\right)\right). \tag{5.9}$$

5.2 Numerical Evaluation

The focusing capability of the discussed algorithm and hence the performance are crucially depending on both parameters:

- The standard deviation σ_α from equation (5.5)
- The number of neighbouring measurement positions N.

The determination of both parameters shall be derived in the following for a fully compact feature extraction algorithm. The graphical result is shown in Figure 5.5.

The artefact quantity from equation (4.15) is again evaluated for object o11. However, to quantify the influence of both above mentioned parameters on the accuracy the cumulative distribution function of the artefact quantity $F_{\tilde{a}}(\tilde{a})$ is evaluated for an iso-artefact level of $\tilde{a} = 0.45\lambda_{\mathrm{c}} \approx 0.015$ m. This quantity is classified for the parameters under test in the range of $0.25\lambda_{\mathrm{c}} \leq \sigma_\alpha \leq 2.5\lambda_{\mathrm{c}}$ and $1 \leq N \leq 100$. The parameter N expresses the symmetric coverage of all neighbouring measurement points to the left as well as to the right of the MUT. The standard deviation is normalised with $\lambda_{\mathrm{c}} \approx 0.033$ m where λ_{c} equals the wavelength of the centre frequency.

Obviously, the best performance where the vast majority $F_{\tilde{a}}(\tilde{a} = 0.45\lambda_{\mathrm{c}})|_{0.25\lambda_{\mathrm{c}} \leq \sigma_\alpha \leq 2.5\lambda_{\mathrm{c}} \wedge 1 \leq N \leq 100} \geq 90\%$ of target points exhibit a translative error less than $\tilde{a} = 0.45\lambda_{\mathrm{c}}$ is for $80 \leq N \leq 100$ and $\sigma_\alpha \leq 0.5\lambda_{\mathrm{c}}$. Moreover, the percentage values are still higher than 70% as long as N is more than 60 whereas this value rapidly drops below 40% for $\sigma_\alpha > 1.5\lambda_{\mathrm{c}}$.

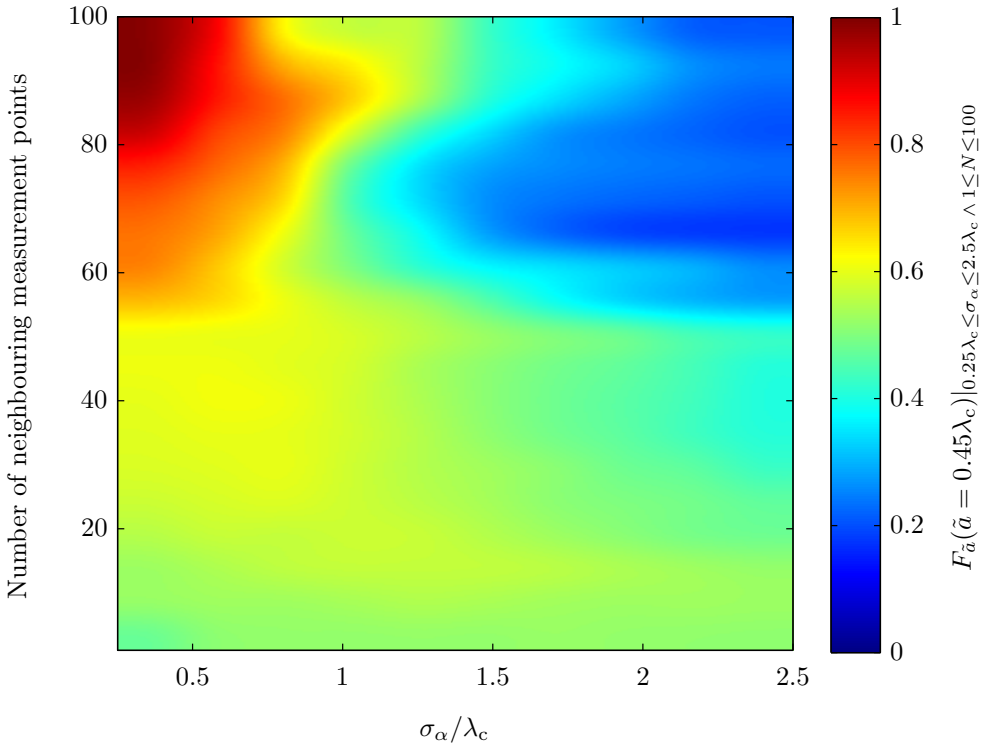

Figure 5.5: Accuracy evaluation in dependence of σ_α and N.

In summary, for super-resolution capable mapping of the wavefronts into unique highly precise coordinates (i) the number of neighbouring measurement points has to be large whereas (ii) the standard deviation of the convergence evaluation function from equation (5.5) has to minimise. Note here, that a too small standard deviation is not recommended since narrow evaluation functions handicap the accumulation operation.

Actually, these evaluation results are plausible and also conform with the literature.
A small standard deviation ensures the Gaussian function in equation (5.5) to be 'sharp' whilst a larger standard deviation blurs the coverage and dis-

torts the accuracy.
Furthermore, it is well known that the down-range resolution is inverse proportional to the hardware given bandwidth. Two scatterers aligned in the boresight of the Radar are the more precise separable as the pulses are the more narrow resulting in less interference. But it is not too well known that the cross-range resolution which expresses the capability to separate 2 scatterers perpendicular aligned to the boresight is differently quantified. "While range resolution depends on the bandwidth, cross range resolution is mainly dependent on the ratio between aperture and wavelength. In UWB systems resolution is estimated with an average wavelength." [52]
To be more specific, the cross-range resolution is inverse proportional to the aperture, i.e. the larger the aperture is, the more capable is the Radar system to separate nearby scatterers perpendicular to the boresight. This is e.g. the reason why narrowband air-borne and space-borne Radars provide high-resoluted images of landscape but do not obtain precise depth information.

However, by increasing the quantity N the synthetic aperture of the system is increased and the more capable is the system to apply focusing. This well-known specification of the narrowband Radar community is herewith quantified for the field of short-range UWB Radar.

The feature extraction algorithm dicussed so far is applied on the reference measurements as well as on the validation measurements to carry out the OR. A second pattern is obtained from the same measurements in the form of a migrated image. In the following, the specifications of the therewith obtained references are discussed.

5.3 Wavefront based Reference Alphabet

The first set of the reference alphabet consists of the feature extraction algorithm results shown in Figure 5.6. Within the reference measurements the

objects are not subject to a translative or a rotational offset. The wavefronts are extracted by the PDCM with slow time optimisation and the parameters of the feature extraction algorithm are set to $N = 100$ and $\sigma_\alpha = 0.25\lambda_c$. For the sake of clarity colorbars are avoided and therefore the target points are subject to a grayscale coding. White assigns minimal values whereas black assigns maximum amplitudes. The amplitudes equal the absolute value of the peak amplitudes in the corresponding scattering momentum expressed as $|m_{\mathrm{MUT}}\left(\left(l_{1,\mathrm{MUT}} + l_{2,\mathrm{MUT}}\right)/c_0\right)|$.
However, in the OR algorithm the set of target points are not directly processed but they are subject to a clustering with a subsequent extraction of the gravity of mass of each cluster. The centres of gravity are marked in red.

5.4 Imaging based Reference Alphabet

A second set of the reference alphabet obtained by the Kirchhoff migration (KM) is provided from the same reference measurement that also serves for the first set. Thus, not an additional hardware effort but rather a different processing of the Radar data supplies diverse input data for the final OR system. The second reference set is shown in Figure 5.7.
In the following, the KM shall be introduced just briefly because the theory on migration based imaging is extensively analysed in the literature for over 3 decades mainly in the fields of geophysics, seismic exploration and radioastronomy. Moreover, the adaption to UWB has been established to a satisfying level from the beginning of the UWB activities [83] [173] [175]. Finally, the KM is a tool which supports the OR performance but is not the essential core and innovation of the thesis at hand.
Like all other EM imaging algorithms the KM assumes a priori known radiation velocity. Within these investigations this requirement is fulfilled since the measurements are carried out in ambient air with the velocity of light c_0. Let an area be scanned on a known track while measurements are taken successively. The strategy of the KM now is a back projection of the radiation

signature $m_{\mathrm{MUT}}(t)$ which is performed by a coherent summation.
More specifically, under the assumption of a bi-static configuration the radiation occurs with an elliptic shape. Hence, every time sample of the time-dependent MUT assigns an unique ellipse; the more delayed a sample is, the larger is the ellipse due to the longer covered distance. Afterwards, every ellipse 'floats' over the area to be imaged and assigns each pixel the amplitude of the corresponding time sample which is crossed by the spreading ellipse. Every time sample of each MUT is processed in the same way and the image is finally build up sequentially. Mathematically this can be formulated as

$$o(x,y) = \frac{1}{N}\sum_{n=1}^{N} m^n_{\mathrm{MUT}}\left(\frac{l^n_{1,\mathrm{MUT}}(x,y) + l^n_{2,\mathrm{MUT}}(x,y)}{c_0}\right) \tag{5.10}$$

where $o(x,y)$ is the pixel of the discretised image, $l^n_{1,\mathrm{MUT}}(x,y)$ is the distance between the Tx of the n-th MUT and $o(x,y)$, $l^n_{2,\mathrm{MUT}}(x,y)$ is the distance between $o(x,y)$ and the Rx of the n-th MUT. In the case that an object feature causes a scattering the peak points in the MUT arise and the ellipses superpose to hot spots of higher energy. Consequently, the image contrast is the higher the more measurements are performed. However, the summation also provokes artefacts because the ellipses or even the arcs, respectively, also intersect apart real scattering centres. The spatial resolution is decreased by this ambiguity of erroneous ellipse intersection points. Additionally, the noise level is increased just by the elippses themselves which degenerates the dynamic range.

The Reference Alphabet II and hence the images in Figure 5.7 consist of the KM applied onto the Pauli matrix decomposed Radar data for single bounce contribution. Double bounce is not considered here since objects o1 to o4 do not exhibit any double bounce scattering.

In chapter 7 it will be shown how these two alphabets are used to recognise the objects.

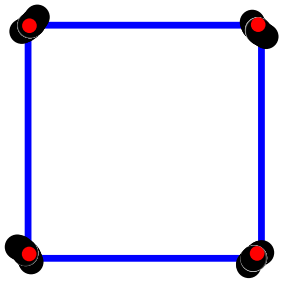

o1, 360 points

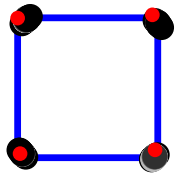

o2, 360 points

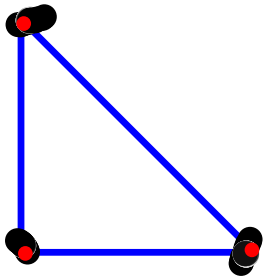

o3, 360 points

o4, 360 points

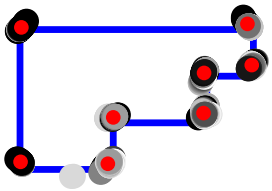

o5, 1342 points

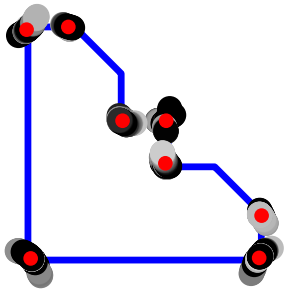

o6, 1197 points

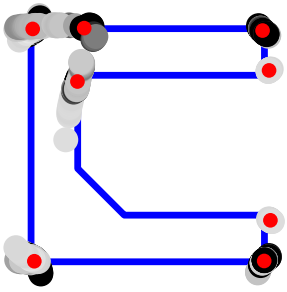

o7, 1064 points

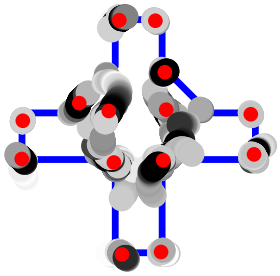

o8, 2100 points

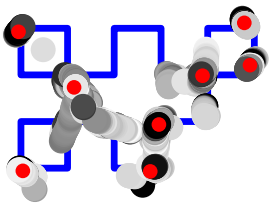

o9, 2348 points

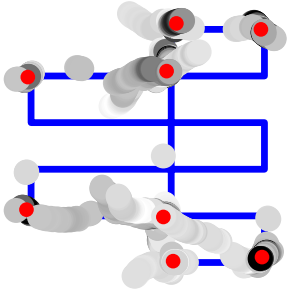

o10, 2227 points

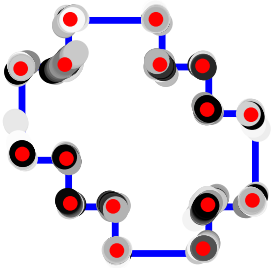

o11, 2588 points

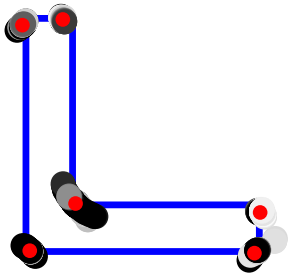

o12, 1250 points

Figure 5.6: Reference alphabet I

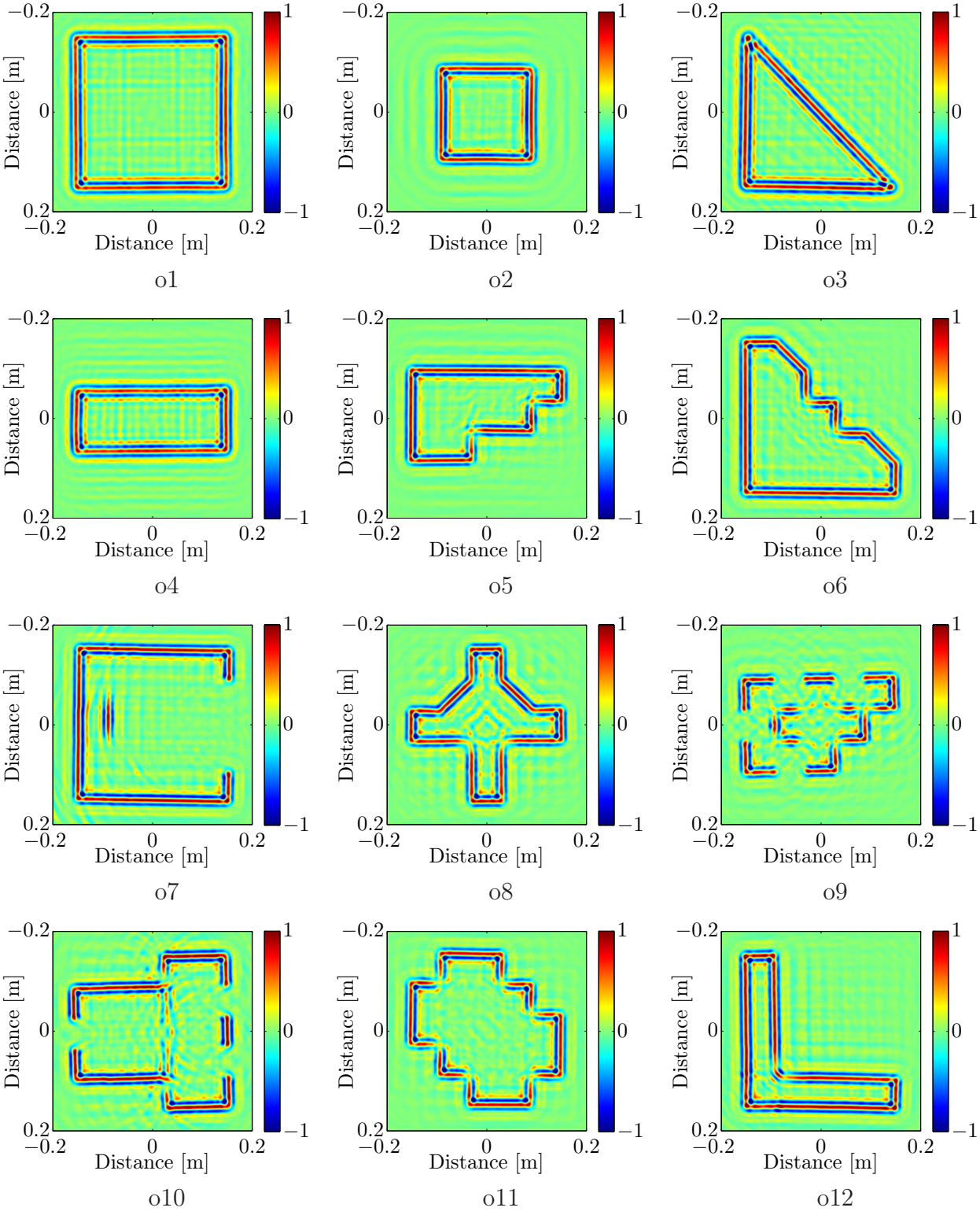

Figure 5.7: Reference alphabet II

SIXTH CHAPTER

Stereoscopic 3D Imaging

In recent years, several 3D UWB imaging algorithms have been published [70] [71] [72] [74] [92] [119] [147] [159]. All algorithms have in common that they utilise only a planar scanning surface. Hence, solely a limited perspective is used and the coverage of the lateral region of the object is rarely provided or would require extensive scan distances. As a matter of course, the back region and other shadowed areas are not imaged due to the lack of sensor illumination. To be entirely accurate, although the previously mentioned references claim to be 3D imaging they are actually not 3D or at least not stereoscopic 3D.

An S3D imaging algorithm provides all stereoscopically distributed scattering centres in a three dimensional Euclidean space. Thus, the planar aperture has to be substituted with an extended spatial aperture including the complete three dimensional Euclidean space. In [48] an imaging algorithm for biomedical diagnostics with a spatial scanning track is presented. However, the algorithm is based on inverse scattering algorithms and utilises a derivative operation onto the TOF. It is well known, that such algorithms exhibit weak performance with complex objects which cause multiple scattering effects. The resulting wavefronts are not continuous and a direct derivation is therefore not applicable.

In this chapter a mathematically exact S3D imaging of a bi-static UWB Radar system will be discussed that exhibits the required intersection point of 3 arbitrarily distributed and arbitrarily oriented ellipsoids. Actually, this

S3D algorithm is based on the 2D feature extraction algorithm discussed in chapter 5. The extension to a further dimension is basically straightforward except for the determination of the intersection point of 3 ellipsoids. In contrast to the well documented computation of the intersection point of 2 ellipses in the 2D imaging case, there is a lack on a numerical solution for the 3D case. Accordingly, this chapter focuses on the mathematical solution for the estimation of the intersection point of 3 ellipsoids. The incorporation of this solution into an imaging algorithm will be briefly discussed at the end of this chapter since it is very similar to the algorithm in chapter 5.

The innovative S3D method introduced here does actually not contribute to the OR algorithm. However, the scientific contribution to the field of UWB imaging is highly significant. Moreover, the exhibited novelty in the algorithm should be a fundamental basis for future research on 3D Radar imaging and entail more relevant research. On account of this, the S3D algorithm is covered on this occasion.

6.1 Intersection Point of Three Ellipsoids

Within the research for this thesis an award winning S3D algorithm has been published in [132]. In that publication the determination of a target point was simplified to a pair of two dimensional estimations. Thus, the elevation as well as the azimuth dimension was separately computed for the MUT. A crossed aperture both in horizontal and vertical direction with respect to the sensor location of the MUT was proposed and the 2D algorithm was carried out two times. However, an exact determination of stereoscopically distributed target points strictly requires an embracing aperture at different heights which also covers inclined neighbouring sensor positions. Hence, the spanned aperture of the novel algorithm is rather a mesh than two line apertures.

From a mathematical point of view, the set of identical TOFs of a bi-static antenna configuration shapes an ellipsoid in a three dimensional Euclidean space with the Tx and Rx at its foci. As an analogy to the 2D case it can be assumed that the scattering centre lies on the intersection point of the ellipsoid under test $\bar{\mathcal{E}}_1$ with a second and third neighbouring ellipsoid $\bar{\mathcal{E}}_2$ and $\bar{\mathcal{E}}_3$, respectively. For the further processing this intersection point has to be computed with a negligible deviation.
The three dimensional equation system

$$\begin{aligned} f_i(x,y,z) = &\frac{\left(x\cos\left(\alpha_i\right) + y\sin\left(\alpha_i\right) - x_i\right)^2}{a_i^2} \\ &+ \frac{\left(x\sin\left(\alpha_i\right) + y\cos\left(\alpha_i\right) - y_i\right)^2}{b_i^2} \\ &+ \frac{\left(z - z_i\right)^2}{c_i^2} - 1 = 0. \end{aligned} \tag{6.1}$$

describes the three ellipsoids $\bar{\mathcal{E}}_i$ with $i = 1, 2, 3$ where a_i, b_i and c_i denote the semi-axis lengths of the ellipsoid $\bar{\mathcal{E}}_i$. The coordinates of the ellipsoid centre are x_i, y_i, z_i and α_i is the rotation angle of ellipsoid in the xy-plane (azimuthal dimension).

Ellipsoids intersection particularly or quadric surface intersection in general is a demanding problem and continues to be an active topic of research in the field of geodesy and mathematics [53]. A. Norrdine who is an geodesy expert with particular expertise in the field of indoor positioning has contributed highly valuable to this issue [96] [97]. Since equation (6.1) is non linear and cannot be solved directly, a simple solution approach is to find a best estimate according to the Gauss-Newton (GN) method.

Let $P_{\mathrm{tp}} = (x, y, z)$ denote the spatial coordinates of the target point or the intersection point, respectively. The GN algorithm iteratively finds the min-

imum of the sum of squares formulated as

$$\hat{P}_{\mathrm{tp}} = \arg\min_{P_{\mathrm{tp}}} \sum_{i=1}^{3} f_i(P_{\mathrm{tp}}) \tag{6.2}$$

with $\hat{P}_{\mathrm{tp}}$ as the best estimate.

The solution procedure is to choose a start estimate, linearise the equations about that estimate, and solve iteratively the linearised equations in a least-squares sense. From a mathematical point of view, the algorithm starts with an initial guess $P_{\mathrm{tp},0}$. In order to find the minimum in equation (6.2) the method proceeds by the iterations [11] [95]

$$P_{\mathrm{tp},k+1} = P_{\mathrm{tp},k} - \left(\mathbf{J}_{\vec{\mathbf{f}}}^{\mathrm{T}}\mathbf{J}_{\vec{\mathbf{f}}}\right)^{-1}\mathbf{J}_{\vec{\mathbf{f}}}^{\mathrm{T}}\vec{\mathbf{f}}(P_{\mathrm{tp},k}) \tag{6.3}$$

where $\mathbf{J}_{\vec{\mathbf{f}}}$ is the Jacobian matrix of the vector $\vec{\mathbf{f}}(P_{\mathrm{tp},k}) = [f_1(P_{\mathrm{tp},k})\ f_2(P_{\mathrm{tp},k})\ f_3(P_{\mathrm{tp},k})]^{\mathrm{T}}$ at $P_{\mathrm{tp},k}$ and $(\cdot)^{-1}$ and $(\cdot)^{\mathrm{T}}$ are the inverse and transverse operator, respectively. The iteration process stops when the estimation error becomes negligibly small.

The application of the GN algorithm ensures to find the local minimum. However, this does not always coincide with the absolute minimum. Tests reveal that the GN-method could reliably solve equation (6.1) but only if the start estimate is 'close' to the solution. The determination of a reliable start is therefore a fundamental step.

A straightforward technique to find a reasonable start estimate would be to solve equation (6.1) analytically. However, in the literature closed formulas are restricted to two dimensional cases (intersection of ellipses) [29]. Another approach restricts itself to the existence of ellipsoid intersection; it is based on extending the problem to four dimensions and then determining the eigenvalues which yield a degenerate quadric surface [19]. Thus, a quantitative

solution with regard to the existence of an intersection point is given and not a qualitative solution with regard to the coordinates of the intersection point.

The proposal for an efficient start estimate investigated within this thesis is based on two steps:

1. Every ellipsoid in equation (6.1) has to be approximated with its equivalent sphere. An equivalent sphere has the same center as the ellipsoid and its radius is an average of the three ellipsoid axis lengths.

2. Determination of the intersection of the three equivalent spheres.

From a geometrical point of view the start estimate is determined by the intersection of three spheres (referred to as trilateration in geometry). In general the three spheres intersect in two points as possible solutions. The uniqueness can either be enforced by using a fourth sphere or an additional constraint. The constraint in the case of an UWB Radar system with directive antennas is that the intersection point is in front of the UWB Antennas.

In the literature different approaches exist for the coordinates calculation of the intersection point based on the trilateration principle. As an example, in [4] several methods are discussed and an algebraic method using the Groebner bases are presented. The approach in [157] is based on the calculation of the height of the tetrahedron, using its volume and the triangle plain, spanned by three sphere centers.

An alternative method for solving nonlinear problems on the example of trilateration is presented in [97] which will be used in the following. In contrast to the other methods, this method can easily be extended to the multilateration case and exhibits real-time capability. In the proposed method, the nonlinear elements of the equations system are treated as additional unknowns, which represent simultaneously a constraint. Thus a new equation system is

created, which is solved by means of linear algebra methods. The basic idea of the algorithm for the solution of intersection of three sphere is as following:

Given are the three reference points $P_1(x_1, y_1, z_1)$, $P_2(x_2, y_2, z_2)$ and $P_3(x_3, y_3, z_3)$ and the corresponding range measurements s_1, s_2 and s_3 to the intersection point N. The determination of the coordinates (x_N, y_N, z_N) of the point N is equivalent to finding the solutions of the quadratic equations

$$\begin{aligned}(x-x_1)^2+(y-y_1)^2+(z-z_1)^2&=s_1^2,\\(x-x_2)^2+(y-y_2)^2+(z-z_2)^2&=s_2^2,\\(x-x_3)^2+(y-y_3)^2+(z-z_3)^2&=s_3^2.\end{aligned} \tag{6.4}$$

Expanding and regrouping equation (6.4) yields

$$\begin{aligned}(x^2+y^2+z^2)-2x_1x-2y_1y-2z_1z&=s_1^2-x_1^2-y_1^2-z_1^2,\\(x^2+y^2+z^2)-2x_2x-2y_2y-2z_2z&=s_2^2-x_2^2-y_2^2-z_2^2,\\(x^2+y^2+z^2)-2x_3x-2y_3y-2z_3z&=s_3^2-x_3^2-y_3^2-z_3^2.\end{aligned} \tag{6.5}$$

Or in matrix representation:

$$\begin{bmatrix}1 & -2x_1 & -2y_1 & -2z_1\\ 1 & -2x_2 & -2y_2 & -2z_2\\ 1 & -2x_3 & -2y_3 & -2z_3\end{bmatrix}\begin{bmatrix}x^2+y^2+z^2\\ x\\ y\\ z\end{bmatrix}=\begin{bmatrix}s_1^2-x_1^2-y_1^2-z_1^2\\ s_2^2-x_2^2-y_2^2-z_2^2\\ s_3^2-x_3^2-y_3^2-z_3^2\end{bmatrix}. \tag{6.6}$$

Thus, equation (6.6) is represented in the form

$$\mathbf{A}_0\,\vec{\mathbf{x}}=\vec{\mathbf{b}}_0 \tag{6.7}$$

with the constraint

$$\vec{\mathbf{x}}\in E \text{ where } E=\left\{(x_0,\,x_1,\,x_2,\,x_3)^{\mathrm{T}}\in\mathbb{R}^4 | x_0=x_1^2+x_2^2+x_3^2\right\}. \tag{6.8}$$

Note that the span of the columns of $\mathbf{A}_0$ does depend only on the choice of the reference points. In the usual case, where the points P_1, P_2 and P_3 do

not lie on a straight line, it applies that $\text{rank}(\mathbf{A}_0) = 3$ and $\dim(\ker(\mathbf{A}_0)) = 1$. The $\text{rank}(\mathbf{A}_0)$ is the subset of $\mathbb{R}^3$ comprised of all vectors in $\mathbb{R}^4$.

The general solution of equation (6.7) can be expressed as

$$\vec{\mathbf{x}} = \vec{\mathbf{x}}_\text{p} + t \cdot \vec{\mathbf{x}}_\text{h}, \tag{6.9}$$

Where $\vec{\mathbf{x}}_\text{p}$ is the particular solution, $\vec{\mathbf{x}}_\text{h}$ is the solution of the homogeneous system $\mathbf{A}_0 \vec{\mathbf{x}} = 0$ ($\vec{\mathbf{x}}_\text{h}$ is a Basis of $\ker(\mathbf{A}_0)$) and t is a real parameter. The vectors $\vec{\mathbf{x}}_\text{p}$ and $\vec{\mathbf{x}}_\text{h}$ can be computed using the Gaussian elimination method. The particular solution $\vec{\mathbf{x}}_\text{p}$ could be alternatively determined using the pseudo inverse of the matrix $\mathbf{A}_0$.

The determination of the parameter t shall be discussed in the following: Let $\vec{\mathbf{x}}_\text{p} = [x_{\text{p}0}\ x_{\text{p}1}\ x_{\text{p}2}\ x_{\text{p}3}]^\text{T}$, $\vec{\mathbf{x}}_\text{h} = [x_{\text{h}0}\ x_{\text{h}1}\ x_{\text{h}2}\ x_{\text{h}3}]^\text{T}$ and $\vec{\mathbf{x}} = [x_0\ x_1\ x_2\ x_3]^\text{T}$. By substituting $\vec{\mathbf{x}}_\text{p}$, $\vec{\mathbf{x}}_\text{h}$ and $\vec{\mathbf{x}}$ in equation (6.9) it yields

$$\begin{aligned} x_0 &= x_{\text{p}0} + t \cdot x_{\text{h}0}, \\ x_1 &= x_{\text{p}1} + t \cdot x_{\text{h}1}, \\ x_2 &= x_{\text{p}2} + t \cdot x_{\text{h}2}, \\ x_3 &= x_{\text{p}3} + t \cdot x_{\text{h}3}. \end{aligned} \tag{6.10}$$

By applying the constraint in equation (6.8) it yields

$$x_{\text{p}0} + t \cdot x_{\text{h}0} = (x_{\text{p}1} + t \cdot x_{\text{h}1})^2 + (x_{\text{p}2} + t \cdot x_{\text{h}2})^2 + (x_{\text{p}3} + t \cdot x_{\text{h}3})^2 \tag{6.11}$$

and thus

$$\begin{aligned} \left(x_{\text{h}1}^2 + x_{\text{h}2}^2 + x_{\text{h}3}^2\right)\, t^2 + 2 \left(x_{\text{p}1}x_{\text{h}1} + x_{\text{p}2}x_{\text{h}2} + x_{\text{p}3}x_{\text{h}3} - \frac{1}{2}x_{\text{h}0} \right) t \\ + x_{\text{p}1}^2 + x_{\text{p}2}^2 + x_{\text{p}3}^2 - x_{\text{p}0} = 0. \end{aligned} \tag{6.12}$$

Equation (6.12) describes a quadratic equation in the form $at^2 + bt + c = 0$ with the solution

$$t_{1/2} = \frac{-b \pm \sqrt{b^2 - 4ac}}{2a}. \tag{6.13}$$

Finally, the solution of the equation (6.7) reveals

$$\begin{aligned}\vec{\mathbf{x}}_1 &= \vec{\mathbf{x}}_\mathrm{p} + t_1 \cdot \vec{\mathbf{x}}_\mathrm{h},\\ \vec{\mathbf{x}}_2 &= \vec{\mathbf{x}}_\mathrm{p} + t_2 \cdot \vec{\mathbf{x}}_\mathrm{h}.\end{aligned} \tag{6.14}$$

Both solutions of equation (6.14) express the coordinates of the initial point N which equals the sphere intersection. Due to the directivity of the antennas the solution behind the antennas is discarded. By reason of the definition in equation (6.8) the last 3 coordinates x_1, x_2, x_3 of the solution $\vec{\mathbf{x}}$ are the actual coordinates which are used in equation (6.3) as the start estimation for the actual iterative ellipsoid intersection algorithm.

If the trilateration problem cannot be solved because e.g. the measured distances are too short, there are no real valued solutions. In this case, the real part is used as an start estimate. However, with this estimate, the constraint in equation (6.8) is not met anymore. Thus the difference $d = x_0 - (x_1^2 + x_2^2 + x_3^2)$ is a measure of the solvability of the trilateration problem.

6.2 S3D Image Evaluation

With the ellipsoid intersection algorithm in the previous section the 2D feature extraction algorithm discussed in chapter 5 can be extended by another dimension to obtain S3D images.

In equation (5.4) of the 2D algorithm a set of angles has been uniquely defined by $\mathbf{R}\vec{\mathbf{x}}_\mathrm{MUT}$ and the intersection points $\vec{\mathbf{P}}_n^i$ induced by neighbouring measurement locations.
The similar applies for the S3D case; every MUT for which a target point shall be estimated provides an ellipsoid intersection point with a pair of neighbouring sensor points of the aperture. This is iteratively performed for every pair of the aperture mesh spanned around the sensors of the MUT.

Hence, a set of intersection points in the three dimensional Euclidean space is provided. The position of each intersection point as well as the Rx position of the MUT are known which provides an azimuth and elevation angle and a distance between the Rx and the intersection point in spherical coordinates.

Analogously to the 2D case the set of azimuth and elevation angles are represented by the convergence evaluation functions in equation (5.5) separately. An unambigious azimuth and elevation angle is hence obtained by the superposition of the convergence evaluation functions as performed for the 2D case in equation (5.6). A maximum operator (equation (5.7)) finally yields the azimuth and elevation angles of the target point.

So far, the sensor positions of the MUT, the TOF and thus the resulting ellipsoid from equation (6.1) are known. Together with the previously estimated azimuth and elevation angle the only unknown parameter to determine an unique target point is the distance between the Rx and the surface of the ellipsoid. By means of simple optimisation methods this is highly accurately solvable [95] [11].

Experimental validations are shown in Figure 6.1 to Figure 6.6.
The antennas are fixed using horizontal alignment and move on a circular track at different heights. However, a hemispherical alignment of the antennas which covers more spatial degrees of freedom would immensely enhance the imaging results. Because of this and due to the lack of finer cross-resolution the fine structures in the middle of the target in Figure 6.5 and 6.6 are not completely resolved.

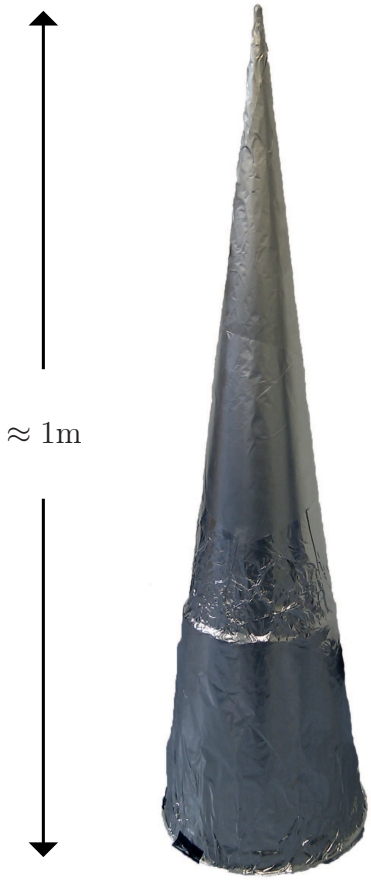

Figure 6.1: Photograph of the target

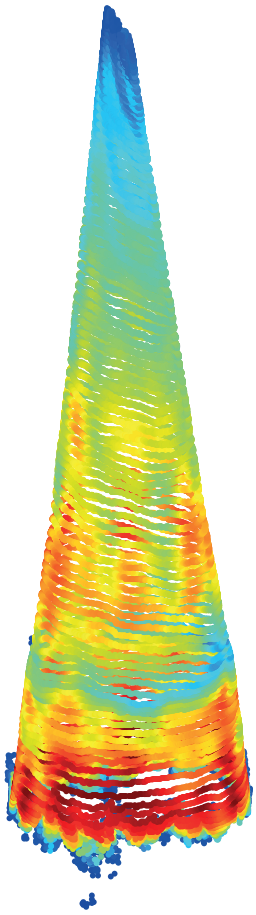

Figure 6.2: UWB Radar image of the target

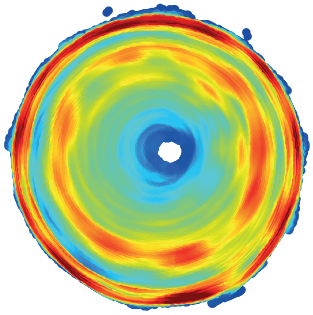

Figure 6.3: Top view of the UWB Radar image of the target

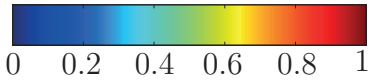

Color coded normalised amplitude

Figure 6.4: Photograph of the target

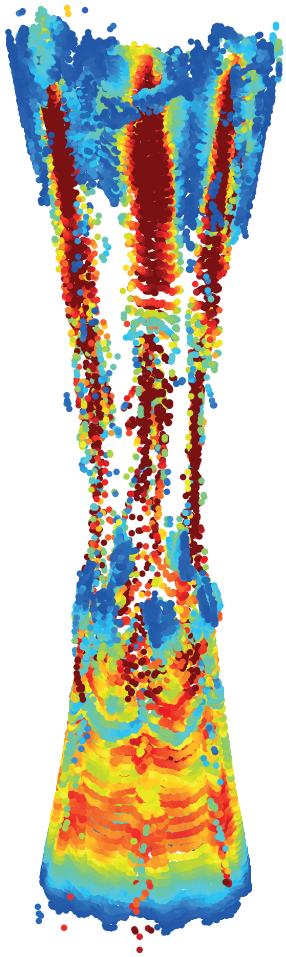

Figure 6.5: UWB Radar image of the target

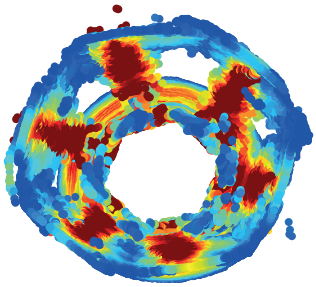

Figure 6.6: Top view of the UWB Radar image of the target

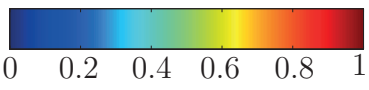

Color coded normalised amplitude

seventh Chapter

Object Recognition

The discussion in the chapter 1.2 shows that up to now an experimentally validated OR algorithm with complex structured objects in the field of UWB Radar is not investigated in the literature except the publications acquired within the research for the thesis at hand [124] [129] [131] [163]. Even theoretical considerations with simulated Radar data have not been published by other groups yet.

The vast majority of the investigations in the long history of the OR research is based on data gathered by optics or computationally generated patterns, i.e. data wich are visually well interpretable with cognitive abilities of humans. Thus, image processing algorithms have always been an essential part of OR systems for the sake of pre- and post-processing of the data. Although the fundamental physics behind both optical and UWB systems are similar, i.e. EM scattering, there are still fundamental differences between images obtained by optics and EM radiation based UWB images:

- Optical sensors are in most cases passive sensors. This means that an external source has to illuminate the area of interest with visible or non-visible (infrared) light while the optical Rx records the fraction of the light scattered towards it. Visible light occupies wavelengths from 380 nm (blue light) to 780 nm (red light). Thus, optical systems potentially resolve geometries from everyday life highly accurate. The final optical image is created by a single lens or an array of lenses wich are generally in the range of a couple of mm. Compared with the wavelength of visible light this is pretty large and finally determines the

ultra fine cross-resolution of optical images.
However, apart from special 3D cameras the sensor is not synchronised to the light source and consequentially the captured data is non-coherent. As a result, direct range information are not provided and estimations have to be performed by means of assisting systems, e.g. a stereo camera or a pair of eyes in the case of human beings.

- A Radar system based on EM scattering is an active system which works in a synchronous way and records the scattered waves coherently. Thus, by evaluating the travelling time of the waves a precise range information is provided at once which can be by far more precise than the estimations in the optics. A microwave image needs an aperture in any case, whether real or synthetic. The cross-resolution of the used UWB system is by far less than in the field of optics because the allocated wavelengths in this thesis occupy the range from 5 cm to 15 cm. A comparable cross resolution like in the optics would require an aperture of more than 600 m. Thus, short-range UWB Radar microwave images may be difficult to interpret with cognitive abilities of humans compared with optical images.

In this sense, approved methods and algorithms of the classical OR research could be adapted to the UWB OR to some extent while other parts (e.g. the OR evaluation of restricted tracks with an illumination beamwidth of non-ideal extension) required a complete rethinking and new strategies.
With regard to these circumstances, this chapter introduces the theory as well as experimentally validated results of a short-range super-resolution OR algorithm by means of UWB Radar.

7.1 Object Features

"To identify a target by a scalar RCS is like identifying people by their weight." [111]

This statement has been made by distinguished Radar engineers in 1989 at a time when UWB Radar of several GHz in the lower microwave region has not yet been considered, even not theoretically in the civil Radar research. However, the core objective of increased ambiguities in the field of UWB Radar data still remains the case today; due to the lack of precise direction information and due to the hardware given non-ideal beamwidth a radargram or a part of a radargram may be composed of by various similar objects. In this case an unique recognition with a very low ambiguity is not a trivial task.

The acquisition as well as the preparation of the received raw data needs sophisticated super-resolution algorithms as the previously introduced wavefront extraction algorithm in chapter 4 and the imaging and feature extraction algorithms in chapter 5. Thus, the MUTs are processed and provided in the same way as the reference feature map in Figure 5.6 and reference KM image in Figure 5.7.

From these representations a set of features has to be extracted from which conclusions may be drawn on the object under test (OUT) .
In order to exploit the full potential the features have to satisfy following demands:
For an efficient computation the feature extraction processing provides a reduction of the whole data volume to a subset which, in the ideal case, entirely contains the relevant information with regard to the application. Additionally, redundancy as well as non-relevant information shall be vanished as far as possible. The features have to provide a large discrepancy among each other which allows a characterisation and classification of the OUT on the highest possible level. The features shall be independent among each other, i.e. the covariance should converge to zero. Finally, these demands and requirements shall be preserved under translation and rotation of the OUT, i.e. the features shall provide invariances against linear transformation. In

this particular case, a scale invariance is not desired since object o1 and o2 shall be recognized as individual objects.

From both the feature map and the KM image the following features are extracted:

Moment based features

- Moment invariant $\vec{\vec{\mathbf{F}}}_{\mathrm{MI}}$

Geometrical features

- Eccentricity $\widetilde{F}_{\mathrm{EC}}$
- Fitting circle $\widetilde{F}_{\mathrm{FC}}$
- Form factor $\widetilde{F}_{\mathrm{FF}}$
- Inertia $\widetilde{F}_{\mathrm{IN}}$

Texture Features

- Fourier descriptors $\vec{\vec{\mathbf{F}}}_{\mathrm{FD}}$
- Curvature scale $\vec{\vec{\mathbf{F}}}_{\mathrm{CS}}$

In the following, the acquisition of the features shall be discussed in detail and vividly by means of the OUT o11 which is subject to a translative offset of $\delta_r = 0.162$ m and a rotational offset of $\delta_\alpha = 325°$. The obtained feature map and the KM image are shown in Figure 7.1 and 7.2, respectively.

7.1.1 Moment based Features

The theory of moment invariance for pattern recognition was first introduced by Hu in the early sixties [56] [57] and later discussed in more detail with regard to shape analysis by Reiss [110]. Hu adapted the classical algebraic theory of invariances of the previous century to the field of pattern recognition

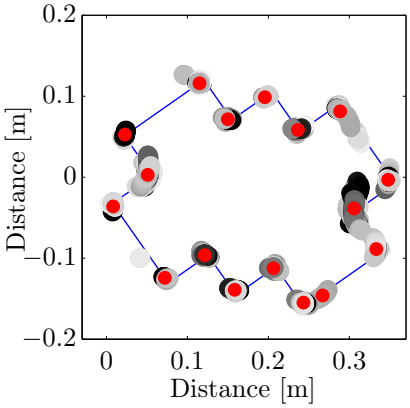

Figure 7.1: Feature Map of the OUT

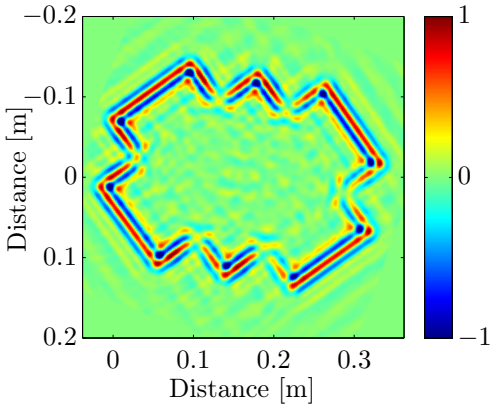

Figure 7.2: KM image of the OUT

of a two dimensional image. Based on the well known regular and central moments from statistics and the classical mechanics 7 moments are obtained which are invariant against translation, rotation and scaling.
Let $f(x, y)$ be a discretised grayscale image, then the regular moment m_{pq} of the order $p + q$ can be defined as

$$m_{pq} = \sum_x \sum_y x^p y^q f(x, y) \qquad \text{with } p, q = 0, 1, 2 \ldots \tag{7.1}$$

Obviously, m_{00} denotes the total image weight, i.e. cumulative amplitude sum of entirely all pixels. In analogy to classical mechanics the centre of gravity of the image yields

$$\overline{x} = \frac{m_{10}}{m_{00}} \qquad \text{and} \qquad \overline{y} = \frac{m_{01}}{m_{00}} \tag{7.2}$$

for the x and y dimension, respectively. By relating the regular moments with the centres of gravity, the central moments can be obtained as

$$\mu_{pq} = \sum_x \sum_y (x - \overline{x})^p (y - \overline{y})^q f(x, y) \qquad \text{with } p, q = 0, 1, 2 \ldots \tag{7.3}$$

Hence, by the shift of $(\overline{x}, \overline{y})$ an object adapted coordinate system is provided which makes the central moments invariant against translation. In the original theorem [57] a normalisation factor depending on the regarded order

is introduced to achieve invariance against object scaling. However, due to direct TOF evaluations scaling does not appear in Radar images. Moreover, objects o1 and o2 have both a square cross section of different size. The final rotation invariance is therefore obtained by the 7 Hu moments which are a non-linear combination of the central moments:

$$\begin{aligned}
h_1 =& \ \mu_{20} + \mu_{02} \\
h_2 =& \ (\mu_{20} - \mu_{02})^2 + 4\mu_{11}^2 \\
h_3 =& \ (\mu_{30} - 3\mu_{12})^2 + (3\mu_{21} + \mu_{03})^2 \\
h_4 =& \ (\mu_{30} - \mu_{12})^2 + (\mu_{21} + \mu_{03})^2 \\
h_5 =& \ (\mu_{30} - 3\mu_{12})(\mu_{30} + \mu_{12}) \left[(\mu_{30} - \mu_{12})^2 - 3(\mu_{21} - \mu_{03})^2\right] + \\
& \ (3\mu_{21} - \mu_{03})(\mu_{21} + \mu_{03}) \left[3(\mu_{30} + \mu_{12})^2 - (\mu_{21} + \mu_{03})^2\right] \\
h_6 =& \ (\mu_{20} - \mu_{02}) \left[(\mu_{30} + \mu_{12})^2 - (\mu_{21} + \mu_{03})^2\right] + \\
& \ 4\mu_{11}(\mu_{30} + \mu_{12})(\mu_{21} + \mu_{03}) \\
h_7 =& \ (3\mu_{21} - \mu_{30})(\mu_{30} + \mu_{12}) \left[(\mu_{30} + \mu_{12})^2 - 3(\mu_{21} + \mu_{03})^2\right] + \\
& \ (3\mu_{21} - \mu_{03})(\mu_{21} + \mu_{03}) \left[3(\mu_{30} - \mu_{12})^2 - (\mu_{21} + \mu_{03})^2\right]. \qquad (7.4)
\end{aligned}$$

It is well known in the field of image processing that the moments perform more robust on grayscale images [63]. Because of this, the KM images (also shown in Figure 5.7 for the second reference alphabet) serve as the basis for all moment based features, i.e. the eccentricity feature $\widetilde{F}_{\mathrm{EC}}$ discussed later and the moment based feature $\vec{\widetilde{\mathbf{F}}}_{\mathrm{MI}}$ which is determined as

$$\vec{\widetilde{\mathbf{F}}}_{\mathrm{MI}} = [h_1 \ \ h_2 \ \ h_3 \ \ h_4 \ \ h_5 \ \ h_6 \ \ h_7]\,. \qquad (7.5)$$

7.1.2 Geometrical Features

For the processing of the geometrical features the target points of the feature map are clustered. The i-th and j-th target point are merged to one cluster if the condition $\left|\vec{\mathbf{P}}^i_{\mathrm{tp}} - \vec{\mathbf{P}}^j_{\mathrm{tp}}\right| \leq 0.01$ m with $i = j = 1, 2, 3 \ldots N$ holds true for a total number of N target points. Subsequently, every cluster is substituted

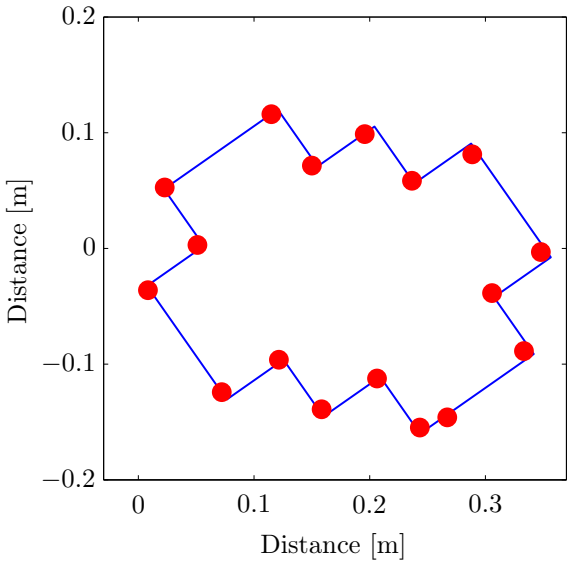

Figure 7.3: Cluster Map of the OUT

by its individual centre of gravity $(\overline{x}, \overline{y})$. Finally, the cluster map consists of the obtained centres of gravity. In both Figures 7.1 and 7.3 the centres of gravity for the OUT are depicted in red. For the further processing the cluster map consists of a binary image with pixels of the value 1 for a member of the cluster and pixels of the value 0 otherwise. Thus, additonal redundancy is removed and the relevant information with regard to the purpose is reduced to a minimum which significantly decreases the computational load.

Eccentricity

The eccentricity $\tilde{\epsilon}$ quantifies the degree of elongation versus circularity of an object and ranges from 0 to 1. It equals 0 for an object of circular cross section and 1 for a straight line. In particular, the eccentricity denotes the relation of the major object axis to the minor object axis. The major object axis is the longest straight line through the object and the minor axis is the longest straight line through the object subject to be perpendicular to the

major axis [63]. The eccentricity is based on the second-order moments and the exact calculation yields

$$\tilde{\epsilon} = \frac{(\mu_{20} - \mu_{02})^2 + 4\mu_{11}^2}{(\mu_{20} + \mu_{02})^2}. \tag{7.6}$$

As the moments are invariant against translation and rotation the same applies for the eccentricity feature which finally yields $\widetilde{F}_{\mathrm{EC}} = \tilde{\epsilon}$.

Fitting Circle

The fitting circle feature is a simple measure for the radial extension of an object. In contrast to a bounding box the fitting circle is rotation invariant. The radius of the fitting circle equals the distance between the centre of gravity $(\overline{x}, \overline{y})$ of the cluster map and the cluster member which is furthest away. Mathematically this can be formulated as

$$r_{\max} = \max_{c} \left| \begin{pmatrix} \overline{x} \\ \overline{y} \end{pmatrix} - \vec{\mathbf{P}}_{\mathrm{cl}}^{c} \right| \qquad \text{with } c = 1, \ldots, C \tag{7.7}$$

where $\vec{\mathbf{P}}_{\mathrm{cl}}^{c}$ is the position vector to the c-th member of the cluster and a total number of C cluster members. For the sake of illustration, the fitting circle of the OUT is plotted with its relevant quantities in Figure 7.4. The fitting circle feature is invariant against translation and rotation and yields $\widetilde{F}_{\mathrm{FC}} = 2\pi r_{\max}$.

Form Factor

The form factor denotes the compactness of the object by relating the radial extension and the total image weight of the cluster map m_{00} to each other. Thus, it is an efficient feature to discriminate objects of similar dimensions though they exhibit a diverse contour which induces a different cluster map. The form factor feature is defined as

$$\widetilde{F}_{\mathrm{FF}} = \frac{r_{\max}^2}{4\,\pi\,m_{00}} \tag{7.8}$$

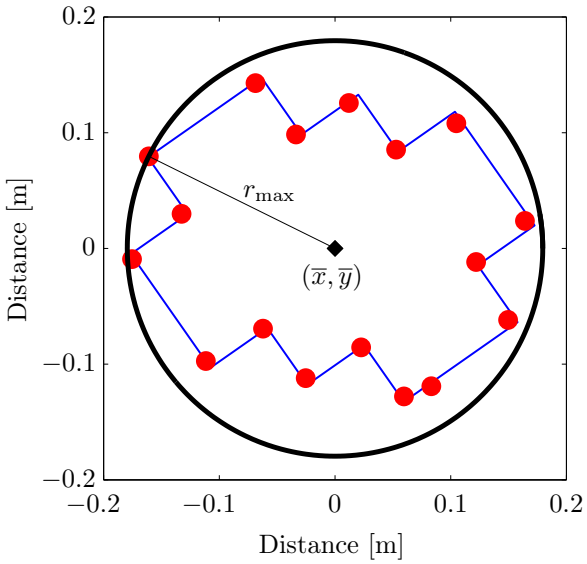

Figure 7.4: Fitting circle illustration of the OUT

and is invariant against translation and rotation.

Inertia

The moment of inertia is a measure from classical mechanics which quantifies the inertia of a rotating object with respect to its mass distribution. The object is split into k small pieces with the mass $m_1, m_2, \ldots m_k$ which exhibit the distances $r_1, r_2, \ldots r_k$ from the axis of rotation. The moment of inertia of the object is $I = m_1 r_1^2 + m_2 r_2^2 + \ldots + m_k r_k^2$. By the evaluation of I with respect to the axis of rotation the classical moment of inertia is invariant against translation and rotation [164].

The adaption of the inertia calculation to the cluster map presumes a sequence of successive boundary pixels derived from the set of cluster members. At first, the object is shifted by its centre of gravity $(\overline{x}, \overline{y})$ so that it is placed around the origin of axis. With this locality a polar coordinates description of the cluster members with monotonously increasing angle is

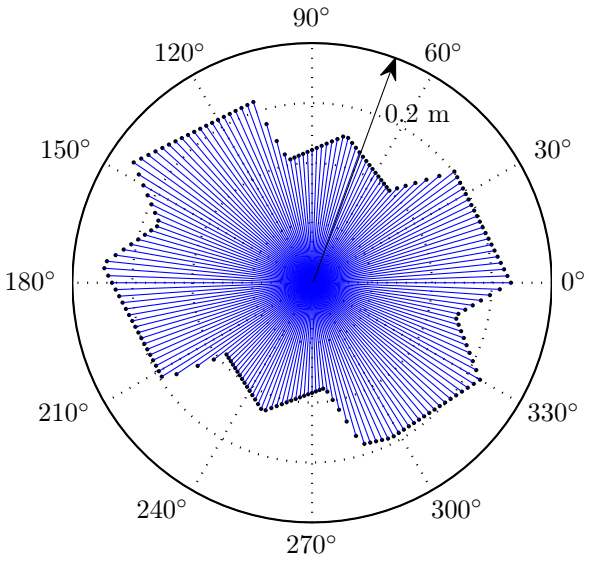

Figure 7.5: Angular sampled contour of the OUT for inertia calculations

feasible. Afterwards, the cluster members are connected with sequential angles in ascending order. Finally, the resulting curve is sampled equiangular at a 1° grid which results in 360 discrete samples with the polar coordinates $r_n \cdot \exp(\mathrm{j}\pi\frac{n}{360})$ with $n = 0 \ldots N$ and $N = 359$. Here, r_n is the n-th distance from the origin to the regarded sample with the corresponding angle n. An illustration of this processing for the OUT is shown in Figure 7.5. For the sake of clarity, every second sample is removed in the plot. The final inertia feature is hence determined by

$$\widetilde{F}_{\mathrm{IN}} = \sum_{n=0}^{N} r_n^2 \tag{7.9}$$

and is invariant against translation and rotation.

7.1.3 Texture Features

The texture features consist of the Fourier descriptors and the curvature scale to describe the structural composition and distribution of pixels of the OUT. Similar to the previous determination of the inertia both features presume a sequence of successive boundary pixels derived from the set of cluster members. However, in contrast to the inertia the boundary for the texture analysis is obtained by an equidistant sampling with a pixelwise sample period explained in the following.

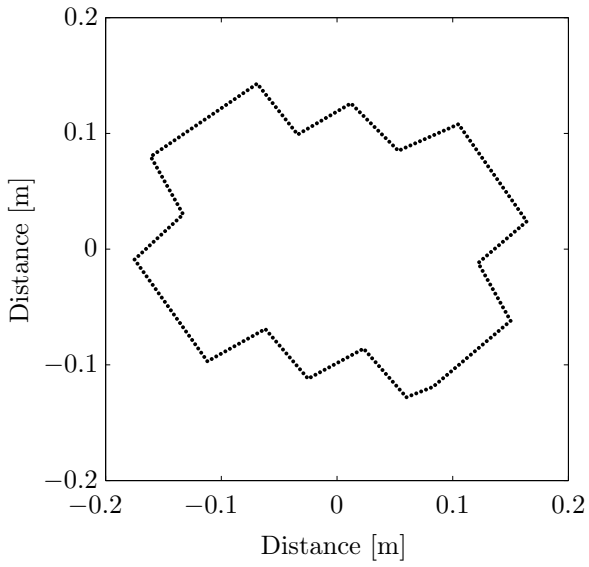

Figure 7.6: Equidistant sampled contour of the OUT for the texture analysis

Fourier Descriptors

The Fourier transformation representation of curves as the boundary of patterns is well known and has been popular over several decades [35] [63] [84]. Due to the Fourier theorem the transformation of the coordinates of an equidistantly sampled curve provides a set of complex values, i.e. the Fourier descriptors. These descriptors represent the curve in the frequency domain.

Let the boundary curve of the OUT of Figure 7.6 consist of P samples which can be described by a complex value as $z(p) = x(p)+\mathrm{j}y(p)$ with $p = 0, \ldots P-1$ as the parameter. Then the Fourier descriptors yield

$$Z(k) = \sum_{p=0}^{P-1} z(p) \exp\left(-\mathrm{j}2\pi \frac{pk}{P}\right) \qquad \text{with } k = 0, \ldots, P-1. \tag{7.10}$$

Because $z(p)$ is complex the Fourier descriptors $Z(k)$ of the first half are not the complex conjugate of the latter half and thus exhibit individual information. For the sake of not to exceed the framework of this thesis the Fourier transformation shall not be explained further. Interested readers may refer to the vast existing literature on this topic, e.g. [102] [106].

Due to the summation over a periodic function in equation (7.10), a translative shift of the curve just influences the DC $Z(0)$. However, translation invariance is already maintained by using a coordinate system whose origin is aligned to the centre of gravity.
Due to the Fourier theorem a rotation of the curve solely induces a constant phase shift of every descriptor. However, within this thesis the orientation invariance is provided by using the absolute value of all descriptors.
A scale invariance is not desired within this OR algorithm. However, the scaling effects shall be explained for the sake of completeness: a scaling of the curve causes a scaling of the descriptors with the same factor. Thus a normalisation with the absolute value of the first descriptor would provide scale invariance.

The lower frequencies provide information about the general shape and dimension of the area bounded by the curve whereas the higher frequencies contain information about the fine structures and small details of the curve evolution. Because of this, a small subset of the descriptors is sufficient to cover the discrepancy of the objects while reducing the computational load. The absolute value of the descriptors converges to zero after a couple

of indexes anyway. Within this thesis the Fourier descriptor feature yields $\vec{\vec{\mathbf{F}}}_{\mathrm{FD}} = (|Z(1)|\ |Z(2)|\ \ldots |Z(20)|)$.

Curvature Scale

The curvature of a curve expresses the offset of the curve evolution from a straight line. Thus, it is defined as

$$\kappa(p) = \lim_{h \to 0} \frac{\varphi}{h} \tag{7.11}$$

where φ is the angle between both tangent vectors $\vec{\mathbf{t}}(p)$ and $\vec{\mathbf{t}}(p+h)$ with the curve parameter p. Let the equidistant samples of a curve be described by a parametric vector equation as $\vec{\mathbf{z}}(p) = [x(p)\ y(p)]$ with $p = 0, \ldots P-1$. The curvature of the curve $\vec{\mathbf{z}}(p)$ can be expressed [18] as

$$\kappa(p) = \frac{\dot{x}(p)\ddot{y}(p) - \ddot{x}(p)\dot{y}(p)}{\left(\dot{x}^2(p) + \dot{y}^2(p)\right)^{3/2}} \tag{7.12}$$

where a single and double dot about a variable denotes the first and second derivative with respect to the parameter p, respectively. In contrast to the Fourier theorem the curvature scale of a curve contains local information. This means, that the p-th sample of the curvature contains the geometric information of the p-th sample of the curve.

However, the equidistant sampled contour of the OUT in Figure 7.6 consists of straight segments. Thus, the resulting curve exhibits a change of orientation just in the sample which connects two segments. In this case, the corresponding curvature is a function which equals zero except the sample of each segment connection where $\kappa(p)$ equals a Dirac delta.
The classification and discrimination of a pair of objects which exhibit such curvature scale is challenging and extremely error-prone; a single pixel offset of the connection sample (due to noise e.g.) shifts the Dirac delta and highly complicates the comparison. To overcome this issue the raw curve is

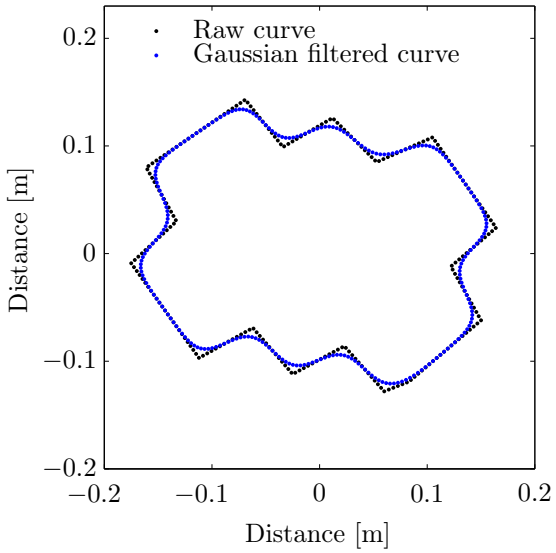

Figure 7.7: Equidistant sampled contour of the OUT before and after the application of a Gaussian filter

pre-processed by means of the Gaussian filter [93]

$$g(p) = \frac{1}{\sigma_{\mathrm{cs}}\sqrt{2\pi}} \exp\left(-p^2/2\sigma_{\mathrm{cs}}^2\right) \tag{7.13}$$

where σ_{cs} is the standard deviation of the filter. In this thesis $\sigma_{\mathrm{cs}} = \lambda_{\mathrm{c}}$ where λ_{c} is the wavelength which corresponds to the centre frequency.

An illustration of the raw curve before and after the application of a Gaussian filter is shown in Figure 7.7. As a consequence, the shape of $\kappa(p)$ is blurred from a Delta dirac to a Gaussian shape which is shown in Figure 7.8. Thus, after the Gaussian filtering the change of orientation in the evolution of the curve as well as the correponding $\kappa(p)$ takes place leisurely. The degree of bluring is determined by σ_{cs}. The exact quantification must satisfy a minimum expansion of the Dirac deltas while ensuring a robust discrimination of meaningful orientation changes without an overlapping.

Due to the alignment of the coordinate system to the centre of gravity the

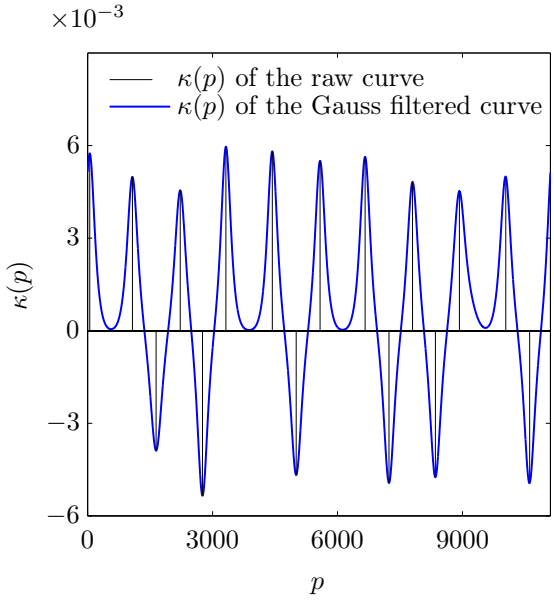

Figure 7.8: $\kappa(p)$ of the OUT contour before and after the application of a Gaussian filter

curvature scale analysis is invariant against translation. However, a rotation of the OUT would circularly shift $\kappa(p)$. Thus, the curvature scale analysis is not invariant against rotation which must be taken into account in the classification step of the OR. The final curvature scale feature is defined as $\vec{\widetilde{\mathbf{F}}}_{\mathrm{CS}} = \kappa(p)$ with the curvature of the Gaussian filtered curve $\vec{\mathbf{z}}(p) * g(p)$, where $*$ is the convolution operator.

7.2 Object Discrimination and Classification - Full Track

The final step of the OR is the comparison of the OUT with each of the twelve reference objects by means of the previously derived features. Thus, the level of discrimination between the OUT and every possible reference object can be quantified. A subsequent classification and the determination

of a final choice is performed by the OR algorithm.

As previously discussed, UWB Radar technology is especially a promising sensing technique for emergency scenarios. In such situations the demands on real-time processing and measurement time of the systems are strictly severe. Hence, to highly satisfy real-time capability the OR was designed from the outset with a simple classification algorithm. Thus, the support of vector machines, neural networks and other OR algorithms with vast computational loads were excluded completely. The following discussion refers to the description of the measurement campaign in the section 3.4.2 which was performed for the sake of an experimental validation.

Previously, in this chapter the determination of the features has been discussed. A set of reference quantities will be assigned to each of the twelve reference objects:

$$\mathcal{R}^j = \left\langle \vec{\widetilde{\mathbf{F}}}^j_{\mathrm{MI}}, \widetilde{F}^j_{\mathrm{EC}}, \widetilde{F}^j_{\mathrm{FC}}, \widetilde{F}^j_{\mathrm{FF}}, \widetilde{F}^j_{\mathrm{IN}}, \vec{\widetilde{\mathbf{F}}}^j_{\mathrm{FD}}, \vec{\widetilde{\mathbf{F}}}^j_{\mathrm{CS}} \right\rangle \quad \text{with } j = 1, \ldots, 12. \tag{7.14}$$

The i-th MUT for the OR evaluation is assigned to the i-th feature set as

$$\mathcal{M}^i = \left\langle \vec{\widetilde{\mathbf{F}}}^i_{\mathrm{MI}}, \widetilde{F}^i_{\mathrm{EC}}, \widetilde{F}^i_{\mathrm{FC}}, \widetilde{F}^i_{\mathrm{FF}}, \widetilde{F}^i_{\mathrm{IN}}, \vec{\widetilde{\mathbf{F}}}^i_{\mathrm{FD}}, \vec{\widetilde{\mathbf{F}}}^i_{\mathrm{CS}} \right\rangle \quad \text{with } i = 1, \ldots, 80 \tag{7.15}$$

which contains the same feature evaluation as the reference evaluation. The variable i ranges until 80 because, as explained in the chapter 3.4.2, the OR validation setup consists of 80 MUTs per OUT.
With a simple MMSE classifier the i-th MUT $\mathcal{M}^i$ gets a MMSE value for the j-th reference object $\mathcal{R}^j$ as

$$\mathrm{MMSE}^i(j) = \frac{1}{7}\left[\sum_{k=1}^{K=6}\left(\mathcal{M}^i(k) - \mathcal{R}^j(k)\right)^2 + \left(1 - \max_{\tau}\left(R_{\mathcal{M}^i(7)\,\mathcal{R}^j(7)}(\tau)\right)\right)^2\right] \tag{7.16}$$

where the normalised cross-correlation $R_{\mathcal{M}^i(7)\,\mathcal{R}^j(7)}(\tau)$ expresses the similarity between the i-th MUT and the j-th reference object with regard to the curvature scale feature. This operation is necessary because the curvature scale is not invariant against rotation. A rotational offset of the OUT causes a circular shift of the curvature scale feature. However, this mismatch can be compensated with a correlation evaluation. The range of the normalised correlation varies between 0 for orthogonal signals and 1 for equal signals.

The recognition for the i-th MUT is finally performed by evaluating the MMSE classifier with a minimum operator with regard to the j-th reference object. Hence, the i-th MUT is recognised as the $\hat{\mathrm{o}}^i_{\mathrm{MMSE}}$ reference object which can be mathematically formulated as

$$\hat{\mathrm{o}}^i_{\mathrm{MMSE}} = \arg\min_j \left(\mathrm{MMSE}^i(j)\right). \tag{7.17}$$

As previously mentioned in the section 3.4.2, the investigated OR algorithm is experimentally validated within an immense measurement campaign. In order to avoid too ideal circumstances, every OUT has been measured 80 times subject to a translative as well as a rotational offset from the centre of the circular track. The correct recognition rate for each object as the ultimate result of the OR algorithm is provided in Figure 7.9.

7.3 Object Discrimination and Classification - Restricted Track

As can be seen in Figure 7.9 the OR algorithm provides excellent recognition rates for all objects without exception.

Further performance evaluations of the OR algorithm shall be carried out under severe restrictions of the antenna track. To maintain a realistic relevance and to keep close to real world conditions the sensor tracks are restricted to

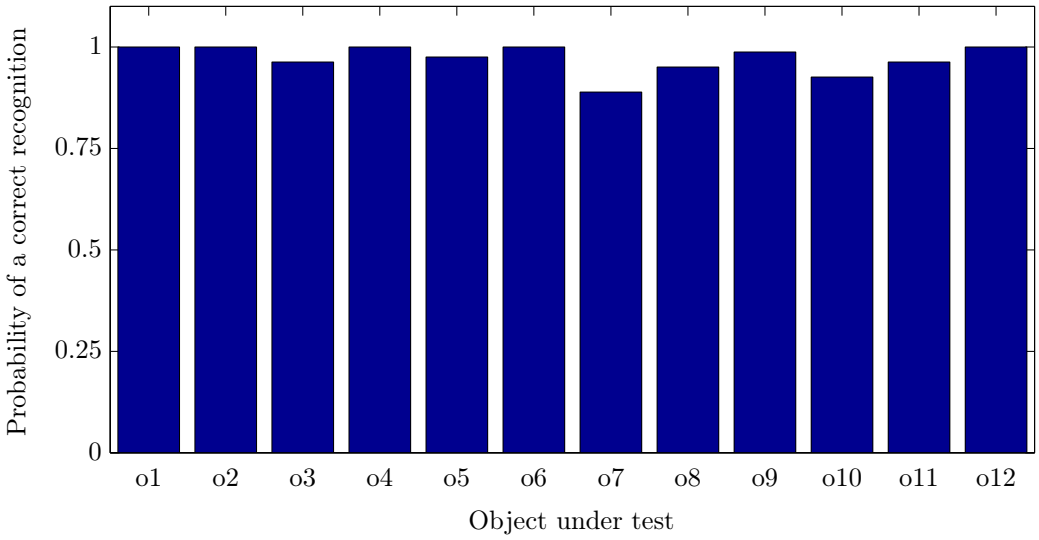

Figure 7.9: Results of the experimental OR validation for 80 arbitrary full track measurements

270° and 180°, respectively. For the sake of a fair validation of exclusively the OR algorithm the acquisition and processing of the data remains unchanged except one necessary issue:

- Due to the restricted track the obtained cluster map of the OUT is incomplete. Hence, the seven features have to be extracted from incomplete data. Due to the restriction of the track, the centre of gravity does not coincide anymore with the centre of gravity of the full track cluster map. Thus, the classification and discrimination by means of the existing full track reference set is not feasible any more.
  All object features except the moment based ones $\vec{\widetilde{\mathbf{F}}}_{\mathrm{MI}}$ and $\widetilde{F}_{\mathrm{EC}}$ are strongly depending on the geometrical relationship between the centre of gravity and the cluster members and thus the curves determined by them.

However, to counteract the limitations of a restricted track a mesh of pseudo centres of gravity which define possible deviations from the exact centre of

gravity are taken into account as follows:
First, the exact centre of gravity of the obtained cluster map is calculated. The more the track is restricted the more the position of the centre of gravity deviates from the one of the full track.
Secondly, a mesh of pseudo centres of gravity are spanned around the calculated centre of gravity. The mesh consists of pseudo centres of gravity both in horizontal and vertical dimension with a 5 mm grid and a mesh dimension of 30×30 cm^2 around the calculated centre of gravity.

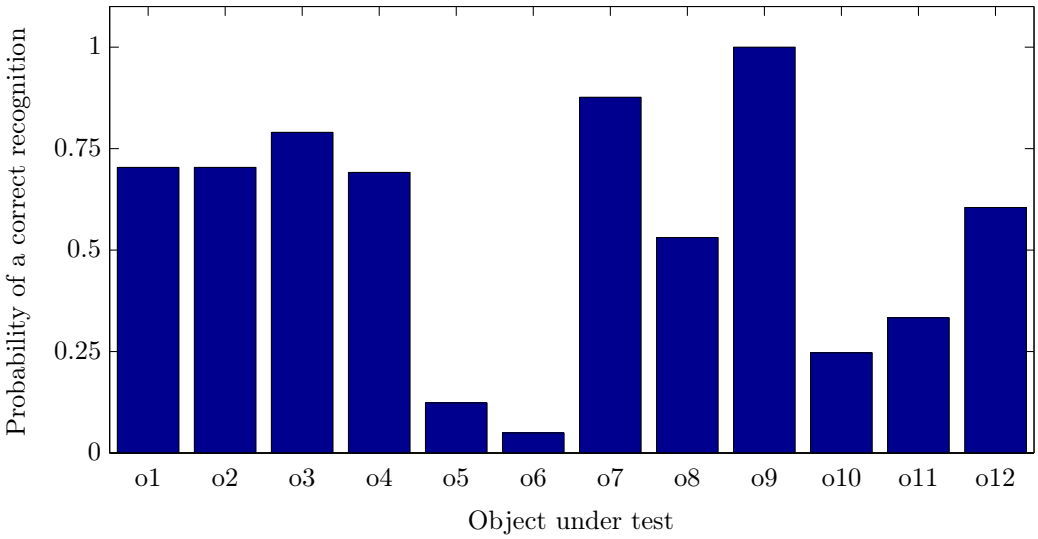

Figure 7.10: Results of the experimental OR validation for 80 arbitrary restricted 270° track measurements

Let the resulting total number of pseudo centres of gravity plus the exact one be N_{sub} for the sub cluster map. Hence, the i-th MUT set $\mathcal{M}^i$ from equation (7.15) consists of N_{sub} possible evaluations. Each evaluation is performed for one of the N_{sub} centres of gravity. Consequently, the MMSE classification in equation (7.16) for the i-th MUT is carried out N_{sub} times for every reference object. Note here, that the second term in equation (7.16) for the correlation based evaluation is performed in parallel and the overall

best match is chosen. The final evaluation of the OR is performed with a similar minimum operation as equation (7.17). The only difference is that the global minimum is carried out which means that first the minimum of the N_{sub} subsets are evaluated per reference object. Subsequently, the minimum is evaluated for each reference object. The results for the OR with a 270° track and a MMSE classifier are shown in Figure 7.10.

7.4 Improved Object Recognition with a Bayes Classifier

As expected and can be seen in Figure 7.10, the restriction of the track to 270° decreases the recognition rate partly minimally and partly drastically depending on the OUT.

One reason is that sections of the objects are similar or even equal to other objects, e.g. this holds for o1, o3, o6, o7 and o12. These objects exhibit one or more edges with 30 cm flat surfaces to the left and to the right. Hence, the Radar signature of these parts will increase the ambiguity which downgrades the recognition rate.
Another reason is that the features of the reference set $\mathcal{R}^j$ for the j-th object oj are extracted from the full track reference measurement. Thus, restricted MUTs are compared with non-restricted references.

A promising strategy for the evaluation of restricted tracks is the partial consideration of the object features for a new set of a more appropriate reference alphabet. Thus, a training sequence which provides the Radar signature statistics of every object is generated from the reference full track measurement by splitting it into several 270° segments. A segment starts at $0°, 12°, 24°$... and so forth in multiples of 12° until 360° which results in 30 segments. Thereby, a training sequence of 30 segments is generated that cov-

ers the whole Radar signature as a compilation. Note here, that the training sequence is still gathered from the single full track reference measurement without increasing the experimental workload or any other hardware effort.

A superior classification shall be discussed in the following where the training sequence provides a priori information. Thus, a more robust and reliable decision shall be reached by exploiting the Radar signature statistics of each object by means of the training sequence. The probability model for the decision on the object as a result of the OR algorithm is based on the probability

$$P\left(\mathrm{o}j\right|\mathcal{M}_{270}^{i}) \tag{7.18}$$

which denotes the conditional probability of the j-th object given the i-th restricted MUT feature set. The output of the statistical classifier to be designed is hence the j-th object that maximises the conditional probability in equation (7.18). This results in a minimisation of the average erroneous recognition probability.

Due to the Bayes' theorem [28] the conditional probability in (7.18) can be expressed as

$$P\left(\mathrm{o}j|\mathcal{M}_{270}^{i}\right) = \frac{P\left(\mathcal{M}_{270}^{i}|\mathrm{o}j\right)\ P\left(\mathrm{o}j\right)}{P\left(\mathcal{M}_{270}^{i}\right)}. \tag{7.19}$$

The first term $P\left(\mathcal{M}_{270}^{i}|\mathrm{o}j\right)$ in the numerator is called the *likelihood* of oj with respect to $\mathcal{M}_{270}^{i}$ and expresses the conditional probability of the MUT feature set assigned with the j-th object. The second term $P\left(\mathrm{o}j\right)$ denotes the *prior* probability of the j-th object. The term $P\left(\mathcal{M}_{270}^{i}\right)$ in the denominator is called the *evidence* and yields in the particular case of 12 objects for the i-th restricted MUT feature set

$$P\left(\mathcal{M}_{270}^{i}\right) = \sum_{j=1}^{12} P\left(\mathcal{M}_{270}^{i}|\mathrm{o}j\right)\ P\left(\mathrm{o}j\right). \tag{7.20}$$

The evidence can be regarded as a normalisation factor which guarantees that the *posterior* probability $P\left(\mathrm{o}j|\mathcal{M}^i_{270}\right)$ ranges between 0 and 1, as can be seen when the equation (7.20) is inserted into (7.19). For the sake of clarity, a linguistic notation of the Bayesian classifier in the equation (7.19) shall be denoted which yields

$$\text{posterior} = \frac{\text{likelihood} \cdot \text{prior}}{\text{evidence}}.$$

In practical evaluations for a decision making process the evidence is of minor importance as it has a scaling character. The numerator is evaluated for each object in order to determine the j-th object that maximises the posterior probability $P\left(\mathrm{o}j|\mathcal{M}^i_{270}\right)$ in equation (7.19). Hence, this results in the solution for the initial objective of the discussion in equation (7.18), i.e. the probability of the object oj given the i-th measured restricted set $\mathcal{M}^i_{270}$.

In the field of Bayesian methods the prior and the likelihood in the numerator are rarely, if ever, completely known. Typically, vague information or design parameters and general kowledge is available in the best case [28]. However, in the particular case of restricted tracks the previously discussed training sequence fully provides the necessary information.
The prior term expresses the appearance probability of the $j-$th object within the OR process. Due to the setting of the OR task, the prior probability $P\left(\mathrm{o}j\right)$ can be assumed uniformly distributed. This means, that no object is prioritised. Hence, it exhibits a scaling character and can be neglected for a decision making process.
The quantification of the likelihood term is based on the estimation of the statistical distribution of the object features within a training sequence. Hence, the probability density functions (PDF) which are assumed to be Gaussian distributions have to be modelled with the information provided by the training sequence. Since the 7 features discussed in the section 7.1 consist of vectors as well as scalars the estimation of the PDFs slightly differ:

Scalar features The geometrical features i.e. eccentricity $\widetilde{F}_{\mathrm{EC}}$, fitting circle $\widetilde{F}_{\mathrm{FC}}$, form factor $\widetilde{F}_{\mathrm{FF}}$ and inertia $\widetilde{F}_{\mathrm{IN}}$ are single scalar quantities. Thus, each distribution of every feature resembles an *univariate* Gaussian distribution

$$f_x(x) = \frac{1}{\sigma\sqrt{2\pi}} \exp\left(-\frac{(x-\mu)^2}{2\sigma^2}\right) \tag{7.21}$$

for the random variable x with the expectation parameter μ and the standard deviation σ. The univariate Gaussian distribution is entirely determined by these two parameters. The estimation of both parameters by means of the 30 segments per training sequence yields

$$\mu = \frac{1}{30}\sum_{k=1}^{30} x_k \qquad \text{and} \qquad \sigma = \sqrt{\frac{1}{30}\sum_{k=1}^{30}(x_k-\mu)^2}.$$

Trivially, the random variable x in this example is substituted with the feature values provided by the training sequence. Overall, the distribution of each of the four features is performed for every object.

Vector valued features The moment invariant feature $\vec{\widetilde{\mathbf{F}}}_{\mathrm{MI}}$, the Fourier descriptors $\vec{\widetilde{\mathbf{F}}}_{\mathrm{FD}}$ and the curvature scale $\vec{\widetilde{\mathbf{F}}}_{\mathrm{CS}}$ are vector valued features. The Gaussian distribution is expressed by a *multivariate* Gaussian distribution

$$f_{\vec{\mathbf{x}}}(\vec{\mathbf{x}}) = \frac{1}{\sqrt{(2\pi)^k|\boldsymbol{\Sigma}|}} \exp\left(-\frac{1}{2}(\vec{\mathbf{x}}-\vec{\boldsymbol{\mu}})^{\mathrm{T}}\boldsymbol{\Sigma}^{-1}(\vec{\mathbf{x}}-\vec{\boldsymbol{\mu}})\right) \tag{7.22}$$

for the random vector $\vec{\mathbf{x}}$ with k components. The parameter $\boldsymbol{\Sigma}$ denotes the symmetric covariance matrix, $\vec{\boldsymbol{\mu}}$ is the mean vector with k components, $(\cdot)^{-1}$ is the inverse operator and $(\cdot)^{\mathrm{T}}$ is the transpose operator, respectively. Analogously to the univariate case the multivariate Gaussian distribution is entirely determined with both the parameters $\boldsymbol{\Sigma}$ and $\vec{\boldsymbol{\mu}}$. Hence, to express the vector valued features as a Gaussian

distribution, the parameter estimation based on the training sequence which consits of 30 segments yields

$$\vec{\boldsymbol{\mu}} = \frac{1}{30}\sum_{k=1}^{30}\vec{\mathbf{x}} \qquad \text{and} \qquad \boldsymbol{\Sigma} = \frac{1}{30}\sum_{k=1}^{30}(\vec{\mathbf{x}}-\vec{\boldsymbol{\mu}})\,(\vec{\mathbf{x}}-\vec{\boldsymbol{\mu}})^{\mathrm{T}}.$$

Once again the mean quantity as well as the deviation is again estimated by the arithmetic mean of the samples. This strategy meets the demands to a satisfying degree.

The crucial step for a robust Bayes estimation is the quantification of the the likelihood $P\left(\mathcal{M}^i_{270}|\mathrm{o}j\right)$ which shall be described in the following:

Let $\mathcal{M}^i_{270} = \left\langle \vec{\widetilde{\mathbf{F}}}^i_{\mathrm{MI}}, \widetilde{F}^i_{\mathrm{EC}}, \widetilde{F}^i_{\mathrm{FC}}, \widetilde{F}^i_{\mathrm{FF}}, \widetilde{F}^i_{\mathrm{IN}}, \vec{\widetilde{\mathbf{F}}}^i_{\mathrm{FD}}, \vec{\widetilde{\mathbf{F}}}^i_{\mathrm{CS}} \right\rangle$ be the feature set of the i-th MUT with $i = 1, \ldots, 80$. Further, let the reference set $\mathcal{R}^j$ for the j-th object with $j = 1, \ldots, 12$ consist of the univariate Gaussian distributions $f_{\widetilde{F}^j_{\mathrm{EC}}}(\widetilde{F}^j_{\mathrm{EC}})$, $f_{\widetilde{F}^j_{\mathrm{FC}}}(\widetilde{F}^j_{\mathrm{FC}})$, $f_{\widetilde{F}^j_{\mathrm{FF}}}(\widetilde{F}^j_{\mathrm{FF}})$, $f_{\widetilde{F}^j_{\mathrm{IN}}}(\widetilde{F}^j_{\mathrm{IN}})$ as well as the multivariate Gaussian distributions $f_{\vec{\widetilde{\mathbf{F}}}^j_{\mathrm{MI}}}(\vec{\widetilde{\mathbf{F}}}^j_{\mathrm{MI}})$, $f_{\vec{\widetilde{\mathbf{F}}}^j_{\mathrm{FD}}}(\vec{\widetilde{\mathbf{F}}}^j_{\mathrm{FD}})$, $f_{\vec{\widetilde{\mathbf{F}}}^j_{\mathrm{CS}}}(\vec{\widetilde{\mathbf{F}}}^j_{\mathrm{CS}})$, extracted from the a priori processed training sequence.

Under the assumption of conditional independence the likelihood $P\left(\mathcal{M}^i_{270}|\mathrm{o}j\right)$ for the i-th MUT can be computed as the product of the probability quantities extracted from the reference densities for the feature quantities of the i-th MUT:

$$\begin{aligned} P\left(\mathcal{M}^i_{270}|\mathrm{o}j\right) = {} & f_{\vec{\widetilde{\mathbf{F}}}^j_{\mathrm{MI}}}(\vec{\widetilde{\mathbf{F}}}^i_{\mathrm{MI}}) \cdot f_{\widetilde{F}^j_{\mathrm{EC}}}(\widetilde{F}^i_{\mathrm{EC}}) \cdot f_{\widetilde{F}^j_{\mathrm{FC}}}(\widetilde{F}^i_{\mathrm{FC}}) \cdot \\ & f_{\widetilde{F}^j_{\mathrm{FF}}}(\widetilde{F}^i_{\mathrm{FF}}) \cdot f_{\widetilde{F}^j_{\mathrm{IN}}}(\widetilde{F}^i_{\mathrm{IN}}) \cdot f_{\vec{\widetilde{\mathbf{F}}}^j_{\mathrm{FD}}}(\vec{\widetilde{\mathbf{F}}}^i_{\mathrm{FD}}) \cdot \\ & f_{\vec{\widetilde{\mathbf{F}}}^j_{\mathrm{CS}}}(\vec{\widetilde{\mathbf{F}}}^i_{\mathrm{CS}}) \qquad \text{with } j = 1, \ldots, 12. \end{aligned} \tag{7.23}$$

Finally, a recognition in terms of a Bayesian decision theory can be performed for the i-th MUT by evaluating a maximum operator on the equation (7.23)

with regard to the j-th reference object. Hence, the i-th MUT is recognised as the $\hat{\mathrm{o}}^i_{\mathrm{Bayes}}$ reference object which can be mathematically formulated as

$$\hat{\mathrm{o}}^i_{\mathrm{Bayes}} = \arg\max_j \left(P\left(\mathcal{M}^i_{270}|\mathrm{o}j\right)\right) \qquad \text{with } j = 1, \ldots, 12. \tag{7.24}$$

As previously mentioned in the section 3.4.2, the investigated OR algorithm has been experimentally validated within an immense measurement campaign. To provide a fair classification of the influence of the track restriction, the same measurement campaign except a premature stop of the track has been carried out. Thus, every OUT has been measured 80 times subject to the same translative as well as rotational offset from the centre of the circular track. The recognition rate for each object as the result of the OR algorithm for restricted tracks with a Bayes classifier is provided in Figure 7.11 for a 270° circular track. As a proof of plausibility the track is restricted more severely to 180° with the results shown in Figure 7.12. For the sake of comparison the MMSE results are plotted as well in the diagrams.

As can be seen in Figure 7.11 9 of 12 recognition rates could be increased remarkably with the Bayes classifier. The most considerable improvements are exhibited by the objects o5 and o6 with an increase of more than 60% compared to the MMSE classifier. However, object o3, o7 and o9 are recognised more reliable with the MMSE.

Most of the ambiguity is caused by objects which are similar or partly even equal, i.e. o1, o3, o6, o7 and o12. These objects exhibit one or more edges with 30 cm flat surfaces to the left and to the right which downgrades plausibly the recognition rate.

The main reason for the outstanding performance of the Bayes classifier is that it exhibits more reliable and capable information by splitting the reference set into 270° and 180° segments, respectively.

In contrast, the MMSE classifier exhibits a reference set extracted from the full track reference measurement. Thus, the restricted MUTs are compared with non-restricted references.

That is e.g. the reason why the MMSE classifier fails for objects o1, o2 and o4 with the 180° track in Figure 7.12. With half of the full track the objects o1, o2 and o4 always exhibit a cluster map with only 3 cluster members due to the severly restricted track. Consequently in all cases object o3 is chosen most probably because the object o3 exhibits *exactly* 3 cluster members in the full track reference.
This is a decision which is wrong for o1, o2 and o4 but is true for o3; that is why the MMSE classifier has a pretty good matching with object o3 with the 180° track.

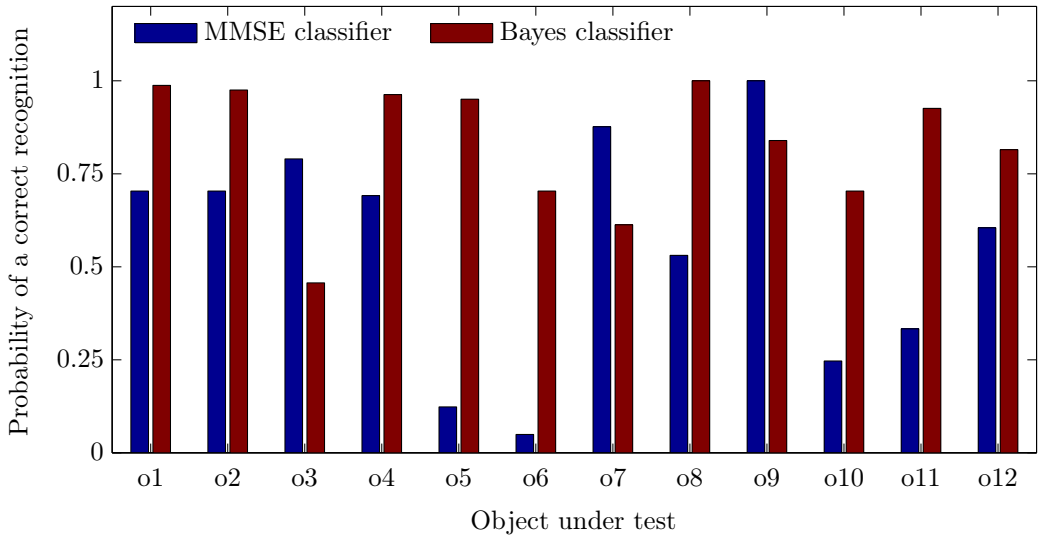

Figure 7.11: Results of the experimental OR validation with a Bayes classifier for 80 arbitrary 270° track measurements

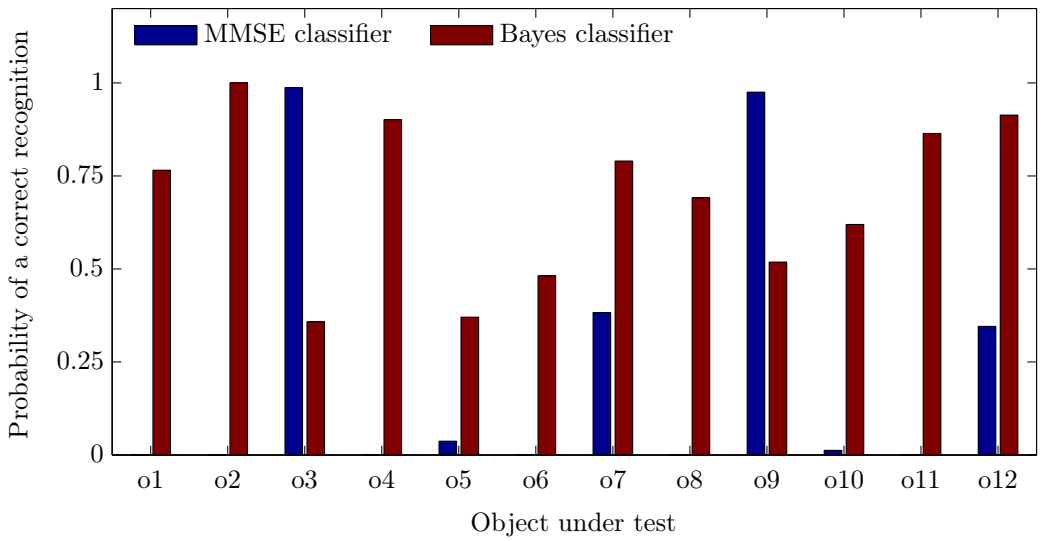

Figure 7.12: Results of the experimental OR validation with a Bayes classifier for 80 arbitrary 180° track measurements

EIGHTH CHAPTER

Conclusion

Due to the huge bandwidth of usually several GHz UWB signals obtain resolution in the cm and sub cm range. By locating the operational frequencies in the lower microwave region the super-resolution potential is established jointly with significant medium penetrating capabilities. With regard to these features, UWB offers novel technological applications and exhibits superior preferences compared with classical sensor technologies, e.g. infrared, optics, ultrasound and narrowband Radar.

As a consequence of the huge bandwidth, the envelope of the sounding UWB pulse is in the range of typical antenna and target dimensions. Thus, in contrast to narrowband systems, pulse distortion due to the involved geometries and transient effects of the hardware are non-negligible. Since these influences distort the pulse shape and yet the pulse shape determines directly the resolution capability, transient behaviour considerations are a prerequisite for any UWB Radar system. The evaluation of solely power related spectral quantities, which is the classical habitus in the narrowband case, are absolutely insufficient. In this respect, four time domain quality measures have been introduced which cover the pulse preserving quantification conveniently.

High-resolution methods resolve fine structures as long as two or more pulses do not or only slightly interfere. However, in the field of super-resolution the processing of even massively overlapped pulses is feasible. The most popular method to extract pulses is the matched filter based correlation method using a reference pulse. However, under more severely interfered conditions

this method deteriorates significantly. A crucial improvement could be conducted within this thesis. This progress is foremost due to the adaption of the Pauli scattering matrix decomposition to UWB Radar. Therewith, weak diffuse scattering contributions could be disjoint from strong dihedral reflections and are not masked anymore. Moreover, the correlation search is performed with a more appropriate synthetic reference pattern. This consists of a pair of reference pulses which exhibit a successively increasing delay. A final optimisation is applied which exploits the evolution of the signal history in the radargram. The resulting algorithm enables new levels of imaging and OR precision in the field of super-resolution UWB Radar and satisfies highest demands on accuracy.

For cases where the contour of the image is not well resolved due to resolution deficiencies or improper antenna alignment an algorithm for feature extraction is developed. Features are significant scattering or reflection centres which either provoke strong echoes or exhibit an almost omni reradiation pattern, i.e. edges, corners and alike geometries. The scattering centres of an object with a complex polygon contour (e.g. object o11 which partly provokes a massively distorted interference pattern of up to 3 diffuse scattering and 2 specular reflection contributions) can precisely be resolved by means of the proposed synthetic aperture focusing method.

An object recognition algorithm has been developed which evaluates both the previously determined object features and the migrated images obtained from the same measurements. Geometrical features, moment based features and texture based features are acquired and characterise each reference object as well as each measurement under test. An extraordinary accuracy can be achieved by the above mentioned pre-processing of the Radar data. Due to that, a simple minimum mean squared error classifier exhibits satisfying recognition rates for a full circular track around the objects. Additionally, a

Bayesian based classifier has been developed to entirely gather the radiation statistics of each reference object. By the exploitation of this probabilistic approach the recognition rates could significantly be increased over earlier publications. This benefit is most notably, when the full track is restricted and the object discrepancies suffer from minor relevance due to similar objects.

As a supplementary, a mathematically precise determination of a stereoscopic 3D image by means of a bi-static antenna configuration is developed. In this particular case, the wavefronts exhibit ellipsoidal shapes. Thus, for exact calculations the intersection point of 3 arbitrarily distributed ellipsoids in the three dimensional Euclidean space has to be determined. A mathematical approach for coordinate estimations with negligible deviations from the exact intersection point has been provided in this thesis.

All algorithms, methods and results in this thesis are experimentally validated. In particular, a vast measurement campaign has been carried out to prove the real-world capability of the object recognition as a whole system.

Future research should expand the investigations to dispersive dielectric material, for example, in the field of ground penetrating UWB Radar for landmine detection. There has always been a lack of focusing capability to satisfy the extremely high demands. Further, the adaption to new technological achievements e.g. sophisticated antenna arrays or increased bandwidths at higher centre frequencies should be performed.

Bibliography

[1] IEEE Std 1672-2006. IEEE Standard for Ultrawideband Radar Definitions. *E-ISBN: 0-7381-5317-6, DOI: 10.1109/IEEESTD.2007.359972*, pages c1–9, 2007.

[2] Y. Abe, S. Kidera, and T. Kirimoto. Accurate and Omnidirectional UWB Radar Imaging Algorithm With RPM Method Extended to Curvilinear Scanning Model. *IEEE Geoscience and Remote Sensing Letters*, 9(1):144–148, 2012.

[3] A. P. G. Ariza and R. S. Thomä. Polarimetric Ultrawideband MIMO Radar for Security Check Points: Detecting and Classifying Suspects carrying Wires. In *2012 6th European Conference on Antennas and Propagation (EUCAP)*, pages 1733–1736, March 2012.

[4] J. L. Awange and E. W. Grafarend. Algebraic Solution of GPS Pseudo-Ranging Equations. *GPS Solutions*, 5(4):20–32, 2002.

[5] C. A. Balanis. *Advanced Engineering Electromagnetics*. John Wiley & Sons, ISBN 0471503169, 1989.

[6] C. E. Baum, E. G. Farr, and C. A. Frost. Transient Gain of Antennas related to the Traditional Continuous-Wave (CW) Definition of Gain. In *Ultra-Wideband Short-Pulse Electromagnetics 4*, pages 109–118, 1998.

[7] J. W. Betz, R. W. Pinto, and J. L. Prince. A Model-Based Vision System for Object Recognition ith Synthetic Aperture Radar Data. In *1989 International Conference on Acoustics, Speech, and Signal Processing (ICASSP)*, pages 1618–1621 vol.3, 1989.

[8] H.-G. Beyer and K. Deb. On the Analysis of Self-Adaptive Evolutionary Algorithms. Technical report, Universität Dortmund, 1999.

[9] B. Bhanu and G. Jones. Target Recognition for Articulated and Occluded Objects in Synthetic Aperture Radar Imagery. In *1998 IEEE Radar Conference (RADARCON)*, pages 245–250, 1998.

[10] B. Bhanu and G. Jones. Object Recognition Results using MSTAR Synthetic Aperture Radar Data. In *IEEE Workshop on Computer Vision Beyond the Visible Spectrum: Methods and Applications*, pages 55–62, 2000.

[11] A. Björck. *Numerical Methods for Least Squares Problems.* SIAM, 1996.

[12] W. M. Boerner. Use of Polarization in Electromagnetic Inverse Scattering Radio Science. In *Special Issue: 1980 Munich Symposium on EM Waves*, pages 1037–1045, 1981.

[13] W. M. Boerner, M. El-Arini, Chung-Yee Chan, and P. Mastoris. Polarization Dependence in Electromagnetic Inverse Problems. *IEEE Transactions on Antennas and Propagation*, 29(2):262–271, 1981.

[14] W. M. Boerner and et al. *Inverse Methods in Electromagnetic Imaging, Proceedings of the NATO-Advanced Research Workshop (18-24 Sept. 1983, Bad Windsheim, FR Germany), NATO-ASI C-143, 1500 pages.* D. Reidel Publ. Co, 1985.

[15] W. M. Boerner and et al. *Direct and lnverse Methods in Radar Polarimetryt, NATO-ARW, Sept. 18-24, 1988, 1938 pages, NATO-ASI Series C: Math & Phys. Sciences, vol. C-350, Parts 1&2.* D. Reidel Publ. Co, 1992.

[16] W. M. Boerner, Wei ling Yan, A.-Q. Xi, and Y. Yamaguchi. On the Basic Principles of Radar Polarimetry: The Target Characteristic Polarization State Theory of Kennaugh, Huynen's Polarization Fork Concept and its Extension to the Partially Polarized Case. *Proceedings of the IEEE*, 79(10):1538–1550, 1991.

[17] R. Bose, A. Freedman, and B. D. Steinberg. Sequence CLEAN: A Modified Deconvolution Technique for Microwave Images of Contiguous Targets. *IEEE Transactions on Aerospace and Electronic Systems*, 38(1):89–97, 2002.

[18] J. Casey. *Exploring Curvature*. Springer Verlag, 1996.

[19] K. Chen. *A Simple Mathematical Approach for Determining Intersection of Quadratic Surfaces*. pp 271-298, in Multiscale Optimization Methods and Applications, Springer, 2006.

[20] S. R. Cloude and E. Pottier. A Review of Target Decomposition Theorems in Radar Polarimetry. *IEEE Transactions on Geoscience and Remote Sensing*, 34(2):498–518, 1996.

[21] J. R. Copeland. Radar Target Classification by Polarization Properties. *Proceedings of the IRE*, 48(7):1290–1296, 1960.

[22] R. J.-M. Cramer, R. A. Scholtz, and M. Z. Win. Evaluation of an Ultra-Wideband Propagation Channel. *IEEE Transactions on Antennas and Propagation*, 50(5):561–570, 2002.

[23] G. Crevecoeur, P. Sergeant, L. Dupre, and R. Van De Walle. A Two-Level Genetic Algorithm for Electromagnetic Optimization. *IEEE Transactions on Magnetics*, 46(7):2585–2595, 2010.

[24] D. Damjanov. Polarimetric UWB-Radar Super-Resolution Object Recognition. Master's thesis, University Duisburg-Essen, Fachgebiet Nachrichtentechnische Systeme (NTS), 2014.

[25] T. Deisler, J. Thielecke, R. Salman, T. Schultze, and I. Willms. UWB Radar Object Recognition for SLAM. In *2010 11th International Radar Symposium (IRS)*, pages 1–4, 2010.

[26] G. A. Deschamps. Techniques for Handling Elliptically Polarized Waves with Special Reference to Antennas: Part II - Geometrical Representation of the Polarization of a Plane Electromagnetic Wave. *Proceedings of the IRE*, 39(5):540–544, 1951.

[27] A. T. Dhar, B. D. Gray, and C. C. Menges. Characterizing Multi-Layered Vegetation with Dual-Polarimetric TerraSAR-X Imagery. In *2011 IEEE In-*

ternational Geoscience and Remote Sensing Symposium (IGARSS), pages 401–404, 2011.

[28] R. O. Duda, P. E. Hart, and D. G. Stork. *Pattern Classification*. John Wiley & Sons, 2012.

[29] D. Eberly. Intersection of Ellipses. Technical report, Geometric Tools, LLC, 2000.

[30] J. H. G. Ender, I. Walterscheid, and A. R. Brenner. New Aspects of Bistatic SAR: Processing and Experiments. In *2004 IEEE International Geoscience and Remote Sensing Symposium (IGARSS)*, volume 3, pages 1758–1762 vol.3, 2004.

[31] T. Espeter, I. Walterscheid, J. Klare, and J. H. G. Ender. Synchronization Techniques for the Bistatic Spaceborne/Airborne SAR Experiment with TerraSAR-X and PAMIR. In *2007 IEEE International Geoscience and Remote Sensing Symposium (IGARSS)*, pages 2160–2163, 2007.

[32] B. H. Fleury, M. Tschudin, R. Heddergott, D. Dahlhaus, and K. I. Pedersen. Channel Parameter Estimation in Mobile Radio Environments using the SAGE Algorithm. *IEEE Journal on Selected Areas in Communications*, 17(3):434–450, 1999.

[33] A. P. Garcia Ariza, R. Muller, F. Wollenschlager, A. Schulz, M. Elkhouly, Y. Sun, S. Glisic, U. Trautwein, R. Stephan, J. Muller, R. S. Thomä, and M. A. Hein. 60 GHz Ultrawideband Polarimetric MIMO Sensing for Wireless Multi-Gigabit and Radar. *IEEE Transactions on Antennas and Propagation*, 61(4):1631–1641, April 2013.

[34] E Geng and W. Wiesbeck. *Planungsmethoden für die Mobilkommunikation: Funknetzplanung unter realen physikalischen Ausbreitungsbedingungen*. Springer DE, ISBN 3642589804, 1998.

[35] F. Ghorbel. Stability of Invariant Fourier Descriptors and its Inference in the Shape Classification. In *11th IAPR International Conference on Pattern*

Recognition, Conference C: Image, Speech and Signal Analysis, Proceedings., pages 130–133, 1992.

[36] S. A. Greenhalgh, D. R. Pant, and C. R. A. Rao. Effect of Reflector Shape on Seismic Amplitude and Phase. *Wave Motion*, 16, no. 4(9):307–332, 1992.

[37] K. Haneda and J. I. Takada. An Application of SAGE Algorithm for UWB Propagation Channel Estimation. In *2003 IEEE Conference on Ultra Wideband Systems and Technologies*, pages 483–487, 2003.

[38] K. Haneda, J. I. Takada, and T. Kobayashi. Experimental Evaluation of a SAGE Algorithm for Ultra Wideband Channel Sounding in an Anechoic Chamber. In *Joint with 2004 Conference on Ultrawideband Systems and Technologies (UWBST) and 2004 International Workshop on Ultra Wideband Systems (IWUWBS)*, pages 66–70, 2004.

[39] S. Hantscher and C. G. Diskus. Resolution Improvement for UWB Wallscanning Radar Applications. In *2008 IEEE International Microwave Symposium Digest (MTT-S)*, pages 1163–1166, 2008.

[40] S. Hantscher and C. G. Diskus. Pulse-Based Radar Imaging Using a Genetic Optimization Approach for Echo Separation. *IEEE Sensors Journal*, 9(3):271–276, 2009.

[41] S. Hantscher, B. Etzlinger, A. Reisenzahn, and C. G. Diskus. A Wave Front Extraction Algorithm for High-Resolution Pulse Based Radar Systems. In *2007 IEEE International Conference on Ultra-Wideband (ICUWB)*, pages 590–595, 2007.

[42] S. Hantscher, B. Etzlinger, A. Reisenzahn, and C.G. Diskus. UWB Radar Calibration Using Wiener Filters for Spike Reduction. In *2006 International Microwave Symposium (MTT-S)*, pages 1995–1998, 2006.

[43] S. Hantscher, B. Praher, A. Reisenzahn, and C. G. Diskus. Analysis of Imaging Radar Algorithms for the Identifcation of Targets by Their Surface Shape. In *Antennen und Messverfahren für Ultra-Wide-Band (UWB)-Systeme, Kamp-Lintfort, Germany*, 12 2006.

[44] S. Hantscher, B. Praher, A. Reisenzahn, and C. G. Diskus. Comparison of UWB Target Identification Algorithms for Through-Wall Imaging Applications. In *2006 3rd European Radar Conference (EuRAD)*, pages 104–107, 2006.

[45] S. Hantscher, A. Reisenzahn, and C. G. Diskus. Through-Wall Imaging With a 3-D UWB SAR Algorithm. *Signal Processing Letters, IEEE*, 15:269–272, 2008.

[46] M. A. Hein. Ultra-Wideband Radar Sensors for Biomedical Diagnostics and Imaging. In *2012 IEEE International Conference on Ultra-Wideband (ICUWB)*, pages 486–490, 2012.

[47] M. A. Hein, M. Helbig, M. Kmec, J. Sachs, F. Scotto di Clemente, R. Stephan, M. Hamouda, T. Ussmueller, R. Weigel, M. Robens, R. Wunderlich, and S. Heinen. Ultra-Wideband Active Array Imaging for Biomedical Diagnostics. In *2012 IEEE-APS Topical Conference on Antennas and Propagation in Wireless Communications (APWC)*, pages 367–370, 2012.

[48] M. Helbig, M. A. Hein, U. Schwarz, and J. Sachs. Preliminary Investigations of Chest Surface Identification Algorithms for Breast Cancer Detection. In *2008 IEEE International Conference on Ultra-Wideband (ICUWB)*, volume 2, pages 195–198, 2008.

[49] M. Helbig, I. Hilger, M. Kmec, G. Rimkus, and J. Sachs. Experimental Phantom Trials for UWB Breast Cancer Detection. In *2012 7th German Microwave Conference (GeMiC)*, pages 1–4, 2012.

[50] R. Herrmann, J. Sachs, M. Kmec, M. Grimm, and P. Rauschenbach. Ultra-Wideband Sensor System for Remote Monitoring of Vitality at Home. In *2012 9th European Radar Conference (EuRAD)*, pages 234–237, 2012.

[51] J. A. Högbom. Aperture Synthesis with a Non-Regular Distribution of Interferometer Baselines. *Astronomy and Astrophysics Supplement*, 15:417–426, 1974.

[52] O. Hirsch, R. Zetik, and R. S. Thomä. *Chapter: Imaging in UWB Sensor Networks, Book: Wireless Sensor Networks: Application - Centric Design*. InTech, ISBN: 978-953-307-321-7, DOI: 10.5772/13397, 2010.

[53] Christoph M. Hoffmann. *Geometric and Solid Modeling: An Introduction*. Morgan Kaufmann Publishers Inc., San Francisco, CA, USA, 1989.

[54] G. Hoffmann. Pattern Recognition of Multiple Signals from Ground Penetrating Radar for Metal and Plastic Objects. *IEE Proceedings - Radar, Sonar and Navigation*, 151(2):91–99, 2004.

[55] http://www.ilmsens.com/. TU Ilmenau Service GmbH. Ehrenbergstraße 11, 98693 Ilmenau, Germany.

[56] Ming-Kuei Hu. Pattern Recognition by Moment Invariants. *Proceedings of the IRE Institute of Radio Engineers*, 49:1428, 1961.

[57] Ming-Kuei Hu. Visual Pattern Recognition by Moment Invariants. *Transactions on Information Theory (IRE)*, 8(2):179–187, 1962.

[58] R. T. Hussain, W. A. Sandham, and R. Chapman. Application of Migration to Ground Probing Radars. In *1988 International Conference on Acoustics, Speech, and Signal Processing (ICASSP)*, pages 1208–1211 vol.2, 1988.

[59] J. R. Huynen. *Phenomenological Theory of Radar Targets*. PhD thesis, TU Delft, the Netherlands, 1970.

[60] I. J. Immoreev and J.D. Taylor. Future of Radars. In *2002 IEEE Conference on Ultra Wideband Systems and Technologies*, pages 197–199, May 2002.

[61] M. Janson. *Hybride Funkkanalmodellierung für Ultrabreitbandige MIMO-Systeme*. PhD thesis, Karlsruher Institut für Technologie (KIT), Institut für Hochfrequenztechnik und Elektronik (IHE), 2011.

[62] M. Janson, R. Salman, T. Schultze, I. Willms, T. Zwick, and W. Wiesbeck. Hybrid Ray Tracing FDTD UWB-Model for Object Recognition. *Frequenz Journal of RF-Engineering and Telecommunications*, 63:pp. 217–220, Oct. 2009.

[63] B. Jähne. *Digital Image Processing*. Springer-Verlag, 2002.

[64] J. M. Johnson and V. Rahmat-Samii. Genetic Algorithms in Engineering Electromagnetics. *IEEE Antennas and Propagation Magazine*, 39(4):7–21, 1997.

[65] D. E. Joyce. The Laws of Cosines and Sines. Technical report, Department of Mathematics and Computer Science, Clark University, 1996.

[66] M. Kanda. Time Domain Sensors for Radiated Impulsive Measurements. *IEEE Transactions on Antennas and Propagation*, 31(3):438–444, 1983.

[67] E. M. Kennaugh. Polarization Properties of Radar Reflections. Master's thesis, Ohio State University, Columbus, 1952.

[68] E. M. Kennaugh. Effects of the Type of Polarization on Echo Characteristics. Technical report, Antenna Laboratory of the Ohio State University Research Foundation, 381-1 to 394-24, 1949 - 1954.

[69] M. I. Khalid, F. A. H. Khalid, and A. A. Abd-El-hadi. Two-Dimensional Imaging and Shape Recognition of Land buried Objects Through Polarimetric Ground Penetrating Radar. In *2012 Middle East Conference on Antennas and Propagation (MECAP)*, pages 1–5, 2012.

[70] S. Kidera, Y. Kani, T. Sakamoto, and T. Sato. An Experimental Study for a High-resolution 3-D Imaging Algorithm with Linear Array for UWB Radars. In *2007 IEEE International Conference on Ultra-Wideband (ICUWB)*, pages 600–605, 2007.

[71] S. Kidera and T. Kimmoto. Accurate 3-Dimensional Image Expansion Algorithm using Range Derivative of Double scattered Signals for UWB Radars. In *2011 XXXth URSI General Assembly and Scientific Symposium*, pages 1–4, 2011.

[72] S. Kidera and T. Kirimoto. Efficient Three-Dimensional Imaging Method Based on Enhanced Range Point Migration for UWB Radars. *IEEE Geoscience and Remote Sensing Letters*, 10(5):1104–1108, 2013.

[73] S. Kidera, T. Sakamoto, and T. Sato. A Robust and Fast Imaging Algorithm without Derivative Operations for UWB Pulse Radars. In *2006 1st European Conference on Antennas and Propagation (EuCAP)*, pages 1–6, 2006.

[74] S. Kidera, T. Sakamoto, and T. Sato. Accurate UWB Radar Three-Dimensional Imaging Algorithm for a Complex Boundary Without Range Point Connections. *IEEE Transactions on Geoscience and Remote Sensing*, 48(4):1993–2004, 2010.

[75] S. Kidera, T. Sakamoto, and T. Sato. Super-Resolution UWB Radar Imaging Algorithm Based on Extended Capon With Reference Signal Optimization. *IEEE Transactions on Antennas and Propagation*, 59(5):1606–1615, 2011.

[76] V. I. Koshelev. Detection and Recognition of Radar Objects at Sounding by High-Power Ultrawideband Pulses. In *2007 IEEE International Conference on Ultra-Wideband (ICUWB)*, pages 31–36, 2007.

[77] V. Kovalenko, A. G. Yarovoy, and L. P. Ligthart. A Novel Clutter Suppression Algorithm for Landmine Detection With GPR. *IEEE Transactions on Geoscience and Remote Sensing*, 45(11):3740–3751, 2007.

[78] P. K. Kumar and T. K. Kumar. Three Dimensional Imaging for Through-The-Wall Human Sensing. In *2011 International Conference on 3D Imaging (IC3D)*, pages 1–5, 2011.

[79] D.-H. Kwon. Effect of Antenna Gain and Group Delay Variations on Pulse-Preserving Capabilities of Ultrawideband Antennas. *IEEE Transactions on Antennas and Propagation*, 54(8):2208–2215, 2006.

[80] C. Le, T. Dogaru, Lam Nguyen, and M.A. Ressler. Ultrawideband (UWB) Radar Imaging of Building Interior: Measurements and Predictions. *IEEE Transactions on Geoscience and Remote Sensing*, 47(5):1409–1420, 2009.

[81] J. S. Lee and E. Pottier. *Polarimetric Radar Imaging from Basics to Applications*. CRC Press, 2009.

[82] B. Levitas. UWB Time Domain Measurements. In *2007 2nd European Conference on Antennas and Propagation (EuCAP)*, pages 1–8, 2007.

[83] Xuyang Li, G. Adamiuk, M. Janson, and T. Zwick. Polarization Diversity in Ultra-Wideband Imaging Systems. In *2010 IEEE International Conference on Ultra-Wideband (ICUWB)*, volume 1, pages 1–4, 2010.

[84] C. C. Lin and R. Chellappa. Classification of Partial 2-D Shapes using Fourier Descriptors. *IEEE Transactions on Pattern Analysis and Machine Intelligence*, PAMI-9(5):686–690, 1987.

[85] J. M. Lopez-Sanchez and J. Fortuny-Guasch. 3-D Radar Imaging using Range Migration Techniques. *IEEE Transactions on Antennas and Propagation*, 48(5):728–737, 2000.

[86] A. Ludloff. *Praxiswissen Radar und Radarsgnalverarbeitung.* Vieweg, 2002.

[87] S. P. Lukyanov and O. V. Stukach. Archeological Researches of the Ancient Fortress by GPR. In *2009 International Siberian Conference on Control and Communications (SIBCON)*, pages 324–331, 2009.

[88] E. Malz, R. S. Thomä, R. Zetik, P. Semashko, and A. P. G. Ariza. Polarimetric Ultrawideband Radar - Principles and Applications. In *2012 IEEE International Conference on Ultra-Wideband (ICUWB)*, pages 407–411, 2012.

[89] J. Maurer. *Strahlenoptisches Kanalmodell für die Fahrzeug-Fahrzeug-Funkkommunikation.* PhD thesis, Karlsruher Institut für Technologie (KIT), Institut für Hochfrequenztechnik und Elektronik (IHE), 2005.

[90] D. Miller, M. Oristaglio, and G. Beylkin. A New Slant on Seismic Imaging: Migration and Integral Geometry. *Geophysics*, 52:943–964, 1987.

[91] M. Mirbach and W. Menzel. A Simple Surface Estimation Algorithm for UWB Pulse Radars based on Trilateration. In *2011 IEEE International Conference on Ultra-Wideband (ICUWB)*, pages 273–277, 2011.

[92] M. Mirbach and W. Menzel. Time of Arrival based Localization of UWB Transmitters buried in Lossy Dielectric Media. In *2012 IEEE International Conference on Ultra-Wideband (ICUWB)*, pages 328–332, 2012.

[93] F. Mokhtarian. Silhouette-Based Isolated Object Recognition through Curvature.Scale Space. *IEEE Transactions on Pattern Analysis and Machine Intelligence*, 17:539–544, 1995.

[94] A. Nezirovic, A. G. Yarovoy, and L. P. Ligthart. Signal Processing for Improved Detection of Trapped Victims Using UWB Radar. *IEEE Transactions on Geoscience and Remote Sensing*, 48(4):2005–2014, 2010.

[95] J. Nocedal and S. Wright. *Numerical Optimization*. Springer, 2006.

[96] A. Norrdine. Scientific exchange and personal discussions on the mathematical calculation of the ellpsoid intersection calculation. Geodätisches Institut und Lehrstuhl für Bauinformatik & Geoinformationssysteme, RWTH Aachen University, 2013.

[97] A. Norrdine. Direkte Loesung des räumlichen Bogenschnitts mit Methoden der Linearen Algebra. *Allgemeine Vermessungs-Nachrichten (AVN)*, 1:7–9, 2008.

[98] J. S. Orfanidis. *Electromagnetic Waves and Antennas*. http://www.ece.rutgers.edu/ orfanidi/ewa/, 2008.

[99] E. Pancera. *Strategies for Time Domain Characterization of UWB Components and Systems*. PhD thesis, Karlsruher Institut für Technologie (KIT), Institut für Hochfrequenztechnik und Elektronik (IHE), 2009.

[100] E. Pancera, A. Bhattacharya, E. Veshi, T. Zwick, and W. Wiesbeck. Ultra Wideband Impulse Radar Calibration. In *2009 IET International Radar Conference*, pages 1–4, 2009.

[101] E. Pancera, T. Zwick, and W. Wiesbeck. Full Polarimetric Time Domain Calibration for UWB Radar Systems. In *2009 European Radar Conference (EuRAD)*, pages 105–108, 2009.

[102] A. Papoulis. *Signal analysis*. McGraw-Hill, ISBN 0070484600, 1977.

[103] R. Parks. Seismic Data Acquisition and Processing Equipment for Edinburgh Royal Observatory. *Radio and Electronic Engineer*, 31(3):171–180, 1966.

[104] A. J. Patterson, J. M. Tealby, and N. M. Allinson. Ground Penetrating Radar Migration with Uncertain Parameters. In *1995 International Geoscience and Remote Sensing Symposium (IGARSS)*, volume 1, pages 27–29 vol.1, 1995.

[105] J. G. Proakis. *Digital Communications*. McGraw-Hill Higher Education, ISBN 9780072321111, 2001.

[106] J. G. Proakis. *Digital Signal Processing: Principles, Algorithms, And Applications*. Pearson Education, ISBN 8131710009, 2007.

[107] G. Quintero, J.-F. Zurcher, and A.K. Skriverviky. System Fidelity Factor: A New Method for Comparing UWB Antennas. *IEEE Transactions on Antennas and Propagation*, 59(7):2502–2512, 2011.

[108] S. S. Qureshi, Xueming Li, and T. Ahmad. Applying Super Resolution Techniques for Objects Recognition in Radar. In *2011 4th IEEE International Conference on Broadband Network and Multimedia Technology (IC-BNMT)*, pages 483–487, 2011.

[109] L. Reichardt, S. Beer, T. Deissler, R. Salman, R. Zetik, and T. Zwick. A Dual-Polarized UWB Antenna System for the Demonstration of Autonomous Localization and Object Recognition with Mobile Sensors. In *2013 International Workshop on Antenna Technology (iWAT)*, pages 137–140, 2013.

[110] T. H. Reiss. *Recognizing Planar Objects Using Invariant Image Features*. Springer, Berlin, 1993.

[111] S. Riegger and W. Wiesbeck. Wide-Band Polarimetry and Complex Radar Cross Section Signatures. *Proceedings of the IEEE*, 77(5):649–658, 1989.

[112] J. Sachs. *Handbook of Ultra-Wideband Short-Range Sensing. Theory, Sensors, Applications*. Weinheim: Wiley-VCH, 2012.

[113] J. Sachs, A. Badstubner, F. Bonitz, M. Eidner, M. Helbig, R. Herrmann, M. Kmec, P. Rauschenbach, and H. Solas. High Resolution Non-Destructive Testing in Civil Engineering by Ultra-Wideband Pseudo-Noise Approaches. In *2008 IEEE International Conference on Ultra-Wideband (ICUWB)*, volume 2, pages 137–140, 2008.

[114] J. Sachs, R. Herrmann, M. Kmec, M. Helbig, and K. Schilling. Recent Advances and Applications of M-Sequence based Ultra-Wideband Sensors. In *2007 IEEE International Conference on Ultra-Wideband (ICUWB)*, pages 50–55, 2007.

[115] T. Sakamoto and T. Sato. A Target Shape Estimation Algorithm for Pulse Radar Systems Based on Boundary Scattering Transform. *IEICE Transactions on Communications*, E87:1357–1365, 2004.

[116] T. Sakamoto and T. Sato. A Novel Transform for Ultra-Wideband Multi-Static Imaging Radar. In *2012 6th European Conference on Antennas and Propagation (EUCAP)*, pages 1724–1728, 2012.

[117] T. Sakamoto, T. Sato, R. Salman, I. Willms, and A. G. Yarovoy. Novel Transform for Ultra Wide-Band Radar Imaging with Circular Scanning Antennas . In *2013 10th European Radar Conference (EuRAD)*, 2013.

[118] T. Sakamoto, T. Sato, R. Salman, I. Willms, and A. G. Yarovoy. Quasi-Wavefront Selection Algorithm for Fast and Accurate Ultra-Wideband Imaging with Polar Revised Range Point Migration . In *2013 IEEE International Conference on Ultra-Wideband (ICUWB)*, 2013.

[119] T. Sakamoto, T. Savelyev, P. Aubry, and A. Yarovoy. Fast Range Point Migration Method for Weapon Detection using Ultra-Wideband Radar. In *2012 9th European Radar Conference (EuRAD)*, pages 230–233, 2012.

[120] R. Salman, T. Schultze, M. Janson, W. Wiesbeck, and I. Willms. Robust UWB Radar Object Recognition. In *2008 IEEE International RF and Microwave Conference (RFM)*, pages 399–403, 2008.

[121] R. Salman, T. Schultze, and I. Willms. UWB Material Characterisation and Object Recognition with Applications in Fire and Security. In *2008 IEEE International Conference on Ultra-Wideband (ICUWB)*, volume 2, pages 203–206, 2008.

[122] R. Salman, T. Schultze, and I. Willms. Rough UWB Object Imaging for Improved Microwave Fire Detection. In *2009 14th International Conference on Automatic Fire Detection (AUBE)*, 2009.

[123] R. Salman, T. Schultze, and I. Willms. Performance Enhancement of UWB Material Characterization and Object Recognition for Security Robots. *Journal of Electrical and Computer Engineering*, vol. 2010:6 pages, 2010.

[124] R. Salman, T. Schultze, and I. Willms. UWB Object Recognition based on Ray-tracing Reference Data. Technical report, Berichtskolloquium zum DFG Schwerpunktprogramm Ultrabreitband Funktechniken für Kommunikation, Lokalisierung und Sensorik (UKoLoS), Senatssaal in Kollegienhaus (KH 1.011), Erlangen, Feb. 2009.

[125] R. Salman, T. Schultze, and I. Willms. 3D UWB Radar Super-Resolution Imaging for Complex Objects with Fragmented Wavefronts. Technical report, Berichtskolloquium zum DFG Schwerpunktprogramm Ultrabreitband Funktechniken für Kommunikation, Lokalisierung und Sensorik (UKoLoS), Karlsruher Institut für Technologie, Karlsruhe, Feb. 2011.

[126] R. Salman, T. Schultze, and I. Willms. Onsets and System Design for a Mobile Security Robot equipped with UWB-Radar Technology. Technical report, Berichtskolloquium zum DFG Schwerpunktprogramm Ultrabreitband Funktechniken für Kommunikation, Lokalisierung und Sensorik (UKoLoS), Christian-Albrechts-Universität Kiel, Kiel, Germany, July 2012.

[127] R. Salman, T. Schultze, and I. Willms. UWB Object Recognition for Building Construction Inspection and for Applications in Micro-wave Fire Detection. Technical report, Berichtskolloquium zum DFG Schwerpunktprogramm Ultrabreitband Funktechniken für Kommunikation, Lokalisierung und Sensorik (UKoLoS), Schloss Günzburg / Donau, Mar. 2010.

[128] R. Salman, T. Schultze, and I. Willms. Ultrabreitband (UWB) Mikrowellen-Radar für Sicherheitsanwendungen (in german). Technical report, Verein zur Förderung des Deutschen Brandschutzes e.V., Otto-von-Guericke-Universität, Magdeburg, Okt. 2010.

[129] R. Salman and I. Willms. A Novel UWB Radar Super-Resolution Object Recognition Approach for Complex Edged Objects. In *2010 IEEE International Conference on Ultra-Wideband (ICUWB)*, volume 2, pages 1–4, 2010.

[130] R. Salman and I. Willms. In-Wall Object Recognition based on SAR-like Imaging by UWB-Radar. In *2010 8th European Conference on Synthetic Aperture Radar (EUSAR)*, pages 1–4, 2010.

[131] R. Salman and I. Willms. *Super-Resolution Object Recognition Approach for Complex Edged Objects by UWB Radar*. InTech, ISBN: 978-953-307-222-7, DOI: 10.5772/15574, 2011.

[132] R. Salman and I. Willms. 3D UWB Radar Super-Resolution Imaging for Complex Objects with Discontinous Wavefronts. In *2011 IEEE International Conference on Ultra-Wideband (ICUWB)*, pages 346–350, 2011, Best Student Paper Award.

[133] R. Salman and I. Willms. A Mobile Security Robot Equipped with UWB-Radar for Super-Resolution Indoor Positioning and Localisation Applications. In *2012 International Conference on Indoor Positioning and Indoor Navigation (IPIN)*, pages 1–8, 2012.

[134] R. Salman and I. Willms. Exploitation of Polarimetry in Short Range 3D UWB-Radar Object Imaging. In *2012 International Conference on 3D Imaging (IC3D)*, pages 1–7, 2012.

[135] R. Salman and I. Willms. Joint Efficiency and Performance Enhancement of Wavefront Extraction Algorithms for Short-Range Super-Resolution UWB Radar. In *2012 The 7th German Microwave Conference (GeMiC)*, pages 1–4, 2012.

[136] R. Salman and I. Willms. Recent Advances in Short-Range Super-Resolution UWB-Radar Technology . In *2013 Radar, Communication and Measurement (RADCOM)*, volume 2, pages 661–666, 2013.

[137] R. Salman and I. Willms. Scattering Matrix Decomposition of Quad-Polarized Short-Range Ultrawideband Radar Data. In *2013 14th International Radar Symposium (IRS)*, volume 2, pages 661–666, 2013.

[138] R. Salman and I. Willms. Hochauflösende Objektlokalisierung mittels UWB-Radar. Technical report, ITG-Fachausschuss 7.2: Funksysteme, Funklokalisierung - sicher, schnell und genau, Nov. 2010.

[139] R. Salman, I. Willms, L. Reichardt, T. Zwick, and W. Wiesbeck. On Polarization Diversity Gain in Short Range UWB-Radar Object Imaging. In *2012 IEEE International Conference on Ultra-Wideband (ICUWB)*, pages 402–406, 2012.

[140] R. Salman, I. Willms, L. Reichardt, T. Zwick, and W. Wiesbeck. Geometry Classification by Means of Scattering Matrix Decomposition for Ultra-Wideband Radar . In *2013 10th European Radar Conference (EuRAD)*, 2013.

[141] R. Salman, I. Willms, L. Reichardt, T. Zwick, W. Wiesbeck, and R. S. Thomä. On Buried Weapon Detection by Means of Scattering Matrix Decomposition for Quad-Polarized Ultra-Wideband Radar . In *2013 IEEE International Conference on Ultra-Wideband (ICUWB)*, 2013.

[142] R. Salman, I. Willms, T. Sakamoto, T. Sato, and A. G. Yarovoy. 3D Imaging of a Manmade Target with Weak Scattering Centres by Means of UWB. In *2013 IEEE International Conference on Ultra-Wideband (ICUWB)*, 2013.

[143] R. Salman, I. Willms, T. Sakamoto, T. Sato, and A. G. Yarovoy. Environmental Imaging with a Mobile UWB Security Robot for Indoor Localisation and Positioning Applications. In *2013 10th European Radar Conference (EuRAD)*, 2013.

[144] T. Santos, J. Karedal, P. Almers, F. Tufvesson, and A. F. Molisch. Scatterer Detection by Successive Cancellation for UWB - Method and Experimental

Verification. In *2008 IEEE Vehicular Technology Conference (VTC)*, pages 445–449, 2008.

[145] T. G. Savelyev, L. Van Kempen, H. Sahli, J. Sachs, and M. Sato. Investigation of Time-Frequency Features for GPR Landmine Discrimination. *IEEE Transactions on Geoscience and Remote Sensing*, 45(1):118–129, 2007.

[146] T. G. Savelyev and A. G. Yarovoy. Fast Imaging by 3-D Deconvolution in Short-Range UWB Radar for Concealed Weapon Detection. In *2012 9th European Radar Conference (EuRAD)*, pages 26–29, 2012.

[147] A. Schiessl, A. Genghammer, S. S. Ahmed, and L. Schmidt. Phase Error Sensitivity in Multistatic Microwave Imaging Systems. In *2013 European Microwave Conference (EuMC)*, pages 1631–1634, 2013.

[148] O. Schimmer, F. Daschner, and R. Knöchel. UWB-Sensors in Food Quality Management - The Way from the Concept to Market. In *2008 IEEE International Conference on Ultra-Wideband (ICUWB)*, volume 2, pages 141–144, 2008.

[149] W. A. Schneider. Developments in Seismic Data Processing and Analysis: 1968 - 1970. *Geophysics*, 36, no. 6:1043 – 1073, 1971.

[150] W. A. Schneider. Integral Formulation for Migration in Two and Three Dimensions. *Geophysics*, 43:49–76, 1978.

[151] T. Schultze, R. Salman, and I. Willms. Microwave Ellipsometry and its Application in Emergency Scenarios . In *2009 14th International Conference on Automatic Fire Detection (AUBE)*, 2009.

[152] T. Schultze, R. Salman, and I. Willms. UWB Material Inspection and Object Recognition for Security Applications. Technical report, Berichtskolloquium zum DFG Schwerpunktprogramm Ultrabreitband Funktechniken für Kommunikation, Lokalisierung und Sensorik (UKoLoS), Hotel Gabelbach, Ilmenau, May. 2008.

[153] G. Shen, R. Zetik, H. Yan, O. Hirsch, and R. S. Thomä. Time of Arrival Estimation for Range-Based Localization in UWB Sensor Networks. In *2010 IEEE International Conference on Ultra-Wideband (ICUWB)*, volume 2, pages 1–4, 2010.

[154] G. Shen, R. Zetik, H. Yan, S. Jovanoska, and R. S. Thomä. Localization of Active UWB Sensor Nodes in Multipath and NLOS Environments. In *Antennas and Propagation (EUCAP), Proceedings of the 5th European Conference on*, pages 126–130, 2011.

[155] D. Silverman. Mapping the Earth with Elastic Wave Holography. *IEEE Transactions on Geoscience Electronics*, 7(4):190–199, 1969.

[156] G. W. Sinclair. Modification of the Radar Target Equation for Arbitrary Targets and Arbitrary Polarization. Technical report, Antenna Laboratory of the Ohio State University Research Foundation, 302-19,1948.

[157] P. Singer, D. Ströbel, R. Hördt, J. Bahndorf, and K. Linkwitz. Direkte Lösung des räumlichen Bogenschnitts. *Zeitschrift für Vermessungswesen (ZfV)*, 1:21–24, 1993.

[158] M. I. Skolnik. *Radar Handbook*. McGraw-Hill, ISBN 9780070579132, 1990.

[159] T. Spreng, U. Prechtel, B. Schonlinner, V. Ziegler, A. Meusling, and U. Siart. UWB Near-Field MIMO Radar: Calibration, Measurements and Image Reconstruction. In *2013 European Radar Conference (EuRAD)*, pages 33–36, 2013.

[160] W. Sörgel. *Charakterisierung von Antennen für die Ultra-Wideband-Technik*. PhD thesis, Karlsruher Institut für Technologie (KIT), Institut für Hochfrequenztechnik und Elektronik (IHE), 2007.

[161] W. Sörgel and W. Wiesbeck. Influence of the Antennas on the Ultra-Wideband Transmission. *EURASIP Journal on Advances in Signal Processing*, 2005(3):843268, 2005.

[162] R. H. Stolt. Migration by Fourier Transform. *Geophysics*, 43:23–48, 1978.

[163] R. S. Thomä, R. Knöchel, J. Sachs, I. Willms, and T. Zwick, editors. *Ultra-Wideband Radio Technologies for Communications, Localization and Sensor Applications*. InTech, ISBN 978-953-51-0936-5, DOI: 10.5772/2648, 2013.

[164] L. A. Torres-Mendez, J. C. Ruiz-Suarez, L. E. Sucar, and G. Gomez. Translation, rotation, and scale-invariant object recognition. *IEEE Transactions on Systems, Man and Cybernetics, Part C: Applications and Reviews*, 30(1):125–130, Feb 2000.

[165] J. Tsao and B. D. Steinberg. Reduction of Sidelobe and Speckle Artifacts in Microwave Imaging: The CLEAN Technique. *IEEE Transactions on Antennas and Propagation*, 36(4):543–556, 1988.

[166] F. T. Ulaby, R. K. Moore, and A. K. Fung. *Microwave Remote Sensing: From theory to applications*. Addison-Wesley Publishing Company, Advanced Book Program/World Science Division, ISBN 0890061920, 1981.

[167] W. Wiesbeck. The Radar of the Future. In *2013 10th European Radar Conference (EuRAD)*, 2013.

[168] W. Wiesbeck, G. Adamiuk, and C. Sturm. Basic Properties and Design Principles of UWB Antennas. *Proceedings of the IEEE*, 97(2):372–385, 2009.

[169] W. Wiesbeck, C. Sturm, W. Soergel, M. Porebska, and G. Adamiuk. Influence of Antenna Performance and Propagation Channel on Pulsed UWB Signals. In *2007 International Conference on Electromagnetics in Advanced Applications (ICEAA)*, pages 915–922, 2007.

[170] I. Willms, T. Schultze, R. Salman, W. Krüll, N. Von Wahl, and S. Heinen. Microwave Fire Detection. *Journal of European Society for Automatic Alarm Systems (EUSAS)*, vol. 2009, 2009.

[171] H. Yan, G. Shen, O. Hirsch, R. Zetik, and R. S. Thomä. A UWB Active Sensor Localization Method based on Time-Difference Back-Projection. In *2010 IEEE International Conference on Ultra-Wideband (ICUWB)*, volume 1, pages 1–4, 2010.

[172] R. Zetik, J. Sachs, and R. S. Thomä. Modified Cross-Correlation Back Projection for UWB Imaging: Numerical Examples. In *2005 IEEE International Conference on Ultra-Wideband (ICUWB)*, 2005.

[173] R. Zetik and R. S. Thomä. Monostatic Imaging of Small Objects in UWB Sensor Networks. In *2008 IEEE International Conference on Ultra-Wideband (ICUWB)*, volume 2, pages 191–194, 2008.

[174] X. Zhuge, T. G. Savelyev, A. G. Yarovoy, L. P. Ligthart, and B. Levitas. Comparison of Different Migration Techniques for UWB Short-Range Imaging. In *2009 European Radar Conference (EuRAD)*, pages 184–187, 2009.

[175] X. Zhuge, A. G. Yarovoy, T. G. Savelyev, and L. P. Ligthart. Modified Kirchhoff Migration for UWB MIMO Array-Based Radar Imaging. *IEEE Transactions on Geoscience and Remote Sensing*, 48(6):2692–2703, 2010.

Publications of the Author

1. **R. Salman**, I. Willms, L. Reichardt, T. Zwick and W. Wiesbeck, "Geometry Classification by Means of Scattering Matrix Decomposition for Ultra-Wideband Radar", *IEEE 10th European Radar Conference (EuRAD)*, Nuremberg, Germany, Oct. 2013.

2. **R. Salman**, I. Willms, T. Sakamoto, T. Sato, A. Yarovoy, "Environmental Imaging with a Mobile UWB Security Robot for Indoor Localisation and Positioning Applications", *IEEE 10th European Radar Conference (EuRAD)*, Nuremberg, Germany, Oct. 2013.
   Nominated for the EuRAD Best Paper Award.

3. T. Sakamoto, T. Sato, **R. Salman**, I. Willms and A. Yarovoy, "Novel Transform for Ultra Wide-Band Radar Imaging with Circular Scanning Antennas", *IEEE 10th European Radar Conference (EuRAD)*, Nuremberg, Germany, Oct. 2013.

4. **R. Salman**, I. Willms, L. Reichardt, T. Zwick, W. Wiesbeck and R. S. Thomä, "On Buried Weapon Detection by Means of Scattering Matrix Decomposition for Quad-Polarized Ultra-Wideband Radar", *IEEE International Conference on Ultra-Wideband (ICUWB)*, Sydney, Australia, Sep. 2013.

5. **R. Salman**, I. Willms, T. Sakamoto, T. Sato and A. Yarovoy, "3D Imaging of a Manmade Target with Weak Scattering Centres by Means of UWB", *IEEE International Conference on Ultra-Wideband (ICUWB)*, Sydney, Australia, Sep. 2013.

6. T. Sakamoto, T. Sato, **R. Salman**, I. Willms and A. Yarovoy, "Quasi-Wavefront Selection Algorithm for Fast and Accurate Ultra-Wideband Imaging with Polar Revised Range Point Migration", *IEEE International Conference on Ultra-Wideband (ICUWB)*, Sydney, Australia, Sep. 2013.

7. **R. Salman** and I. Willms, "Scattering Matrix Decomposition of Quad-Polarized Short-Range Ultrawideband Radar Data", *IEEE 13th International Radar Symposium (IRS)*, Dresden, Germany, June 2013.

8. **R. Salman** and I. Willms, "Recent Advances in Short-Range Super-Resolution UWB-Radar Technology", *Radar, Communication and Measurement (RADCOM)*, Hamburg, Germany, April 2013.

9. L. Reichardt, S. Beer, T. Deißler, **R. Salman**, R. Zetik and T. Zwick, "A Dual-polarized UWB Antenna System for the Demonstration of Autonomous Localization and Object Recognition with Mobile Sensors", *IEEE International Workshop on Antenna Technology (iWAT)*, Karlsruhe, Germany, March 2013.

10. **R. Salman** and I. Willms, "Exploitation of Polarimetry in Short Range 3D UWB-Radar Object Imaging", *IEEE International Conference on 3D Imaging (IC3D)*, Liège, Belgium, Dec. 2012.

11. **R. Salman** and I. Willms, "A Mobile Security Robot equipped with UWB-Radar for Super-Resolution Indoor Positioning and Localisation Applications", *IEEE International Conference on Indoor Positioning and Indoor Navigation (IPIN)*, Sydney, Australia, Nov. 2012.

12. **R. Salman**, I. Willms, L. Reichardt, T. Zwick and W. Wiesbeck, "On Polarization Diversity Gain in Short Range UWB-Radar Object Imaging", *IEEE International Conference on Ultra-Wideband (ICUWB)*, Syracuse, USA, Sept. 2012.

13. R. Zetik, H. Yan, E. Malz, S. Jovanoska, G. Shen, R. S. Thomä, **R. Salman**, T. Schultze, R. Tobera, I. Willms, L. Reichardt, M. Janson, T. Zwick, W.Wiesbeck, T. Deißler and J. Thielecke , *Cooperative Localization and Object Recognition*, R.S. Thomä, R. Knöchel, J. Sachs, I. Willms, T. Zwick (Eds.), UKoLoS Ultra-Wideband Radio Technologies for Communications, Localization and Sensor Applications, InTech Academic Publisher, DOI 10.5772/2648, ISBN 978-953-51-0936-5, March 2013.

14. **R. Salman**, Th. Schultze and I. Willms, "Onsets and System Design for a Mobile Security Robot equipped with UWB-Radar Technology", *Berichtskolloquium zum DFG Schwerpunktprogramm Ultrabreitband-Funktechniken für*

Kommunikation, Lokalisierung und Sensorik (UKoLoS), Christian-Albrechts-Universität, Kiel, Germany, July 2012.

15. **R. Salman** and I. Willms, "Joint Efficiency and Performance Enhancement of Wavefront Extraction Algorithms for Short-Range Super-Resolution UWB Radar", *IEEE German Microwave Conference (GeMiC)*, Ilmenau, Germany, March 2012.

16. **R. Salman** and I. Willms, "3D UWB Radar Super-Resolution Imaging for complex Objects with discontinous Wavefronts", *IEEE International Conference on Ultra-Wideband (ICUWB)*, Bologna, Italy, Sept. 2011.
Best Student Paper Award.

17. **R. Salman**, Th. Schultze and I. Willms, "3D UWB-Radar Super-Resolution Imaging for complex Objects with fragmented Wavefronts", *Berichtskolloquium zum DFG Schwerpunktprogramm Ultrabreitband-Funktechniken für Kommunikation, Lokalisierung und Sensorik" (UKoLoS)*, Karlsruher Institut für Technologie, Karlsruhe, Germany, Feb. 2011.

18. **R. Salman** and I. Willms, *Super-Resolution Object Recognition Approach for Complex Edged Objects by UWB Radar*, T. P. Cao (Ed.), Object Recognition, DOI 10.5772/15574, ISBN 978-953-307-222-7, Feb. 2011.

19. **R. Salman** and I. Willms, "Hochauflösende Objektlokalisierung mittels UWB-Radar", *ITG-Fachausschuss 7.2: Funksysteme, Funklokalisierung - sicher, schnell und genau*, Technische Universität Ilmenau, Ilmenau, Germany, Nov. 2010.

20. **R. Salman**, Th. Schultze and I. Willms, "Ultrabreitband (UWB) Mikrowellen-Radar für Sicherheitsanwendungen", *VFDB Workshop Brandschutzforschung in Magdeburg*, Otto-von-Guericke-Universität, Magdeburg, Germany, Oct. 2010.

21. **R. Salman** and I. Willms, "A novel UWB Radar super-resolution object recognition approach for complex edged objects", *IEEE International Conference on Ultra-Wideband (ICUWB)*, Nanjing, China, Sept. 2010.

22. T. Deisler, J. Thielecke, **R. Salman**, Th. Schultze and I. Willms , "UWB Radar Object Recognition for SLAM ", *IEEE 11th International Radar Symposium (IRS)*, Vilnius, Lithuania, June 2010.

23. **R. Salman** and I. Willms, "In-Wall Object Recognition based on SAR-like Imaging by UWB-Radar ", *8th European Conference on Synthetic Aperture Radar*, Eurogress, Aachen, Germany, June 2010.

24. Th. Schultze, **R. Salman** and I. Willms, "UWB Object Recognition for Building Construction Inspection and for Applications in Microwave Fire Detection", *Berichtskolloquium zum DFG Schwerpunktprogramm Ultrabreitband-Funktechniken für Kommunikation, Lokalisierung und Sensorik (UKoLoS)*, Günzburg, Germany, March 2010.

25. **R. Salman**, Th. Schultze and I. Willms, "Performance Enhancement of UWB Material Characterization and Object Recognition for Security Robots ", *Journal of Electrical and Computer Engineering*, vol. 2010, Article ID 314695, 6 pages, DOI 10.1155/2010/314695, Received 28 April 2009, Accepted 13 Sep. 2009.

26. M. Janson, **R. Salman**, Th. Schultze, I. Willms, T. Zwick and W. Wiesbeck, "Hybrid Ray Tracing FDTD UWB-model for Object Recognition", *Frequenz Journal of RF-Engineering and Telecommunications*, vol. 63, pp. 217-220, Oct. 2009.

27. Th. Schultze, **R. Salman** and I. Willms, "Microwave Ellipsometry and its Application in Emergency Scenarios", *14th International Conference on Automatic Fire Dtetection (AUBE)*, Duisburg, Germany, Sep. 2009.

28. **R. Salman**, Th. Schultze, M. Mladenov and I. Willms, "Rough UWB Object Imaging for Improved Microwave Fire Detection", *14th International Conference on Automatic Fire Dtetection (AUBE)*, Duisburg, Germany, Sep. 2009.

29. I. Willms, Th. Schultze, **R. Salman**, W. Krüll, N. von Wahl and S. Heinen , "Microwave Fire Detection", *EUSAS Journal*, No. 5, April 2009.

30. **R. Salman**, Th. Schultze and I. Willms, "UWB Object Recognition based on Ray-tracing Reference Data", *Berichtskolloquium zum DFG Schwerpunktprogramm Ultrabreitband-Funktechniken für Kommunikation, Lokalisierung und Sensorik (UKoLoS)*, Erlangen, Feb. 2009.

31. **R. Salman**, Th. Schultze and I. Willms, "Robust UWB Radar Object Recognition ", *IEEE International Radio Frequency and Microwave Conference (RFM)*, Kuala Lumpur, Malaysia, Dec. 2008.

32. **R. Salman**, Th. Schultze and I. Willms, "UWB Material Characterisation and Object Recognition with Applications in Fire and Security", *IEEE International Conference on Ultra-Wideband (ICUWB)* Hannover, Germany, Sep. 2008.

33. Th. Schultze, **R. Salman** and I. Willms, "UWB Material Inspection and Object Recognition for Security Applications", *Berichtskolloquium zum DFG Schwerpunktprogramm Ultrabreitband-Funktechniken für Kommunikation, Lokalisierung und Sensorik (UKoLoS)*, Ilmenau, Germany, 2008.